



Cite this: *Energy Adv.*, 2025, 4, 820

## A comprehensive review of lithium-ion battery components degradation and operational considerations: a safety perspective

Idris T. Adebanjo, <sup>†</sup><sup>a</sup> Juliana Eko, <sup>†</sup><sup>a</sup> Anita G. Agbeyegbe, <sup>a</sup> Simuck F. Yuk, <sup>bc</sup> Samuel V. Cowart, <sup>\*bc</sup> Enoch A. Nagelli, <sup>bc</sup> F. John Burpo, <sup>bc</sup> Jan L. Allen, <sup>\*d</sup> Dat T. Tran, <sup>d</sup> Nishma Bhattarai, <sup>e</sup> Krishna Shah, <sup>e</sup> Jang-Yeon Hwang <sup>fg</sup> and H. Hohyun Sun <sup>\*a</sup>

As the demand for sustainable energy storage solutions grows, lithium-ion batteries (LIBs) remain at the forefront of modern energy technologies, widely adopted in electric vehicles and energy storage systems. Although they offer high energy densities and reliability, their long-term usage and safety are compromised by complex structural degradation mechanisms and thermal instability, which affect their key components—cathode, anode, and electrolyte—culminating in hazardous events. To comprehensively address these challenges, this review article elaborates on the electrochemical and physicochemical properties of these key components, exploring their structural characteristics, performance in practical applications, and limitations. A thorough understanding of the degradation pathways of the key components along with various strategies to mitigate failure and enhance safety are highlighted. Finally, attention is given to the unique challenges associated with first responder applications with a specific focus on military operations in extreme environments, such as high and subzero temperatures, mechanical shocks, vibrations, and prolonged storage. This review highlights the critical need for advancements in battery design to ensure safety, durability, and long-term usability in demanding environments.

Received 7th March 2025,  
Accepted 23rd April 2025

DOI: 10.1039/d5ya00065c

rsc.li/energy-advances

## Introduction

In the pursuit of global decarbonization and electric transport, interest in advanced, zero-emission energy systems has intensified. Lithium-ion batteries (LIBs) have enjoyed much success owing to their excellent energy densities and reliability, which have been extensively field-tested. Despite the growing

application cases for these batteries, their structural degradation and inherent thermal instability still pose significant safety challenges. With usage and time, the cell's internal resistance increases, and the storage capacity of their cells diminishes due to degradation mechanisms that either co-occur or trigger further mechanisms.<sup>1</sup> Moreover, the safety hazards of LIBs are products of unwanted electrode/electrolyte side reactions that stem from structural degradations occurring in the battery during standard operations, culminating in thermal runaways.<sup>2</sup> Thermal runaway events result from a chain of vigorous exothermic reactions that are often difficult to predict and prevent in real-time.<sup>2,3</sup> Therefore, understanding the degradation of key components—cathode, anode, and electrolyte—is imperative because of the interplay between factors that trigger or exacerbate the degradation mechanisms of each battery component.

Safety concerns surrounding LIBs have become increasingly evident, particularly in high-risk environments such as aviation, electric vehicles (EVs), and large-scale energy storage systems (ESS). Kapp *et al.*<sup>4</sup> analyzed 274 thermal runaway incidents in U.S. commercial aviation from 1996 to 2019, noting a sharp rise in cases since 2015, with most incidents

<sup>a</sup> Department of Chemical and Biological Engineering, The University of Alabama, Tuscaloosa, AL 35487, USA. E-mail: hsun36@ua.edu

<sup>b</sup> Department of Chemistry and Life Science, United States Military Academy, West Point, NY 10996, USA. E-mail: samuel.cowart@westpoint.edu

<sup>c</sup> Photonics Research Center, United States Military Academy, West Point, NY 10996, USA

<sup>d</sup> Battery Science Branch, U.S. Army DEVCOM Army Research Laboratory, 2800 Powder Mill Road, Adelphi, MD 20783-1138, USA.  
E-mail: jan.l.allen8.civ@army.mil

<sup>e</sup> Department of Mechanical Engineering, The University of Alabama, Tuscaloosa, AL 35487, USA

<sup>f</sup> Department of Energy Engineering, Hanyang University, Seoul 04763, Republic of Korea

<sup>g</sup> Department of Battery Engineering, Hanyang University, Seoul 04763, Republic of Korea

<sup>†</sup> Co-first authors.



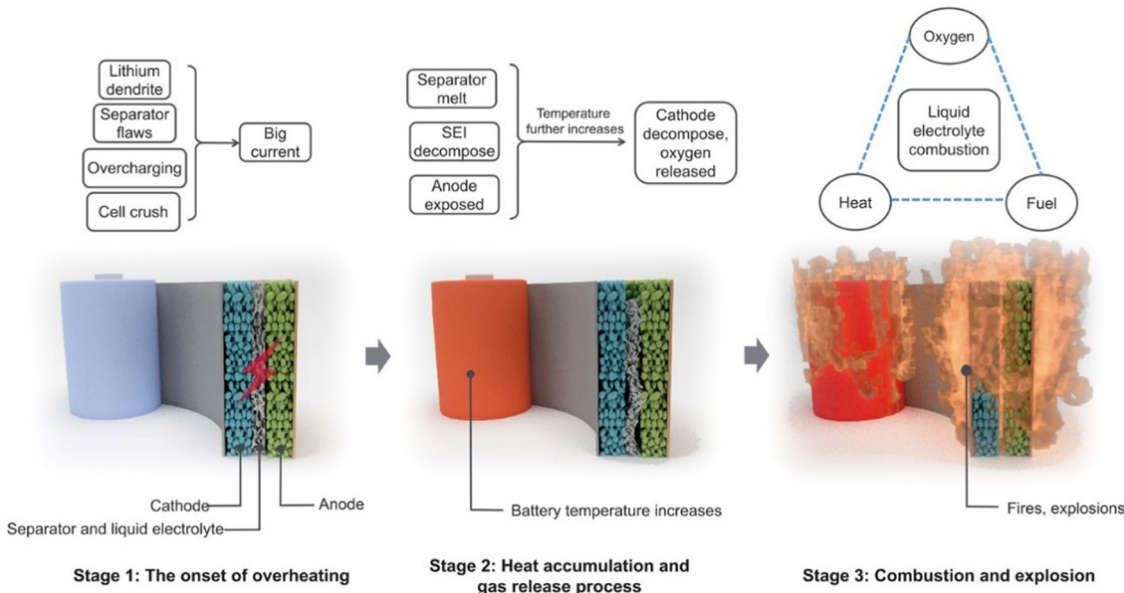


Fig. 1 The stages of thermal runaway in LIBs. Reproduced with permission from ref. 11. Copyright 2018, American Association for the Advancement of Science.

involving fire, smoke, or explosions. When thermal runaway occurs, it leads to the rapid release of stored energy, causing the battery to heat up dramatically, potentially leading to fire, explosion, and the release of toxic gases (Fig. 1).<sup>5</sup> Such events are triggered by various factors, including battery cell degradation, manufacturing defects, mechanical abuse, electrical abuse, and exposure to high temperatures.<sup>6</sup> Numerous high-profile safety incidents involving LIBs have occurred over the past decade. Notably, the Boeing 787 Dreamliner battery incidents in 2013, where two cases of battery fires led to the grounding of the entire Dreamliner fleet for several months.<sup>7</sup> Investigations revealed that internal short-circuiting within LIB cells, due to battery design flaws and manufacturing processes, caused the fires. Similarly, in 2016, the Samsung Galaxy Note7 smartphones were recalled after battery design flaws, such as faulty separators and electrodes, led to numerous reports of the devices catching fire or exploding. This caused significant financial and reputational damage for Samsung.<sup>8</sup> Moreover, in July 2020, in Surprise, Arizona, four firefighters were critically injured from the explosion of an LIB energy storage system (ESS).<sup>9</sup> In 2021, the Victorian Big Battery (300 MW/400 MW h) project in Australia reported a fire outbreak in a Tesla Megapack (MP-1) caused by an internal short circuit resulting from coolant leakage in the MP-1's cooling management system.<sup>10</sup> This leakage led to the overheating of the module's LIB cells, ultimately triggering a thermal runaway event and fire. The Surprise, Arizona, and Victorian Big Battery ESS fire incidents demonstrate the vulnerabilities of large-scale energy storage systems to thermal events and the potential for widespread damage where safety mechanisms fail.

The aforementioned cases highlight the pressing necessity of significant research efforts and design enhancements to

address the safety hazards in commercial applications. Several studies have reported the complex degradation mechanisms of LIB components to provide mitigation strategies. For instance, major cathode degradation has been identified to stem from the anisotropic volume expansion during charge/discharge cycles, particularly in Ni-rich layered cathodes when the Ni content exceeds 60%. Ryu *et al.*<sup>12</sup> investigated the capacity fading mechanisms in layered Ni-rich  $\text{Li}[\text{Ni}_x\text{Co}_y\text{Mn}_{1-x-y}]\text{O}_2$  cathodes with varying Ni content ( $0.6 \leq x \leq 0.95$ ) and found that while increasing Ni content improves discharge capacity, it also significantly reduces cycling stability, especially for compositions with  $x > 0.8$ . The degradation was primarily attributed to the anisotropic volume changes associated with the  $\text{H}_2 \rightarrow \text{H}_3$  phase transition, which causes significant internal stress within the cathode material owing to detrimental shrinkage in the lattice along the *c*-axis, leading to the formation and propagation of microcracks in the cathode particles.<sup>13-16</sup> These microcracks create penetration pathways for the electrolyte, exacerbating degradation by allowing the electrolyte to attack the newly exposed surfaces.<sup>17</sup>

Additionally, Wu *et al.*<sup>18</sup> investigated the degradation mechanisms of LIB cathode materials and observed that the performance degradation and thermal instability of Ni-rich layered LIB cathode materials occur at a surface level. They further observed that the original layered lattice structure of the material transforms into inactive and insulation NiO-like rock-salt near the surface due to the oxidation of the electrode surface contacting the electrolyte by strongly oxidizing  $\text{Ni}^{3+4+}$ , a phenomenon also discussed by Ryu *et al.*<sup>12</sup> The degradation of cathodes is primarily linked to the instability of the crystal structure. However, the degradation mechanisms vary significantly depending on the specific cathode material, each



undergoing distinct pathways that ultimately contribute to crystal structure instability. These varying mechanisms will be explored in detail in the subsequent sections.

Similarly, researchers have also investigated the degradation of anode materials. The degradation mechanisms of anodes vary by material. For instance, Li metal anodes suffer from dendrite formation and parasitic reaction of the Li with the electrolyte.<sup>19</sup> Graphite degrades due to solvent co-intercalation, structural disordering, dissolved transition metal cation plating, and Li plating/dendritic growth.<sup>20–22</sup> Silicon degrades because of repeated volume expansion and contraction during charge and discharge cycles, leading to mechanical stress, cracking, delamination, and pulverization of the silicon particles, resulting in loss of electrical contact, increased impedance, and rapid capacity fading.<sup>23–26</sup>

Electrolyte degradation is also a critical factor in the overall deterioration of LIBs. The mainstream electrolytes in commercial LIBs are carbonate-based, consisting of a Li salt dissolved in organic solvents.<sup>27,28</sup> While battery electrolytes are favored for their compatibility with common anode and cathode materials and their wide electrochemical stability window, they are thermally unstable.<sup>27</sup> Notably, LiPF<sub>6</sub> decomposes into reactive species, such as PF<sub>5</sub> and HF, which further react with the carbonate solvents, generating heat and gaseous byproducts.<sup>28,29</sup> This cascade of reactions increases internal pressure within the battery, heightening the risk of thermal runaway.

To address anode and electrolyte degradation as well as thermal instability concerns, various approaches have been considered. These approaches include the use of composite anodes, solid electrolyte interphase (SEI)-forming additives, solid electrolytes, and the development of aqueous electrolytes to tackle issues like graphite exfoliation, SEI decomposition, solvent co-intercalation, dendrite formation, PF<sub>5</sub> formation, thermal runaway, and toxic gas emissions.<sup>19,30–33</sup>

Overall, LIB component degradation is often perceived as a complex topic with multiple intertwined mechanisms occurring simultaneously. Therefore, this review aims to provide an in-depth yet comprehensive summary of the current state-of-the-art knowledge on the degradation mechanisms of key LIB components—cathode, anode, and electrolyte—and the factors that trigger or exacerbate such wear-downs. Furthermore, this safety-focused review will offer insights into recent strategies that enhance the safety and reliability of these batteries and discuss practical requirements recommended for LIB applications from the viewpoint of first responders, thus contributing uniquely to the existing literature on LIB degradation pathways and thermal instabilities.

The first section of the paper details the electrochemical and physicochemical properties of various widely used cathode, anode, and electrolyte materials. The second and third sections of this paper detail the complex and interdependent degradation mechanisms and abuse conditions of battery components that exacerbate thermal risks and trigger catastrophic cell failure. Particular attention is given to Ni-rich and Li-rich cathodes, as well as 5 V spinel cathodes, which are prone to oxygen

release—a catalyst for thermal runaways. Furthermore, we discuss the unique degradation mechanisms of silicon anodes' remarkable capacity albeit plagued by high-volume expansions and other materials such as graphite, conversion anodes, fast-charging anodes, and Li metal anodes. Given the role of electrolytes as a medium for ionic transport and their significant impact on thermal regulation, we also discuss the thermal stability and degradation of electrolytes—particularly carbonate, ether, and gel polymer electrolytes—addressing their susceptibility to decomposition and gas evolution under thermal stress, elucidating how electrolyte decomposition affects overall cell stability. The fourth section details recent strategies to enhance LIB safety using novel materials and approaches. To present a holistic and first-hand user perspective, the last sections of the review discuss application impacts and specific requirements that LIBs must meet for first responders. This includes considerations for high/fast charge–discharge rates, cycle life requirements, operating temperature ranges, system vibrations, mechanical loads in transportation (automotive, aircraft, small vehicles, drones), and specific challenges faced by first responders and military applications.

## 1. Electrochemical and physicochemical properties of LIB materials

### a. Cathode materials

i. **Ni-rich layered oxide materials (NCM/NCA).** NCM (nickel–cobalt–manganese) and NCA (nickel–cobalt–aluminum) are described by the general formula LiTMO<sub>2</sub> (TM = Ni, Co, Mn, Al, *etc.*) and crystallized in a rhombohedral  $R\bar{3}m$  space group.<sup>34</sup> These materials possess high energy density, excellent cyclability, rate capability, and versatility across various energy applications in EVs, ESS, and portable electronics. The structure of Ni-rich layered oxide cathodes is based on the  $\alpha$ -NaFeO<sub>2</sub> type layered structure consisting of alternating layers of Li and transition metal oxides.<sup>35</sup> The growing demand for higher energy densities has necessitated an increase in the Ni content within these materials, as the increase in Ni content directly translates to higher energy densities.<sup>36–38</sup> As a result, materials such as Li[Ni<sub>0.8</sub>Co<sub>0.15</sub>Al<sub>0.05</sub>]O<sub>2</sub> cathodes, commonly used in EVs, including those manufactured by Tesla, offer a high energy density and long cycle life.

With an increase in Ni content (Ni > 60%), state-of-the-art Ni-rich layered oxide materials achieve impressive energy densities of approximately 300 W h kg<sup>−1</sup> (ref. 39) in 4680 (46 mm in diameter, 80 mm in axial length) cylindrical cells, significantly surpassing those of traditional lithium cobalt oxide (LiCoO<sub>2</sub>). One attribute of the Ni-rich layered oxides is their high voltage, which typically ranges between 3.7 and 3.9 V *versus* Li/Li<sup>+</sup>.<sup>39</sup> This high voltage contributes to the battery's overall energy density, allowing for more energy storage within the same volume compared with other cathode materials. Additionally, the high Ni content contributes to an increase in the capacity because Ni provides multiple oxidation states (Ni<sup>2+</sup>/Ni<sup>3+</sup>/Ni<sup>4+</sup>)<sup>40</sup>



that facilitate electron transfer and  $\text{Li}^+$  intercalation during charge and discharge cycles. This enhanced electrochemical activity is further complemented by the stable layered structure of these oxides, which allows for a high degree of  $\text{Li}^+$  diffusion with minimal lattice distortion. Research has shown that tuning the properties of these cathode materials *via* lattice engineering and defect modulation using strategies such as concentration gradient and single particle engineering can significantly improve their structural stability, further minimizing lattice distortion and leading to excellent rate capability and cycling performance.<sup>41,42</sup>

The stability of Ni-rich layered oxides is bolstered by the careful balance of Ni with other elements like Co, Mn, and Al. Co plays a critical role in stabilizing the layered structure, preventing the  $\text{Li}^+/\text{Ni}^{2+}$  mixing, and improving the thermal stability of the material. This is particularly important for maintaining the integrity of the cathode during high-temperature operations, which is a common requirement for high-performance batteries. Conversely, Mn enhances structural stability and mitigates the harmful effects of phase transitions that can occur during cycling. In the case of NCA cathodes, Al is introduced to improve the mechanical robustness and thermal stability of the material. This balance of elements not only enhances the electrochemical properties of the cathode but also ensures that the material remains relatively stable and safe under various operating conditions.<sup>43-45</sup>

Despite the high energy density and stability shown by Ni-rich layered oxides, this enhancement in energy density is accompanied by rapid structural degradation, such as micro-cracks and deteriorative cathode/electrolyte interfaces that can lead to thermal runaway of the cathode material. This raises significant concerns regarding the safety and practical use of these Ni-rich layered oxides. The heightened energy density, while beneficial, exacerbates the intrinsic instability of Ni-rich layered oxides, leading to accelerated deterioration of the material's structure.<sup>46</sup>

**ii. Li-rich Layered oxide.** Another type of layered cathode material is the Li-rich layered oxide, denoted as  $x\text{Li}_2\text{MnO}_3(1-x)\text{LiTMO}_2$  (where TM = Mn, Ni, Co, or their mixture). The Li-rich layered oxide structure consists of a composite of the Li-excess  $\text{Li}_2\text{MnO}_3$  phase and the layered  $\text{LiTMO}_2$  phase (Fig. 2a and b), where the transition metal (TM) can be a combination of Mn, Ni, and Co. The emergence of Li-rich layered oxide cathode

materials has been a significant advancement in LIB technology, owing to their high theoretical specific capacity ( $>300 \text{ mA h g}^{-1}$ )<sup>47</sup> with a voltage window that typically ranges from 3.5 to 4.8 V *versus*  $\text{Li}/\text{Li}^+$ .<sup>48,49</sup> Furthermore, their high Li content reduces Co usage, a resource with environmental and ethical concerns associated with its mining, thereby bringing down the cost of the Li-rich layered oxide material and making it more environmentally friendly.<sup>50</sup>

Li-rich cathodes possess a layered crystal structure similar to conventional layered oxides like NCM. In these materials, Li and transition metals are arranged in alternating layers within the crystal lattice (Fig. 2c and d). The presence of excess Li in the structure beyond the stoichiometric ratio facilitates a dual redox mechanism involving both the transition metal ions and the oxygen anions. In conventional cathode materials, the capacity is primarily derived from the redox reactions of transition metals such as  $\text{Ni}^{3+}/\text{Ni}^{4+}$  or  $\text{Co}^{3+}/\text{Co}^{4+}$ .<sup>53</sup> However, in Li-rich materials, an additional redox activity involving oxygen anions ( $\text{O}^{2-}$ ) is activated.<sup>54</sup> The incorporation of  $\text{Li}_2\text{MnO}_3$  into the structure enables the activation of Mn ions from a tetravalent state to a trivalent state,<sup>55</sup> which, when combined with oxygen's redox activity, significantly boosts the material's overall capacity. The activation of the oxygen redox is made possible by the excess Li in the structure, which allows oxygen to participate in the electrochemical reactions to enable much higher capacities than its other layered cousin. Li-rich layered oxides also demonstrate impressive electronic conductivity, which, although inherently lower than some other cathode materials, can be significantly improved through strategic doping and surface modifications.<sup>56</sup>

One critical attribute of Li-rich layered oxide is its outstanding thermal stability. Its decomposition temperatures are significantly higher than those of traditional cathode materials.<sup>57</sup> This high thermal stability is attributed to the strong bonding within the layered structure and the robust lattice formed owing to the incorporation of  $\text{Li}_2\text{MnO}_3$ . The presence of Mn in a higher oxidation state ( $\text{Mn}^{4+}$ ) and its interaction with other transition metals contribute to this enhanced stability,<sup>58</sup> making Li-rich layered oxide capable of withstanding higher operational temperatures than Ni-rich layered oxides.

While Li-rich layered oxide boasts of high capacity and better thermal stability than Ni-rich layered oxide materials,

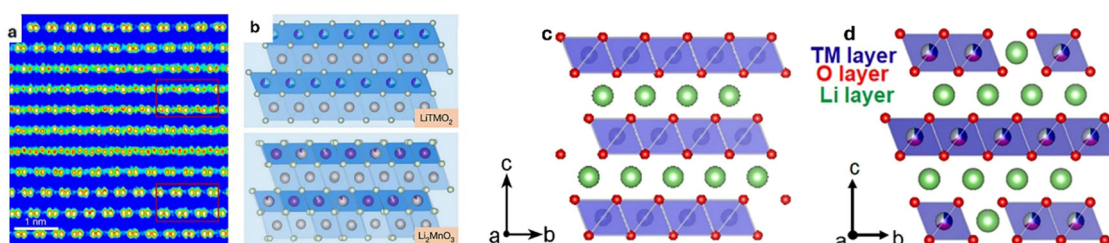


Fig. 2 (a) High-resolution TEM image, and (b) schematic structure of  $\text{LiTMO}_2$  and  $\text{Li}_2\text{MnO}_3$  domains. Reproduced with permission from ref. 51. Copyright 2024, The Author(s). Licensed under Creative Commons CC BY (<https://creativecommons.org/licenses/by/4.0/>). Structures of (c) Ni-rich layered oxide, (d) and Li-rich layered oxide. Reproduced with permission from ref. 52. Copyright 2021, Elsevier B.V.



these materials suffer from significant capacity loss, pronounced voltage hysteresis/fade, low initial Coulombic efficiency (ICE), and poor rate performance as highlighted by Zheng *et al.*<sup>59</sup> In particular, the voltage hysteresis and decay, which lead to energy insufficiency and continuous energy density loss during cycling, remain among the greatest challenges for the practical applications of Li-rich layered oxides.<sup>60,61</sup> This instability manifests primarily through structural degradation, capacity fading, and safety concerns under elevated temperatures and prolonged cycling.

**iii. 5 V Spinel.** The origins of 5 V Spinel can be traced back to the widely studied lithium manganese oxide (LMO) spinel, one of the early commercialized cathode materials for LIBs<sup>62</sup> with the chemical formula  $\text{LiMn}_2\text{O}_4$ . LMO was first introduced in the 1950s by Johnson and Heikes<sup>63</sup> as a promising cathode material due to its three-dimensional  $\text{Li}^+$  diffusion channels, which facilitate high-rate performance.<sup>64</sup> However, capacity fading issues especially at elevated temperatures, limited its long-term application. The transition from LMO to 5 V spinel cathodes involved modifying the chemical composition and crystal structure to increase the operating voltage and improve stability.<sup>65</sup>

In the initial studies on the first spinel structure,  $\text{LiMn}_2\text{O}_4$  in 1964 by Blasse,<sup>66</sup> it was demonstrated that the spinel structure of  $\text{LiMn}_2\text{O}_4$ , with  $\text{Li}^+$  and  $\text{Mn}^{3+}$  occupying tetrahedral and octahedral sites, respectively, delivered a theoretical specific capacity of  $148.2 \text{ mA h g}^{-1}$ . However, its practical application was limited by the Jahn-Teller distortion of  $\text{Mn}^{3+}$ , causing structural changes and capacity fading. Researchers addressed this by doping the spinel structure with divalent cations like Zn and Mg, which enhanced electroactivity at higher voltages. *In situ* XRD and XANES studies showed Mn ion oxidation during charging while Zn and Mg remained divalent. These findings linked lattice parameter shifts to electrochemical performance, laying the groundwork for high-voltage cathode materials. By partially substituting Mn with Ni, Co, or other transition metals, materials such as  $\text{LiNi}_{0.5}\text{Mn}_{1.5}\text{O}_4$  (LNMO) were synthesized (Fig. 3a and b). The most distinguished feature of LNMO is its remarkably high and flat voltage plateau at  $\sim 4.7 \text{ V}$  (vs.  $\text{Li}/\text{Li}^+$ ) that utilizes the entire redox capacity of Ni ( $\text{Ni}^{2+/4+}$ ). It has a remarkable energy density of  $\sim 650 \text{ W h kg}^{-1}$ .<sup>67</sup>

One of the key strengths of 5 V spinel cathodes is their exceptional rate capability, primarily attributed to the spinel

structure's three-dimensional  $\text{Li}^+$  diffusion channels.<sup>68,69</sup> The diffusion of  $\text{Li}^+$  occurs through the 8a tetrahedral and 16c octahedral sites with minimal lattice distortion, which is crucial for maintaining swift ion transport. However, LNMO's practical usage is still severely limited by parasitic reactions associated with its extremely oxidative operating conditions, including the absence of a stable electrolyte at 5 V and TM dissolution, which are further exacerbated under storage or operation at elevated temperatures.

**iv.  $\text{LiFePO}_4$ .** The  $\text{LiFePO}_4$  (LFP) cathode material is known for its exceptional safety, long cycle life, and environmental advantages. LFP was first identified in 1950 by Destenay<sup>70</sup> in the minerals triphyllite and lithiophilite. In 1996, John B. Goodenough and co-workers<sup>71</sup> demonstrated the electrochemical extraction and insertion of Li from LFP, marking a significant milestone. They showed that the olivine structure of LFP provided excellent thermal stability and safety, making it a promising candidate for LIB cathodes. However, its low electrical conductivity posed a challenge, and carbon coating and dopants were incorporated to increase conductivity, along with nanosizing of the LFP for faster charge transport.<sup>72-75</sup>  $\text{Li}^+$  diffusion mechanism in LFP occurs through the one-dimensional channels in the olivine structure. These channels, aligned along the [010] direction, allow  $\text{Li}^+$  to move in and out during charge and discharge cycles, contributing to the material's stability and performance.<sup>76</sup> The theoretical specific capacity of LFP is approximately  $170 \text{ mA h g}^{-1}$ ,<sup>77</sup> which, while lower than that of other cathode materials like NCM, is sufficient for many applications due to LFP's superior safety aspect. Furthermore, LFP exhibits high Coulombic efficiency, often exceeding 99%,<sup>78</sup> indicating minimal energy loss during the charge/discharge cycles and underscoring its suitability for long-term use.

Despite their well-deserved reputation for safety, LFP cathodes are not entirely immune to thermal instability concerns. While they exhibit superior thermal stability compared to other LIB chemistries, certain factors can still trigger a potentially dangerous chain reaction within the battery, leading to thermal runaway. This phenomenon can lead to a rapid rise in temperature, potentially resulting in fire or explosion. Furthermore, the flat voltage plateau at  $\sim 3.2 \text{ V}$  makes it difficult for the battery management system (BMS) to detect the state of charge (SOC).

A high SOC, particularly at 100%, can lead to higher internal energy and heat transfer power, exacerbating thermal

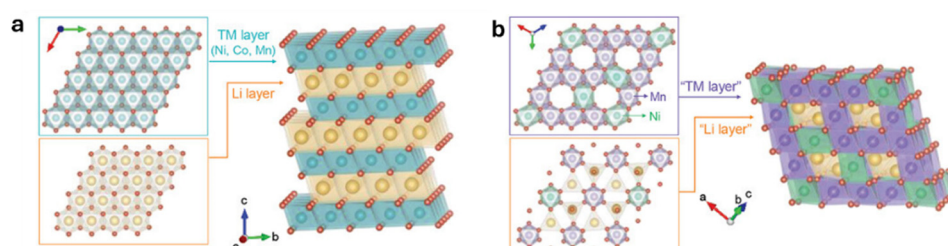


**Fig. 3** A side-by-side comparison between (a) a typical Ni-based NCM, and (b) the spinel 5 V cathode in terms of structural feature. Reproduced with permission from ref. 62. Copyright 2024, The Authors. Advanced Materials published by Wiley-VCH GmbH.



instability. External heat sources and heat conduction between cells during thermal runaway propagation can also contribute to the risk. Yang *et al.*<sup>79</sup> in their comparative study on aging and thermal runaway of commercial LFP/graphite batteries undergoing slight overcharge cycling, explored how slight overcharge cycling affects the aging mechanism and thermal runaway behavior of LFP batteries. They found that overcharging accelerates capacity fading due to Li loss, with a higher risk of internal short circuits and worsened thermal stability. Zhang *et al.*<sup>80</sup> using differential scanning calorimetry tests revealed that the LFP cathode exhibits high thermal stability, while the graphite anode reacts violently with the electrolyte, to produce significant heat. It was established that the key reactions include SEI decomposition, lithiated graphite reaction with electrolyte, and binder reactions at higher temperatures. Key findings indicate that onset temperatures for exothermic reactions can be as low as 70.6 °C, with significant heat and gas venting observed around 200 °C. Understanding these mechanisms is crucial for enhancing the safety of LFP batteries in applications like EVs and ESS. Song *et al.*<sup>81</sup> investigated the thermal runaway propagation behavior and energy flow distribution of a 280 A h LFP battery. Their experiments revealed that thermal runaway propagation occurs primarily at 100% SOC, driven by higher internal energy and heat transfer power. Chen *et al.*<sup>82</sup> conducted an experimental investigation of thermal runaway behavior and hazards of a 1440 A h LFP battery pack. They analyzed the thermal runaway propagation process, finding that heat conduction between batteries becomes the main factor as thermal runaway develops. Their findings provide insights into the implementation of firefighting and flame-retardant strategies. Qian *et al.*<sup>83</sup> examined the thermal runaway vent gases from high-capacity energy storage LFPs. They focused on the composition of gases released during thermal runaway, identifying key components such as CO, H<sub>2</sub>, and CO<sub>2</sub>, which pose significant hazards.

While LFP also undergoes thermal degradation, it does so to a much lesser extent compared to Li-rich, Ni-rich, and 5 V spinel cathodes. Due to its inherently stable structure, LFP is still considered a safe and reliable material. However, given that LFP has a lower capacity than these other cathodes, this paper will not delve into further discussions on the degradation mechanisms and strategies for improving LFP. Instead, the focus will be on higher-capacity materials such as Li-rich, Ni-rich, and 5 V spinel cathodes, which present more significant opportunities and challenges for performance enhancement.

## b. Anode materials

**i. Silicon.** Silicon (Si) is widely recognized as one of the most promising anode materials for next-generation LIBs due to its exceptional capacity for Li<sup>+</sup> storage. The diamond cubic crystal structure of Si allows it to accommodate substantial quantities of Li<sup>+</sup> within its lattice, contributing to its impressive theoretical capacities. 4200 mA h g<sup>-1</sup> as Li<sub>22</sub>Si<sub>5</sub> at 415 °C and 3579 mA h g<sup>-1</sup> as Li<sub>15</sub>Si<sub>4</sub> at room temperature.<sup>84-86</sup> Moreover, the high theoretical capacity of silicon allows the reduction of

the electrode thickness without sacrificing the integral energy density.<sup>87</sup>

During the lithiation process though, significant structural phase transitions occur. These transitions undergo multiple crystalline phase transformations, including Li<sub>Si</sub>, Li<sub>12</sub>Si<sub>7</sub>, Li<sub>7</sub>Si<sub>3</sub>, Li<sub>13</sub>Si<sub>4</sub>, Li<sub>15</sub>Si<sub>4</sub>, and Li<sub>22</sub>Si<sub>5</sub>.<sup>85,88,89</sup> The initial lithiation stage involves the formation of an amorphous Li<sub>x</sub>Si phase, which transitions to the crystalline phases below 50 mV.<sup>85</sup> The crystalline phases are generally more kinetically stable due to their lower formation energies but not always preferentially formed during typical electrochemical lithiation under normal operating conditions.<sup>88</sup> The potential for these phase transitions varies, but Li<sup>+</sup> alloying in Si anodes occurring at a low potential range of 0.01–0.5 V vs. Li/Li<sup>+</sup> at room temperature<sup>85</sup> plays a crucial role in the battery's performance. A low lithiation potential enables efficient alloying, significantly contributing to the high energy density of the battery. However, while the low lithiation potential is advantageous for maximizing energy density, it can increase the risk of Li plating, as the low discharge potential of Si, below 0.4 V vs. Li/Li<sup>+</sup>, is lower than that of other alloy-type, carbonaceous, or metal oxide anodes.<sup>84,86,89</sup> Conversely, the low discharge potential allows for a higher overall cell voltage when paired with high-voltage cathodes during LIB operation, maximizing the energy density of the battery. Moreover, lithiated Si is reported to be considerably less reactive than graphite, offering better chemical stability across a wider range of electrolytes.

Currently, the practical application of pure Si or high Si-anodes is hindered by significant volume expansions during lithiation/delithiation, leading to material fracturing, pulverization, and delamination from current collectors. This results in poor cycling performance and low electronic conductivity. To mitigate these issues, research has increasingly focused on Si-containing composites, such as silicon-graphite/carbon blends, and Si-based derivatives like silicon oxide (SiO<sub>x</sub>). These composites offer a more balanced performance by reducing volume change, improving mechanical stability, and enhancing cycle life, making the use of Si as an anode material more suitable for practical high-energy batteries.<sup>90</sup> Owing to these, recent studies,<sup>91</sup> have demonstrated that Si-based composites, especially those integrated with carbonaceous materials like artificial graphite, significantly enhance the electrochemical performance of Si anodes. This composite offers better cycling stability and rate capability, delivering a specific capacity of 445 mA h g<sup>-1</sup> and 94% retention over 200 cycles. Pan *et al.*<sup>92</sup> demonstrated the advantage of SiO, another class of Si-derived anodes. Their study highlighted that SiO anodes offer significantly lower volume expansion (~118%) compared to pure Si (~280%), leading to improved mechanical stability and durability during cycling. SiO also demonstrates superior rate capabilities, excelling in both fast-charging and fast-discharging due to enhanced Li<sup>+</sup> diffusion facilitated by the Li<sub>4</sub>SiO<sub>4</sub> matrix. Future innovations in Si-anode technology will be pivotal in unlocking its full potential in LIB applications. In subsequent sections, novel strategies aimed at improving the



performance of this promising anode material will be discussed extensively.

**ii. Conversion anodes.** Conversion-type anodes are another promising class of materials for next-generation LIBs, primarily due to their chemical and physicochemical properties that distinguish them from conventional intercalation-type (graphite) and alloying-type (silicon) anodes.

Conversion anode materials consist of transition metal oxides, sulfides, selenides, fluorides, nitrides, and phosphides that store  $\text{Li}^+$  through reversible conversion redox reactions between the  $\text{Li}^+$  and TM cations,<sup>25</sup> resulting in the formation and decomposition of metal nanoparticles embedded in a Li compound matrix (ex:  $\text{Li}_2\text{O}$  in the case of TM oxides).<sup>93</sup> This reaction mechanism offers several advantages over traditional intercalation-based anodes by enabling the storage of more  $\text{Li}^+$ , achieving higher specific capacities of 500–1500  $\text{mA h g}^{-1}$ . Poizot *et al.*<sup>93</sup> reported in 2000 that  $\text{Li}^+$  can be reversibly stored by conversion anodes and demonstrated that these materials could deliver exceptionally high capacities. For example, CoO was shown to exhibit capacities of around 700  $\text{mA h g}^{-1}$ , which is approximately twice that of graphite anodes. This is because the conversion reaction involves multiple electrons per formula unit, unlike intercalation materials that typically involve only one or two electrons.<sup>94</sup> Additionally, conversion anodes can maintain a significant portion of their capacity after cycling, albeit with nano structuring and material engineering. For instance, nano-sized CoO showed excellent capacity retention even after 100 cycles, retaining 85% of its capacity even at 2C.<sup>93</sup> Furthermore, the higher operating voltage range of 0.5 to 1.0 V *vs.*  $\text{Li}/\text{Li}^+$  reduces the risk of Li plating and dendrite formation, translating to enhanced safety and stability.<sup>95</sup>

The chemistry of conversion-type anodes also allows for the tuning of their electrochemical potential because the cell potential is directly linked to the strength of the ionic bond between the TM cation and anionic species.<sup>94</sup> These materials can also be engineered into nanostructures, such as nanoparticles, nanowires, and nanosheets, to enhance their electrochemical activity.<sup>25</sup> Nanosizing reduces the diffusion distances for  $\text{Li}^+$  and electrons, thereby improving the kinetics of the conversion reactions. Nanostructuring reduces the volume changes associated with conversion reactions. By designing hierarchical or hollow nanostructures, it is possible to accommodate the strain induced by these volume changes, thereby enhancing the cyclability of the conversion anode materials. The Li storage performance of some nano-structured and hollow conversion anode is given in Table 1.

**iii. Graphite.** Graphite is the most commonly used anode material due to its stable electrochemical performance, decent specific capacity (372  $\text{mA h g}^{-1}$ ),<sup>102</sup> and cost-effectiveness. Graphite is characterized by an ordered graphene layer stacked in ABABA with a suitable interlayer spacing of 0.335 nm. These  $\text{sp}^2$  hybridized graphene layers are linked by weak van der Waals forces and  $\pi$ - $\pi$  interactions. The layered structure gives rise to flake-like particles with basal and prismatic planes, with the latter being more reactive.<sup>103</sup> This structure causes anisotropy in graphite's properties, with high conductivity along the basal planes but much lower conductivity perpendicular to them. The weak van der Waals forces facilitate  $\text{Li}^+$  intercalation, making graphite a highly efficient and widely used anode material in energy storage systems.<sup>103,104</sup> This property has positioned graphite as an exceptional anode material for LIBs.

In terms of contribution to final energy density on a full-cell level, graphite is superior to common anodes because of its low average de-/lithiation potential of 0.2 V *vs.*  $\text{Li}/\text{Li}^+$ ,<sup>103</sup> which is only surpassed by metallic Li. The Coulombic efficiency of graphite, which is associated with voltage hysteresis—the discrepancy between the discharge and charge potentials—is another important factor contributing to its commercial dominance.<sup>103</sup> Although there has been some progress in lowering voltage hysteresis for materials of the conversion and alloying types, particularly with pre-lithiation and restricting delithiation to small potential ranges, graphite continues to provide a better balance of energy density and efficiency.

Graphite's slow kinetics under high charge/discharge rates, however, limit its fast-charge applications. Improving its structure and morphology can extend its use in fast-charging applications. Methods such as increasing the interlayer spacing of graphite, creating porous structures to shorten  $\text{Li}^+$  diffusion paths, and making interfacial modifications to enhance  $\text{Li}^+$  diffusion within the material have been effective.<sup>104</sup>

**iv. Metallic Li.** Li metal is widely regarded as a promising anode material for next-generation LIBs, primarily due to its low electrochemical potential and exceptional theoretical capacity of 3860  $\text{mA h g}^{-1}$ , which substantially surpasses that of conventional materials such as graphite. The electrochemical potential of Li metal at –3.04 V *vs.* standard hydrogen electrode (SHE) enables high cell voltages when paired with various cathode materials. This potential is significantly higher than conventional graphite anodes, making Li metal particularly attractive for applications requiring high energy output, such as electric vehicles and portable electronics.<sup>105,106</sup>

**Table 1** Electrochemical properties of different conversion type anode materials

Classification	Typical example	Voltage plateau (V <i>versus</i> $\text{Li}/\text{Li}^+$ )	Capacity ( $\text{mA h g}^{-1}$ )	Current density ( $\text{mA g}^{-1}$ )
0D to 3D nanostructures	$\text{CuP}_2$ nanowires <sup>96</sup>	0.6	945 after 100 cycles	100
Hierarchical configurations	$\text{Co}_3\text{O}_4$ nanosheets <sup>97</sup>	1.0	1291 after 25 cycles	445
	$\text{MoS}_2$ nanospheres <sup>98</sup>	0.6	1096 after 110 cycles	100
Hollow structures	$\text{MnCo}_2\text{O}_4$ nanosheet array <sup>99</sup>	0.8	460 after 30 cycles	800
	$\text{Fe}_3\text{O}_4$ hollow spheres <sup>100</sup>	0.7	1046 after 100 cycles	500
	$\text{MoS}_2$ nanotube <sup>101</sup>	0.6	839 after 50 cycles	100



From a physicochemical perspective, Li metal stands out due to its exceptionally low density of  $0.534 \text{ g cm}^{-3}$  among all metals.<sup>107</sup> This property significantly enhances its specific energy, making Li metal batteries highly appealing for weight-sensitive applications. Its body-centered cubic (bcc) crystal structure also facilitates relatively easy ion diffusion, supporting efficient charge–discharge cycles.<sup>108</sup> Additionally, Li's low density contributes to its mechanical softness and flexibility, allowing it to be easily shaped into thin electrodes or novel cell designs for commercial production. Li metal's low density also imparts mechanical softness and flexibility, allowing Li metal to be easily formed into thin electrodes or novel cell architectures for commercial use.

However, the practical application of Li metal anodes is historically limited by issues such as dendrite formation and SEI instability. During cycling, the formation and dissolution of Li deposits occur on the anode surface due to uneven or localized Li deposition, potentially leading to the formation of dendritic(needle-like) structures. These dendrites pose the risk of penetrating the separator, potentially causing internal short circuits and presenting significant safety hazards.<sup>109,110</sup> To address these issues, recent research has focused on developing advanced electrolytes, protective coatings, and novel architectures to stabilize the Li metal surface and improve its electrochemical performance. These strategies will be discussed in-depth in Section 4.

**v. Fast-charging anodes.** Fast charging, as defined by the United States Advanced Battery Consortium (USABC), is characterized by the ability to achieve an 80% SOC within 15 minutes (4C rate).<sup>111</sup> Achieving this benchmark has been particularly challenging due to the significant stress that accelerated charging imposes on anode materials, leading to rapid degradation in performance and cycle life. As of 2021, EVs such as the Tesla Model 3 and Porsche Tycan are currently leading in fast charging capability, with the Tesla charging to 80% SOC in 27 minutes and the Porsche Tycan charging from 5% to 80% SOC in 23 minutes. While these vehicles have impressive fast

charging capabilities, they still fall short of the USABC's specified conditions.<sup>112</sup>

The spinel  $\text{Li}_4\text{Ti}_5\text{O}_{12}$  (LTO) offers fast-charging capability with high Li kinetics due to its higher intercalation potential of approximately 1.5 V *versus*  $\text{Li}^+/\text{Li}$ , which prevents the formation of a SEI layer and mitigates Li metal plating.<sup>113,114</sup> LTO anodes are characterized by a zero-strain insertion process and undergo minimal volumetric change, making them highly durable and resistant to mechanical degradation.<sup>115</sup> However, LTO is limited by a low Li intercalation capacity of  $\sim 160 \text{ mA h g}^{-1}$ .<sup>116,117</sup> To address this limitation, Nb-based Wadsley–Roth structure-based anodes, which feature  $\text{ReO}_3$ -like blocks connected in various configurations to enhance capacity and performance, were developed (Fig. 4).

Wadsley–Roth structures are mixed-valence metal oxides with flexible, non-stoichiometric frameworks derived from the  $\text{ReO}_3$  structure. These materials feature oxygen vacancies and ion-conducting pathways, allowing for rapid ion migration. Their structural adaptability and ability to support multiple redox states make them ideal for fast-charging battery anodes, enabling efficient ion insertion and extraction while maintaining cycling stability.<sup>119–121</sup>

Han *et al.*<sup>114</sup> introduced a new Li-insertion anode material,  $\text{TiNb}_2\text{O}_7$  (TNO), which operates within a voltage range of 1.3–1.6 V *versus*  $\text{Li}^+/\text{Li}$ . The Wadsley–Roth shear structure provides significant advantages for fast charging by preventing the formation of an SEI layer. With a theoretical capacity of  $387.6 \text{ mA h g}^{-1}$  that is enabled by overlapping redox couples, the material's performance is further improved by substituting Nb for Ti and applying a carbon coating. Allen *et al.*<sup>118</sup> investigated the potential of  $\text{NaNb}_{13}\text{O}_{33}$  as an anode material for fast-charging batteries and reported a capacity of  $233 \text{ mA h g}^{-1}$  when cycling between 3.0 V and 1.0 V, along with high  $\text{Li}^+$  conductivity and superior rate capability. The structure of  $\text{NaNb}_{13}\text{O}_{33}$ , consisting of  $\text{NbO}_6$  octahedra arranged in a Wadsley–Roth framework, allows for efficient  $\text{Li}^+$  transport due to large open channels. Electrochemical measurements using

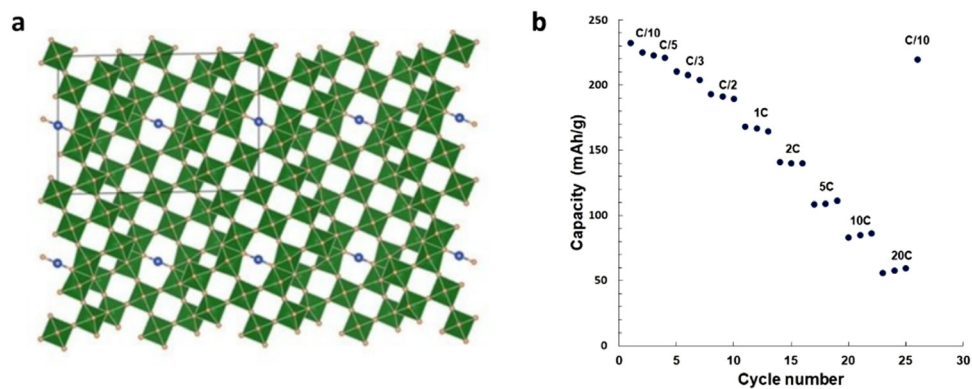


**Fig. 4** (a) Crystal structure of  $\text{NaNb}_{13}\text{O}_{33}$  viewed down the  $b$ -axis. Green octahedra represent Nb-centered  $\text{NbO}_6$ . Na atoms are in blue, O atoms in orange. (b) Delithiation capacity as a function of the rate of  $\text{NaNb}_{13}\text{O}_{33}$  with high-rate capability up to 20C in a Li metal half-cell at the indicated charge–discharge rates. Reproduced under the terms of the Creative Commons CC BY license.<sup>118</sup> Copyright 2023, The Authors. ChemElectroChem published by Wiley-VCH GmbH.



PITT and EIS confirmed the superior diffusion rates of Li within  $\text{NaNb}_{13}\text{O}_{33}$ . Preefer *et al.*<sup>122</sup> investigated the electrochemical behavior of  $\text{PNb}_9\text{O}_{25}$  (PNO) and demonstrated that the material can support high-rate charging by undergoing an insulator-to-metal transition upon Li insertion, contributing to its notable performance. The study indicates that PNO can attain 85% of its theoretical capacity within 30 minutes, resulting in an efficient charge–discharge cycle with excellent capacity retention. Although Wadsley–Roth structured anodes show promise for fast-charging applications, they often experience capacity fading over extended cycles, highlighting the need for improvements in cycle life before they can be viable for practical use. Many of these anode materials are still in the experimental phase and require further development and optimization. Additionally, they heavily rely on high-cost transition metals.

### c. Electrolytes

**i. Carbonate electrolytes.** Carbonate electrolytes are the most used electrolytes in LIBs due to their well-balanced physicochemical and electrochemical properties. These electrolytes typically consist of Li salts, notably lithium hexafluorophosphate ( $\text{LiPF}_6$ ), dissolved in a mixture of aliphatic carbonates—cyclic and linear carbonate solvents. Common solvents include diethyl carbonate (DEC), ethylene carbonate (EC), propylene carbonate (PC), dimethyl carbonate (DMC), and ethyl methyl carbonate (EMC).<sup>27,28</sup> Each organic solvent used in the formulation of carbonate electrolytes offers a mix of strengths and weaknesses. The physical properties of commonly used carbonate solvents are given in Table 2.

As the table shows, cyclic and linear carbonates differ significantly in their physicochemical properties. Cyclic carbonates, such as EC, PC, and FEC, are characterized by high dielectric constants, which are crucial for dissolving Li salts effectively and ensuring a stable SEI on the anode surface. The high flash points, low volatility, and boiling points also contribute to their thermal stability. EC has an extremely high dielectric constant (89.8) and is essential in forming a robust SEI on graphite anodes when it decomposes at 0.8 V *vs.*  $\text{Li}/\text{Li}^+$ .<sup>125</sup>

This makes it a crucial cyclic carbonate in LIB applications.<sup>125</sup> However, with a melting point of  $\sim 37$  °C, EC is a solid at room temperature and easily solidifies when used as a solvent in low-temperature electrolyte formulations,<sup>126</sup> severely impacting its ionic conductivity.

To overcome this limitation, linear carbonates are used as co-solvents to improve the performance of electrolyte mixtures,

allowing a more balanced electrolyte formulation. It is also noteworthy that although PC and EC have comparable physicochemical properties and molecular structures, PC is known to co-intercalate into graphite layers more readily than other carbonate solvents, leading to the mechanical instability of PC-based SEIs.<sup>126</sup> Due to the importance of SEI and anode stability in  $\text{Li}^+$  chemistry, this limits the application of PC in commercial electrolyte formulations. Among the cyclic carbonates, FEC is widely recognized for its ability to decompose and form SEI layers with the desirable LiF which has an ionic conductivity of  $10^{-7}$  to  $10^{-13}$  S cm<sup>-1</sup>.<sup>127</sup> Furthermore, VC is often used as an additive in carbonate electrolyte formulations because of its lower reduction activation energy compared to EC. This property allows the early formation of a stable SEI before the onset of  $\text{Li}^+$  intercalation.<sup>128</sup>

Linear carbonates, such as DMC, DEC, and EMC, have lower viscosities, dielectric constants, flashpoints, and melting points<sup>129</sup> but are essential in improving the wettability, viscosity, and ionic conductivity of the electrolyte. Using low-viscosity solvents alone, however, leads to issues with Li salt solubility, SEI stability, and most importantly flammability. Thus, a balanced mixture of cyclic and linear carbonates is often employed. By mixing these solvents, the merits of individual solvents are imparted on the resultant electrolyte mixture. For instance, a mixture of EC and DMC benefits from the low viscosity of DMC, which enhances ionic conductivity, and the high dielectric constant of EC, which facilitates the dissolution of Li salts and the formation of stable SEIs.<sup>123</sup> From an electrochemical perspective, carbonate electrolytes offer a wide electrochemical stability window, typically between  $\sim 1.5$ –4.5 V *vs.*  $\text{Li}/\text{Li}^+$  and high ambient-temperature ionic conductivity of  $\sim 10^{-2}$  S cm<sup>-1</sup>,<sup>130</sup> making them compatible with both high-voltage cathodes and low-potential anodes like graphite.

The choice of Li salt in carbonate electrolytes also plays a significant role in the overall electrolyte performance, making the properties of Li salts crucial.  $\text{LiPF}_6$  is favored in commercial carbonate electrolytes due to its high ionic conductivity. For instance,  $\text{LiPF}_6$  in EC/DEC or EC/DMC electrolyte formulations yield ionic conductivities up to  $10^{-2}$  S cm<sup>-1</sup> with oxidation potential  $>4.5$  V *vs.*  $\text{Li}/\text{Li}^+$ .<sup>128</sup> However, the thermal property is a challenge for carbonate electrolytes, prompting increased interest in alternative salts, such as lithium bis(trifluoromethansulfonyl)imide (LiTFSI) and lithium bis(fluoromethansulfonyl)imide (LiFSI). These salts offer excellent thermal stability, lower toxicity, and decent

Table 2 Physical properties of commonly used carbonate solvents<sup>27,123,124</sup>

Solvent	Flash point (°C)	Boiling point (°C)	Melting point (°C)	Density@25 °C (g cm <sup>-3</sup> )	Viscosity@25 °C (cP)	Dielectric constant (ε)
Ethylene carbonate (EC)	160	238	36.4	1.32	1.90 (40 °C)	89.8
Propylene carbonate (PC)	132	242	-48.8	1.20	2.53	66.1
Fluoroethylene carbonate (FEC)	120	249	18	1.48	4.1	79.7
Vinylene carbonate (VC)	130	162	22	1.35	1.54	126
Dimethyl carbonate (DMC)	17	90	4.6	1.06	0.59 (20 °C)	3.1
Diethyl carbonate (DEC)	25	127	-74.3	0.97	0.75	2.8
Ethyl methyl carbonate (EMC)	27	108	-53	1.01	0.65	2.4



electrochemical properties, along with providing a more inorganic-rich SEI layer.<sup>128</sup> However, the application of LiTFSI is hindered by its corrosive reaction with Al foil, which is typically used as a current collector in LIBs.<sup>128</sup> Therefore, the tradeoffs in the cost and electrolyte properties must be carefully considered when switching from LiPF<sub>6</sub> to LiTFSI/LiFSI or other Li salts.

**ii. Ether electrolytes.** Ether-based electrolytes have emerged as a more compatible and effective alternative to conventional carbonate electrolytes for Li metal anodes (LMAs). In LIBs, the most common ether electrolytes consist of dimethoxyethane (DME), tetraethylene glycol dimethyl ether (TEGDME), dioxolane (DOL), and tetrahydrofuran (THF).<sup>131</sup> The physical properties of these commonly used ether solvents are given in Table 3.

The compatibility of these solvents with LMAs is primarily attributed to their high donor numbers and effective Li<sup>+</sup> solvation ability. Barchasz *et al.*<sup>133</sup> highlighted the critical role of this Li<sup>+</sup> solvation ability and the high donor number (DN) of ether-based electrolytes. Ether solvents like TEGDME with relatively high donor numbers (DN = 18.6) were shown to solvate Li<sup>+</sup> better, creating a solvation environment that not only enhances ionic conductivity but also accelerates the passivation of the anode surface, thereby extending battery life.

The low viscosities and stability of ether solvents play a crucial role in minimizing electrolyte decomposition and suppressing dendrite formation, resulting in improved Coulombic efficiency (CE) and cycling stability when paired with LMAs.<sup>134,135</sup> Park *et al.*<sup>135</sup> conducted *ab initio* and statistical simulations to investigate why ether solvents are particularly compatible with LMAs. They found that the low reduction potentials of these solvents (ex: DME = -1.68 V vs. Li/Li<sup>+</sup>) are crucial to their stability, which reduces the likelihood of electrolyte decomposition with highly reactive Li metal. This stability is essential for maintaining a stable SEI and preventing dendrite formation. The study also emphasized the significant impact of low viscosity and salt anion size on dendrite suppression. This was demonstrated by the extended short-circuiting time of Li symmetric cells cycled in 1 M LiTFSI in DME, a low-viscosity solvent (Table 3). It was observed that the larger TFSI<sup>-</sup> anion (radius = 0.326 nm) contributes to higher Li<sup>+</sup> transference numbers, which promotes uniform Li deposition and further reduces the formation of dendrites.

**iii. Gel polymer electrolytes.** Gel polymer electrolytes (GPEs) have attracted significant attention owing to their favorable intrinsic properties such as mechanical stability, improved safety, lightweight, and reliability.<sup>136</sup> GPEs combine

the mechanical stability of solid polymers with the ionic conductivity of liquid electrolytes. The concept of GPEs was first proposed by Feuillade and Perche<sup>137</sup> in 1975 and typically consists of a liquid plasticizer in a polymer–salt system, which immobilizes large quantities of liquid plasticizers (electrolytes) within its network. To date, two main classes of plasticizers are commonly used—low molecular weight organic solvents and ionic liquids, of which organic solvents are the most reported.<sup>138,139</sup> The unique structure of GPEs reduces the crystalline content of the polymer matrix and lowers the barrier to ionic mobility.<sup>140</sup> The polymer matrix in GPEs are commonly made from poly(vinylidene fluoride) (PVDF), poly(vinylidene fluoride-*co*-hexafluoropropylene)-*m* (PVDF-HFP), poly(acrylonitrile) (PAN), poly(vinyl chloride) (PVC), poly(propylene carbonate) (PPC), poly(ethylene oxide) (PEO), and poly(methyl methacrylate) (PMMA).<sup>141–143</sup>

The polymer matrix plays a crucial role in defining the mechanical strength profile of GPEs, offering superior mechanical properties, such as tensile strengths exceeding 10 MPa in some GPEs<sup>144</sup> to tolerate the volume changes of electrodes. The flexible nature of the polymer matrix in GPEs enables them to accommodate the formation and growth of Li dendrites. Additionally, GPEs can function as both an electrolyte and a separator,<sup>145</sup> further enhancing their utility by providing a dual-function component that prevents short circuits and ensures reliable operation.

Compared to conventional solid polymer electrolytes (SPES), the improved ionic conductivity of GPEs at room temperature is largely attributed to the incorporation of a liquid electrolyte (plasticizer) within the polymer matrix that plays a significant role in determining ionic conductivity and thermal stability. For instance, GPEs with PVDF-HFP as the matrix have demonstrated high ionic conductivity, typically in the range of 10<sup>-3</sup> S cm<sup>-1</sup>,<sup>144,146</sup> which is comparable to conventional liquid electrolytes. GPEs also offer a wide electrochemical stability window, often up to 4.3 V *versus* Li<sup>+</sup>/Li.<sup>144</sup>

Properties such as a low glass transition temperature ( $T_g$ ), high decomposition temperature, and high melting temperature of the polymer matrix are also important properties for selecting a polymeric host for GPE application in LIBs, as these properties significantly affect the thermal behavior of GPEs.<sup>142</sup> The chemical structure of the polymeric host also affects the behavior of GPEs, especially their thermal behavior. As such, the unique combination of high ionic conductivity, mechanical stability, enhanced safety, and the ability to function as both an electrolyte and separator provided by GPEs makes them ideal candidates for the next generation of LIBs. Their ability to

Table 3 Physical properties of commonly used ether solvents<sup>27,123,132</sup>

Solvent	Flash point (°C)	Boiling point (°C)	Melting point (°C)	Density@25 °C (g cm <sup>-3</sup> )	Viscosity@25 °C (cP)	Dielectric constant (ε)
Dimethoxyethane (DME)	0	83	-58	0.86	0.46	7.2
Dioxolane (DOL)	1	74	-97.2	1.06	0.6	7.1
Tetrahydrofuran (THF)	-14	66	-109	0.88	0.46	7.4
Tetraethylene glycol dimethyl ether (TEGDME)	106	216	-45	0.99	2.73	7.9



maintain performance under varying conditions while offering a safer alternative to liquid electrolytes positions them as a key material in the advancement of LIB technology.

## 2. Degradation pathways pushing cells to catastrophic failure

### a. Cathode materials

**i. Ni-rich layered oxide materials (NCM/NCA).** The instability of the layered crystal structure primarily drives the degradation mechanism for Ni-rich layered oxides. In Ni-rich layered oxides (Ni > 60%), the high proportion of  $\text{Ni}^{4+}$ , combined with the mechanical instability originating from the anisotropic volume changes associated with the  $\text{H}_2 \rightarrow \text{H}_3$  phase transition (Fig. 5a), causes destabilization of the cathode structure and microcrack generation, as discussed by Ryu *et al.*<sup>12</sup> during delithiation, these microcracks weaken the crystalline structure and expose the unstable  $\text{Ni}^{4+}$  to parasitic reactions with the electrolyte, producing an insulating  $\text{NiO}$ -like rock salt phase. As the cathode is charged to high voltages,  $\text{Li}^+$  is extracted, causing  $\text{Ni}^{2+}/\text{Ni}^{3+}$  to oxidize to higher valence states, including  $\text{Ni}^{4+}$ . However,  $\text{Ni}^{4+}$  forms highly covalent, unstable  $\text{Ni}^{4+}-\text{O}^{2-}$  bonds. This instability makes the oxygen more prone to oxidation, especially when the cutoff voltage exceeds  $\sim 4.3$  V. In the process, oxygen is released, making it susceptible to exothermic decomposition.<sup>147-149</sup> These mechanisms interact in complex ways, leading to a cascade of events that culminate in material

degradation, capacity loss, or thermal runaway. In cathodes with low Ni content ( $\leq 80\%$ ), the parasitic side reactions between the cathode and electrolyte are mainly confined to the outer surface of the particles, where microcracks are minimal. In cathodes with Ni content exceeding 80%, the formation of microcracks increases significantly, where degradation from the bulk dominates as the main degradation pathway (Fig. 5b).<sup>150</sup>

Trevisanello *et al.*<sup>154</sup> highlighted this by reporting that the specific surface area of pristine  $\text{LiNi}_{0.8}\text{Co}_{0.1}\text{Mn}_{0.1}\text{O}_2$  cathode increased to  $\sim 1.4 \text{ m}^2 \text{ g}^{-1}$  from  $0.2 \text{ m}^2 \text{ g}^{-1}$  when charged to 4.2 V (vs. Li/Li<sup>+</sup>), owing to microcrack formation. Kang *et al.*<sup>153</sup> reported the capacity retention of a  $\text{Ni}_{0.85}\text{Co}_{0.10}\text{Mn}_{0.05}\text{O}_2$  dropping to 45.1% at 4.4 V after 300 cycles. The degradation is linked to the growth of a phase-transition layer from 10 nm to 25 nm (Fig. 5c), increasing resistance and hindering  $\text{Li}^+$  diffusion. Surface cracks from volume changes and oxygen evolution at high voltages further accelerate performance loss. Noh *et al.*<sup>155</sup> indicated that NCM cathodes with  $\text{Ni} \geq 60\%$  react with air to form  $\text{Li}_2\text{CO}_3$  and  $\text{LiOH}$  on the cathode surface.  $\text{LiOH}$  then reacts with the electrolyte to produce HF acid, leading to electrolyte decomposition and corrosion of electrode materials.  $\text{Li}_2\text{CO}_3$  leads to gas evolution which causes significant swelling of the cathode/battery cell, particularly during high-temperature storage and in the charged state. Furthermore, residual Li compounds increase the cathode surface's alkalinity, degrading the PVDF binder. This degradation forms a gel-like network that obstructs electrode-electrolyte contact,

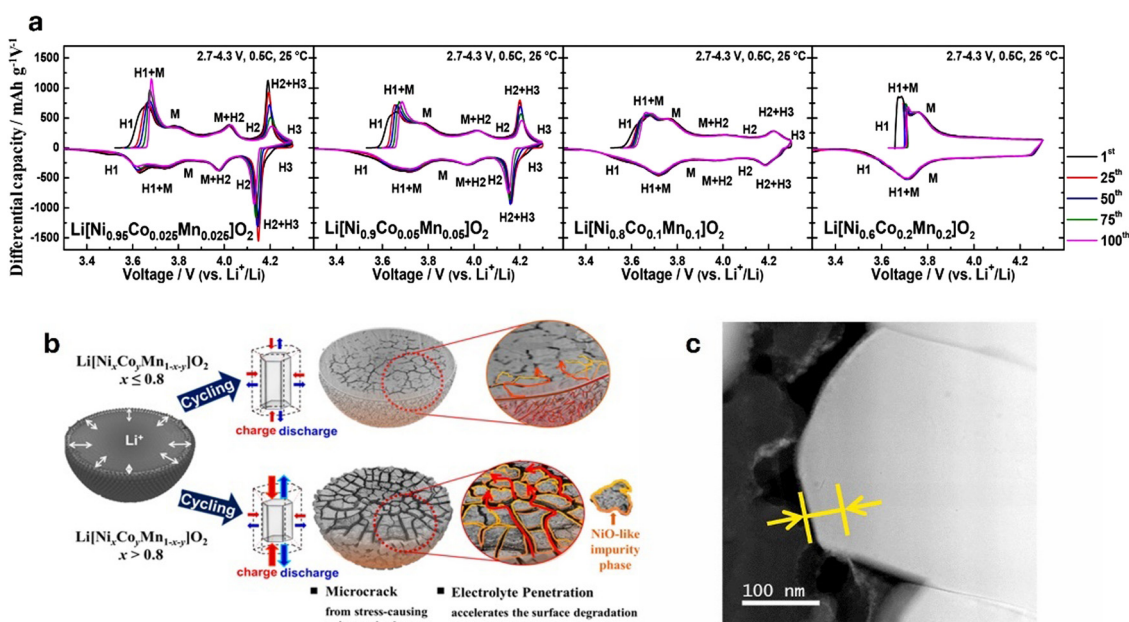


Fig. 5 (a)  $dQ/dV$  profiles of  $\text{Li}[\text{Ni}_x\text{Co}_y\text{Mn}_{1-x-y}]\text{O}_2$  ( $x = 0.95, 0.9, 0.8$ , and  $0.6$ ) illustrating the  $\text{H}_2 \rightarrow \text{H}_3$  phase transition of varying Ni content cathode materials. Reproduced with permission from ref. 151. Copyright 2018, American Chemical Society. (b) Schematic representation of the degradation mechanisms in Ni-rich cathodes. Cathodes with less than 80% Ni primarily degrade due to surface deterioration, whereas those with Ni content exceeding 80% experience degradation through microcrack formation along grain boundaries. These cracks facilitate electrolyte infiltration, leading to the formation of a  $\text{NiO}$ -like rock salt phase. Reproduced under the terms of the Creative Commons CC-BY-NC-ND License.<sup>152</sup> Copyright 2020, American Chemical Society. (c) STEM-EELS image of phase-transition layer. Reproduced with permission from ref. 153. Copyright 2021, Journal of Power Sources published by Elsevier B.V.



impairing ionic conductivity and electron transfer, which reduces cycling capacity, increases internal resistance, elevates charge/discharge rates, and causes overall battery degradation.

Additionally, the similarity in ionic radii between  $\text{Li}^+$  and  $\text{Ni}^{2+}$  facilitates  $\text{Li}^+/\text{Ni}^{2+}$  exchange due to the low potential barrier for  $\text{Ni}^{2+}$  migration to the  $\text{Li}^+$  3b site. During charging,  $\text{Li}^+$  vacancies in the positive electrode are occupied by migrating  $\text{Ni}^{2+}$ , which hinders the return of  $\text{Li}^+$  during discharge. In a highly delithiated state,  $\text{Ni}^{2+}$  continues to migrate to  $\text{Li}^+$  vacancies (octahedral 3b sites), leading to inevitable cation mixing and the release of lattice oxygen due to structural instability, disrupting the local structure and weakening the overall stability of the cathode, thus impacting its performance and lifespan.<sup>156,157</sup> These degradation mechanisms lead to capacity fading, increased impedance, and a reduced cycle life.

**ii. Li-rich layered oxide.** The performance and safety of Li-rich layered oxide are compromised by various intricate degradation mechanisms. A comprehensive understanding of these degradation pathways is crucial for optimizing the performance of Li-rich layered oxide materials. The irreversible loss of lattice oxygen, triggered by the activation of the oxygen redox reaction in Li-rich layered oxides, enables these materials to achieve higher specific capacities. However, this oxygen depletion is both advantageous and detrimental, as significant oxygen loss leads to structural instability and side reactions, ultimately contributing to performance degradation.<sup>158,159</sup> During the first

cycle, Li-rich layered oxides are charged to a high potential where the  $\text{Li}^+$  in the  $\text{LiTMO}_2$  phase are removed. The removed  $\text{Li}^+$  is generally reinserted during the discharge process. However, at higher potentials ( $\sim 4.5$  V), the removal of  $\text{Li}_2\text{O}$  from the  $\text{Li}_2\text{MnO}_3$  phase occurs,<sup>160</sup> contributing significantly to the capacity during the first charge as shown in Fig. 6a with the  $\text{Li}_2\text{MnO}_3$  phase contributing  $152 \text{ mA h g}^{-1}$  to the initial capacity. Unfortunately, this  $\text{Li}$  extraction is mostly irreversible, meaning the  $\text{Li}_2\text{O}$  removed during charging cannot be restored during discharge, leading to a 20–30% capacity loss in the first discharge.<sup>161</sup> Additionally, the generation of oxygen vacancies and the reduction of TM ions weaken the bonds between TMs and oxygen, resulting in easier TM migration to the Li layer sites (Fig. 6b). The migration of TM cations from the TM layer into the Li layer induces significant lattice strain, leading to structural transformations from a layered to a spinel or rock-salt phase (Fig. 6c), which is the main contributor to continuous voltage decay and capacity loss.<sup>59,162</sup>

Li *et al.*<sup>164</sup> reported that TM migration and dissolution caused by oxygen release is the primary cause of degradation with  $\text{Li}_{1.2}\text{Mn}_{0.8}\text{Ni}_{0.2}\text{O}_2$  releasing  $0.31 \mu\text{mol mg}^{-1}$  of oxygen and experiencing a voltage decay of  $2.4 \text{ mV per cycle}$ . Tao *et al.*<sup>165</sup> using *in situ* and *ex situ* X-ray absorption spectroscopy combined with first-principles calculations, revealed that the formation of 27% oxygen vacancies led to a decrease in charge capacity from  $393 \text{ mA h g}^{-1}$  and discharge capacity from

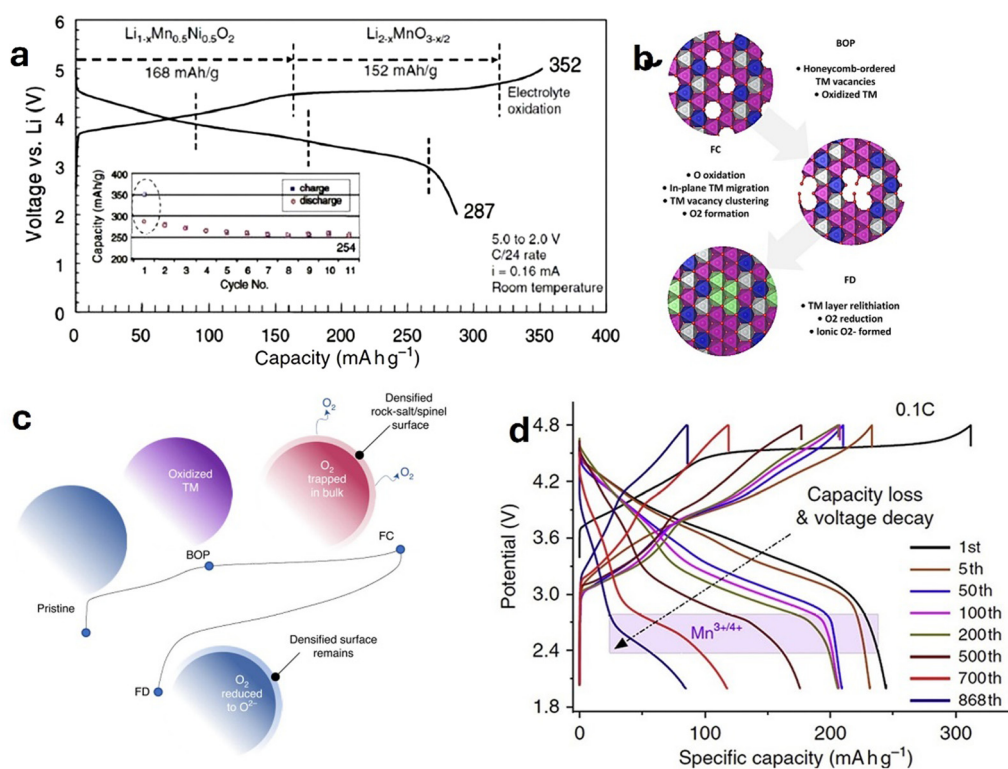


Fig. 6 (a) Voltage curve in the 1st cycle. Reproduced with permission from ref. 52. Copyright 2021, Chinese Society of Particuology and Institute of Process Engineering, (b) atomic-scale changes to ordering within the TM layer. BOP means the beginning of plateau, FC means full charge, FD means full discharge, and (c) macroscale changes to the cathode particles. Reproduced with permission from ref. 163. Copyright 2020, The Authors. (d) Cycling performances. Reproduced with permission from ref. 52. Copyright 2021, Chinese Society of Particuology and Institute of Process Engineering.



Table 4 Key degradation mechanism of cathode materials

Cathode material	Composition	Capacity fade rate	Key degradation mechanisms	Ref.
Ni-rich layered oxide	$\text{LiNi}_{0.6}\text{Co}_{0.2}\text{Mn}_{0.2}\text{O}_2$	0.035%/cycle (100 cycle, 0.5C, 4.3 V, 30 °C)	Minor microcracks; limited surface degradation ( $\sim 5$ nm); no significant $\text{H}_2 \rightarrow \text{H}_3$ transition; stable cycling; damage mostly reversible.	169
	$\text{LiNi}_{0.8}\text{Co}_{0.1}\text{Mn}_{0.1}\text{O}_2$	0.050%/cycle (100 cycles, 0.5C, 4.3 V, 30 °C)	Emerging $\text{H}_2 \rightarrow \text{H}_3$ transition, some microcracks, modest rock-salt surface ( $\sim 7$ –8 nm).	
	$\text{LiNi}_{0.90}\text{Co}_{0.05}\text{Mn}_{0.05}\text{O}_2$	0.150%/cycle (100 cycles, 0.5C, 4.3 V, 30 °C)	Strong $\text{H}_2 \rightarrow \text{H}_3$ , $\Delta c \sim -5.5\%$ , microcracks propagate to surface, electrolyte ingress, interior degradation.	
	$\text{LiNi}_{0.95}\text{Co}_{0.025}\text{Mn}_{0.025}\text{O}_2$	0.170%/cycle (100 cycles, 0.5C, 4.3 V, 30 °C)	Severe $\text{H}_2 \rightarrow \text{H}_3$ , $\Delta c \sim -6.9\%$ , deep cracks, thick rock-salt layer (up to 20 nm), interior failure.	
	$\text{LiNi}_{0.90}\text{Co}_{0.05}\text{Mn}_{0.05}\text{O}_2$	0.150%/cycle (100 cycles, 0.5C, 4.3 V, 30 °C)	Severe microcracking enables electrolyte infiltration, leading to thick rock-salt layers, reduced $\text{Li}^+$ diffusion, increased interfacial resistance, and electrochemical insulation.	16
	$\text{Li}_{1.03}\text{Ni}_{0.85}\text{Co}_{0.10}\text{Mn}_{0.05}\text{O}_2$	0.183%/cycle (300 cycles, 0.2C, 4.4 V, 25 °C)	Surface phase transition layer thickening (10–25 nm); continuous cation mixing; crack formation; Li diffusion resistance rise; spontaneous oxygen release at high voltage	153
Li-rich layered oxide	$\text{Li}_{1.2}\text{Mn}_{0.6}\text{Ni}_{0.2}\text{O}_2$	0.185%/cycle (100 cycles, 4.8 V, 0.2C)	Transition metal migration, oxygen release, layered-to-spinel/rock-salt phase transitions, and structural collapse during cycling due to oxygen vacancy.	170
	$0.5\text{Li}_2\text{MnO}_3 \cdot 0.5\text{LiNi}_{1/3}\text{Co}_{1/3}\text{Mn}_{1/3}\text{O}_2$	0.330%/cycle (100 cycles, 0.1C, 4.5 V 25 °C)	Irreversible oxygen loss ( $\sim 27\%$ vacancies), $\text{MnO}_6$ distortion, phase transformation to $\text{MnO}_2$ , structural disorder, and $\text{TMO}_6$ contraction	165
	$\text{Li}_{1.2}\text{Ni}_{0.2}\text{Mn}_{0.6}\text{O}_2 / \text{Li}_{1.2}\text{Ni}_{0.1}\text{Mn}_{0.525}\text{Co}_{0.175}\text{O}_2$	0.172%/cycle (100 cycles, 0.33C, 4.6 V, 30 °C)	Oxygen loss; TM migration into Li layer; layered-to-spinel transformation; amorphization; strain; crack and pore formation; mosaic spinel domains	166
5 V spinel	$\text{LiNi}_{0.5}\text{Mn}_{1.5}\text{O}_4$	0.50%/cycle (100 cycles, 30C, 4.8 V, 0.1C)	Active $\text{Li}^+$ loss; Mn dissolution; SEI formation on graphite; electrolyte oxidation at high voltage; $\text{Li}^+$ trapping	168

294 mA h g<sup>-1</sup> at 0.1C, to 194 mA h g<sup>-1</sup> after 100 cycles. The release of lattice oxygen induces structural changes,<sup>166</sup> raises internal cell pressure, and catalyzes the oxidative decomposition of the electrolyte. This process forms a thick, resistive cathode-electrolyte interphase (CEI), hindering  $\text{Li}^+$  transport and contributing to the low initial Coulombic efficiency in Li-rich layered oxides. Hence, the growth of the spinel phase and surface defect spinel layer are deemed as the primary factors contributing to poor electrochemical performance. These degradations result in voltage fading in Li-rich cathode materials (Fig. 6d), typically when the integrity and order of the layered structure cannot be fully maintained during cycling at high cutoff voltages.

**iii. 5 V Spinel.** The primary challenge in utilizing the potential of 5 V spinel cathodes resides in their high operating voltage. Conventional LIB electrolytes, which typically comprise salt solutions of Li in organic solvents such as carbonate esters (EC, PC, DMC, DEC, EMC, DFEC) are limited by an electrochemical stability window that falls below 4.5 V. Unfortunately, 5 V spinel cathodes operate at voltages exceeding this limit. As a result, these electrolytes readily undergo oxidation and decomposition when paired with LMO or LNMO, leading to several detrimental effects.<sup>167,168</sup> The decomposition products form a thick solid layer on the electrode surfaces, hindering  $\text{Li}^+$  transport and ultimately reducing cell capacity, and generate gaseous byproducts such as  $\text{CO}_2$ , CO,  $\text{POF}_3$ ,  $\text{C}_2\text{H}_5\text{OCOOPF}_4$ , and  $\text{OPF}_2\text{ORF}$ .<sup>167</sup> These gaseous byproducts further contribute to the capacity fading of the 5 V spinel cell by triggering transition

metal dissolution and migration to the anode. This has been widely acknowledged as a major failure mechanism of 5 V spinel cathodes.<sup>168</sup>

The key degradation mechanism discussed for Ni-rich layered oxides, Li-rich layered materials, and 5 V spinel cathodes are summarized in Table 4 to highlight their distinct failure modes.

## b. Anode materials

**i. Silicon.** The degradation of silicon is driven by both mechanical and chemical factors. Mechanical degradation is primarily attributed to the significant volume expansion and contraction during Li alloying/dealloying because the intermetallic compounds of Li-Si have considerably higher molar volumes than the original nanostructured Si phases.<sup>171</sup> As a result, the repetitive volume changes induce large stresses that cause cracking and pulverization of Si anodes. In addition to particle pulverization, the large volume changes disrupt the electrode architecture. As silicon anodes undergo expansion and contraction during each charging cycle, the bonds between the active material, binder, and conductive additives become weakened. This ultimately leads to the delamination of the active material from the current collector (Fig. 7a), resulting in a loss of electrical conductivity and a decline in capacity.<sup>88</sup> During dealloying, Si undergoes surface roughening and a gradual formation of a nanoporous structure that drives electrolyte decomposition and continuous SEI growth on freshly exposed Si surfaces, causing depletion of the limited  $\text{Li}^+$  and



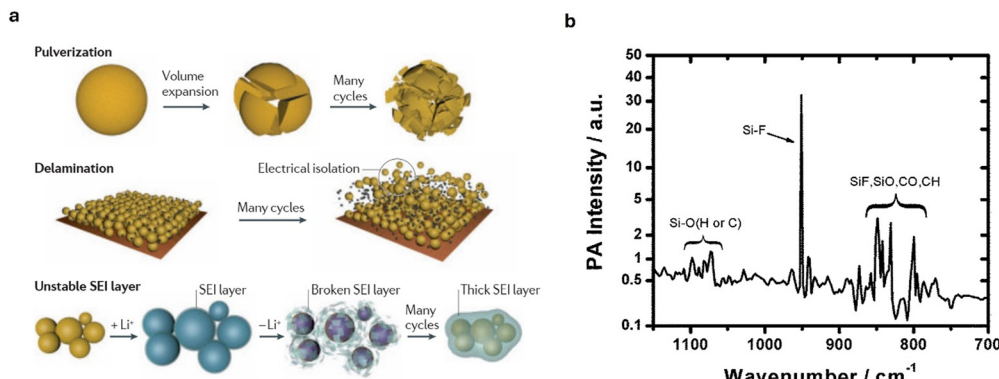


Fig. 7 (a) The main degradation mechanisms of Si anode. Reproduced from ref. 174. Copyright 2016, Macmillan Publishers Limited. (b) Photoacoustic infrared spectroscopy of the interfacial layer formed on Si-anode surface from unwanted reaction with LiPF<sub>6</sub>-based carbonate electrolyte. Reproduced with permission from ref. 173. Copyright 2014, The Royal Society of Chemistry.

electrolyte supply.<sup>172</sup> Moreover, bare Si electrodes exhibit a high irreversible capacity loss on the first cycle, indicating that large amounts of Li<sup>+</sup> are either trapped in the Si matrix or consumed.<sup>88</sup> To address this, agglomerated nanosized Si particles, ~10 nm in size, are commonly used. However, this method increases the surface area to be covered by an SEI, triggering more electrolyte consumption and eventual capacity fade.<sup>173</sup> This continuous SEI growth and Li/electrolyte depletion are described as the primary failure mechanisms in Si anodes.<sup>172</sup>

Furthermore, during dealloying, Si undergoes considerable volume shrinkage, causing regions of the Si that became amorphous during lithiation (due to the structural disruption from Li insertion) to recrystallize into small crystalline grains called nanograins. These nanograins introduce grain boundaries that are prone to mechanical failure.<sup>26</sup> In a LiPF<sub>6</sub> electrolyte, the amorphous silicon surface also rapidly reacts with the electrolyte to form a 35 Å interface layer<sup>173</sup> that consumes electrochemically active Si. Veith *et al.*<sup>173</sup> estimated that this 35 Å interface formation leads to a 17% consumption of electrochemically active Si, effectively lowering the capacity of the Si anode.

Recent studies have highlighted the critical role of chemical degradation as well. For instance, Kim *et al.*<sup>26</sup> highlighted that even before cycling, reactions between Si and the electrolyte result in the corrosion of Si anodes, causing dissolution of Si ions. These dissolved Si ions, along with pulverized Si fragments, block the pores of the separator to impede Li<sup>+</sup> diffusion and charge transfer. Furthermore, in LiPF<sub>6</sub>-based carbonate electrolytes, non-electrochemically driven Si-O and Si-F bonds form on the surface of the Si anodes (Fig. 7b), consuming active Si.<sup>26</sup> The Si-O groups react with HF generated during the decomposition of LiPF<sub>6</sub> causing further dissolution of Si and the formation of water molecules that trigger further HF generation and continuous Si corrosion.<sup>26,173</sup> The generation of HF coupled with rising cell temperature resulting from increasing cell impedance, creates conducive environments capable of triggering and sustaining thermal runaway events.

Over-lithiation, which can occur during battery operations through overcharging, introduces additional complications.

Wang *et al.*<sup>175</sup> demonstrated that over-lithiation promotes Li plating on Si surfaces, to compete with the alloying process. The resulting localized Li plating forms dendrites that puncture the separator and cause internal short circuits. Additionally, over-lithiation accelerates the formation of crystalline Li<sub>15</sub>Si<sub>4</sub>, which exacerbates voltage hysteresis.

**ii. Conversion anode.** Conversion-type anodes undergo several degradation mechanisms, including large volume changes caused by phase transitions, continuous electrolyte decomposition, low electronic conductivity, and severe voltage hysteresis.<sup>25</sup> Voltage hysteresis is a major contributor to the failure mode of conversion anodes. It arises from the different overpotentials required for the nucleation and growth of new phases, the energy required to drive mass transport, and the interfacial energy penalties affiliated with forming and maintaining nanophases during the lithiation/delithiation steps.<sup>130</sup> The extent of this polarization is considerably influenced by the nature of the metal-anion covalent bonds, with materials like metal fluorides, oxides, and sulfides exhibiting the highest polarizations due to their slower kinetics and lower ion mobilities.<sup>130</sup> In metal fluorides, for instance, the voltage discrepancy is also heavily influenced by the size of the metal nanoparticles formed during the reaction. As demonstrated by Seo *et al.*,<sup>176</sup> when CuF<sub>2</sub> undergoes conversion, it breaks down into nanosized metallic Cu and LiF, which have high surface-to-volume ratios and high surface energies that result in an energy penalty, which in turn reduces the voltage observed during discharge. The smaller the nanoparticles, the greater the surface energy, and the larger the voltage discrepancy.

During cycling, these anode materials also undergo significant structural reorganization, resulting in substantial expansions and contractions. The large volume changes create mechanical stress, leading to fracturing, cracking, and eventual electronic isolation of active material particles.<sup>130</sup> As with other types of anode materials, the mechanical cracks from the repeated structural reorganization expose fresh surfaces, driving excessive SEI growth. For instance, metal fluoride (MF) particles in liquid electrolyte become coated with up to 20 nm thick SEI layer from metal (M) catalysis.<sup>177</sup> However, due to



morphological changes and separation of LiF and M clusters, this formed SEI becomes too brittle to accommodate the volume change in the active material,<sup>177</sup> causing exposure of fresh surfaces to the electrolyte, followed by the irreversible loss of Li and the leaching of  $M^{1+/2+/3+}$  cations and  $F^-$  anions.<sup>177</sup> At elevated temperatures, the degradation phenomenon intensifies.

The conversion reaction mechanism transforms the active material into metallic nanoparticles dispersed in a Li compound matrix. The key to stable cycling of conversion anodes relies significantly on the formation of metallic nanoparticles with high interfacial surface area and high activity towards decomposition upon lithiation.<sup>130</sup> Typically, nanostructured active materials offer benefits, such as a larger electrode-electrolyte contact area, shorter  $Li^{+}$  diffusion paths, and improved reactivity. However, nanoparticles are susceptible to agglomeration, which lead to a loss of the initial nanostructure and reduction in the reversible conversion reaction efficiency. The uneven stress distribution that could result from the agglomerated nanometallic particles leads to mechanical fractures that further contribute to the disconnection of the active materials from the current collector. This issue is particularly pronounced when the size of the nanoparticles is  $\sim 10$  nm, reducing the likelihood of re-engaging in the conversion process during subsequent cycles.<sup>176</sup>

The kinetics of the conversion reaction also contribute to degradation. Conversion reactions are typically slower than intercalation processes, owing to the multi-electron transfer mechanism involved in the reduction and oxidation of the metal compounds. The kinetics of conversion reactions are also influenced by a host of other factors, including diffusion coefficients of cations and anions, electronic and ionic conductivity of the newly formed phases, interfacial energetics,<sup>178</sup> the crystal structure of the host lattice, and the diffusion length of metals during cation exchange.<sup>179</sup> McDowell *et al.*<sup>179</sup>

demonstrated this using different metal sulfides. They noted that copper atoms in  $Cu_2S$  for instance move more freely because they have longer diffusion lengths, leading to a faster conversion reaction. However, in  $FeS_2$ , iron atoms cannot move as easily because their diffusion lengths are much shorter, especially at room temperature. This makes it harder for the conversion reaction to proceed easily in  $FeS_2$ . This sluggish kinetics leads to poor rate performance, particularly under fast charging and discharging conditions. The dissolution of transition metals in liquid electrolytes, polysulfide dissolution, and incomplete reconversion reactions also contribute to the degradation of conversion-type anodes.<sup>180-182</sup>

**iii. Graphite.** The degradation of graphite anode is attributed to structural disordering, dissolved transition metal cations plating, and Li plating/dendritic growth (Fig. 8).<sup>20-22</sup> During Li intercalation/deintercalation, graphite undergoes surface structural disordering that generates steep Li concentration gradients, particularly during the early stages of lithiation.<sup>183</sup> This induces local stresses at the edges of graphene sheets that result in the breakage of C-C bonds and the formation of disordered graphite structures. This surface disordering is exacerbated by the continual expansion and contraction of the graphite layers during repeated  $Li^{+}$  intercalation/deintercalation cycles. The expansion and contraction cause electrode strain that results in swelling or cracking.<sup>184</sup> As noted by Sethuraman *et al.*,<sup>183</sup> during  $Li^{+}$  intercalation, the graphite interlayer spacing increases from 3.359 Å in pristine graphite to 3.712 Å in lithiated  $LiC_6$ , inducing mechanical stress and further structural breakdown of graphite. Although this expansion is relatively mild in comparison to other anode materials like silicon, it contributes to localized deformations, delamination of graphite from the current collector, and gradual loss of the structural integrity of graphite during long-term cycling. Another significant degradation mechanism is the instability of SEIs formed on graphite. Repeated cycling, especially under

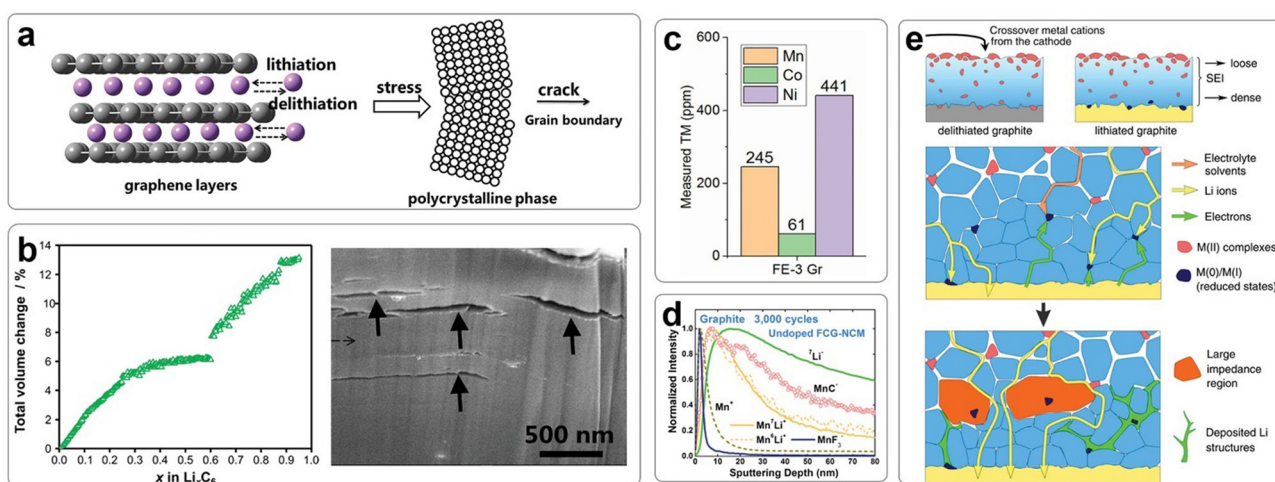


Fig. 8 (a) Crack formation of graphite particles induced by cycling, (b) volume change of a graphite electrode as a function of Li content during lithiation and SEM image of cracks, (c) TM content obtained in a graphite anode after 120 cycles, (d) TOF-SIMS depth profiles of graphite anode after 3000 cycles, and (e) schematic representation of the SEI film evolution at a graphite electrode during cycling under the influence of chemical crossover from the cathode. Reproduced with permission from ref. 15. Copyright 2021, The Authors. Advanced Energy Materials published by Wiley-VCH GmbH.

high charge/discharge rates, causes a continuous breakdown and reformation of the SEI—a process that consumes both Li and electrolyte inventory in the cell. Moreover, the continuous disintegration/reformation of the SEI leads to the growth of a thicker, heterogeneous SEI that consequently increases the internal impedance of the battery cell, further contributing to capacity fade, reduced cell efficiency, and elevated cell temperature.<sup>19</sup>

A more serious degradation of graphite results from the precipitation of dissolved transition metal cations ( $\text{Ni}^{2+}$ ,  $\text{Mn}^{2+}$ , and  $\text{Co}^{2+}$ ) from the cathode onto the graphite surface. The deposited transition metal components cover significant portions of graphite, impeding  $\text{Li}^+$  intercalation and increasing local current density, which accelerates Li deposition.<sup>20</sup>

These cations catalyze parasitic reactions within the SEI, promoting further thickening, structural instability, and the formation of non-uniform SEI layers.<sup>21</sup>  $\text{Mn}^{2+}$  particularly triggers the formation of a thick SEI that reduces cell impedance and ionic conductivity.<sup>21</sup> The catalytic effects of  $\text{Ni}^{2+}$  and  $\text{Co}^{2+}$  also increase interfacial resistance, further hindering mobility and charge transfer across the anode.<sup>21</sup>

Under current conditions greater than 1C, graphite has slow  $\text{Li}^+$  intercalation kinetics. Hence,  $\text{Li}^+$  intercalation into graphite layers becomes less efficient, causing  $\text{Li}^+$  not inserted into the graphite layer to be deposited on the graphite surface as metallic Li.<sup>185</sup> The thermodynamic window for Li intercalation into graphite ranges from approximately 1–100 mV *versus* Li/Li<sup>+</sup>, slightly above the potential at which Li plating occurs (below 0 V *versus* Li/Li<sup>+</sup>). Under normal conditions, Li intercalation occurs without significant issues. However, during fast charging, high reduction overpotentials are required to drive rapid lithiation of graphite. This can lower the anode potential below 0 V, making Li plating thermodynamically favorable.<sup>186,187</sup> This process is further driven by ohmic and concentration polarization.<sup>186</sup> This process contributes to the depletion of the Li inventory, increases the cell's internal resistance, and, more critically, leads to the formation of needle-like dendrites. These dendrites puncture the separator, causing internal circuits that create a favorable condition for thermal runaway.<sup>185</sup> This is considered a severe safety-related degradation pathway because once dendrite formation commences, it becomes a dominant failure mechanism as these structures can rapidly grow and trigger catastrophic cell failure.

**iv. Metallic Li.** Li metal anode degradation is primarily driven by dendrite formation, where uneven Li deposition during charging results in the formation of needle-like dendrites as shown in Fig. 9. Repeated Li plating and stripping (deposition/dissolution) processes produce numerous Li dendrites on the anode surface, resulting in lower Coulombic efficiency.<sup>188</sup> As these dendrites continue to grow, they pierce the separator leading to internal short circuits. Moreover, rapid, uneven dissolution of the Li dendrites near active sites detaches these structures from the electrode, yielding “dead Li”.<sup>189</sup> This “dead Li” refers to electrically isolated Li metal that is encased in a thick SEI layer made up of inorganic and organic Li species. Once disconnected, these Li needles and particles lose their electron and ion transport pathways. Consequently, the formation of “dead Li” reduces the amount of active Li in the electrode and decreases the battery's specific capacity.<sup>190,191</sup> Several works have been done to understand the formation of Li dendrite in metallic Li anodes. In 2016, Wood *et al.*,<sup>190</sup> using operando video microscopy, showed that dendrites formed due to surface inhomogeneities that lead to localized hotspots where Li nucleates. This creates subsurface disturbances that fracture the SEI and expose the underlying Li metal, causing dendrite formation at the fracture points. Han *et al.*,<sup>192</sup> using mass transport monitoring, revealed that the dendrite formation is heavily influenced by the uneven mass transport of  $\text{Li}^+$ . Li dendrite typically emerges when the  $\text{Li}^+$  concentration depletes near the Li metal electrode, leading to non-uniform Li deposition. This transition from a smooth to a dendritic morphology is further accelerated by the uncontrolled reactions on the Li surface to create spatial heterogeneities in the SEI layer that promote dendrite nucleation. The growth of these dendrites exposes fresh Li metal to the electrolyte, further accelerating the creation of new SEI layers and additional dendrites, that cascade to potential battery failure.<sup>193–196</sup>

Thermal instability also plays a crucial role in the degradation of Li metal anodes. During cycling, heat generation from internal resistance and side reactions exacerbate dendrite growth, SEI breakdown, and side reactions, leading to accelerated degradation and potential safety risks. Furthermore, these issues are strongly interdependent, presenting more significant challenges.<sup>193</sup>

**v. Fast charging anode.** Fast-charging anodes, such as lithium titanate (LTO) and Wadsley–Roth anode, experience

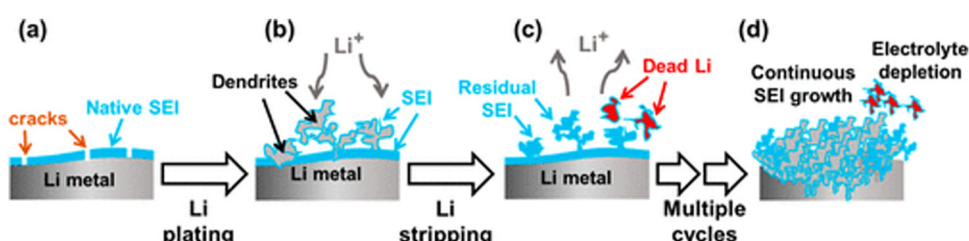


**Fig. 9** Schematic diagram showing (from left to right) (a) pristine Li metal with heterogeneous native SEI layer, (b) growth of Li dendrites during Li plating, (c) loss of  $\text{Li}^+$  (“dead Li”) and growth of residual SEI during Li stripping, and (d) continuous SEI growth and electrolyte depletion after multiple plating/stripping cycles. Reproduced under the terms of the ACS AuthorChoice License.<sup>130</sup> Copyright 2020, American Chemical Society.



complex degradation mechanisms driven by the high current densities associated with rapid charge cycles. LTO anodes are known to have unsatisfactory  $\text{Li}^+$  coefficient ( $10^{-11} \text{ cm}^2 \text{ s}^{-1}$ ) and electron conductivity ( $10^{-13} \text{ S cm}^{-1}$ ), which deteriorate their rate capability, thereby limiting their application.<sup>197,198</sup> Banks *et al.*<sup>199</sup> investigated the degradation mechanisms in LTO batteries, focusing on the impact of elevated temperatures and the SOC. They identified surface layer formation and gas generation as the primary degradation factors, which are both influenced by the SOC. At higher temperatures, particularly at 80 °C, they observed an increase in gas production (including  $\text{H}_2$ ,  $\text{CO}$ , and  $\text{CO}_2$ ), which led to cell swelling and rupturing in some cases, posing significant safety concerns. The study found that degradation is most severe at high SOCs, where irreversible damage occurs due to the loss of active material (LAM) at the positive electrode and the depletion of Li inventory. Liu *et al.*<sup>200</sup> reported that the primary cause of degradation in LTO-based batteries is attributed to LAM, where at least 83% of the total capacity loss at 10C and 81% at 5C cycling conditions originates from LAM. The degradation mechanisms were closely linked to the depth of discharge and cycling rate, with deeper discharge cycles and slower cycling rates accelerating capacity loss.

Wadsley–Roth based structures featuring  $\text{ReO}_3$ -like structure have emerged as an alternative anode for LTO replacement. These anode materials are based on niobium oxide structures namely  $\text{TiNb}_2\text{O}_7$ ,  $\text{Ti}_2\text{Nb}_{10}\text{O}_{29}$ ,  $\text{W}_8\text{Nb}_{18}\text{O}_{69}$ ,<sup>201</sup>  $\text{W}_3\text{Nb}_{14}\text{O}_{44}$ ,<sup>202</sup>  $\text{W}_4\text{Nb}_{26}\text{O}_7$ ,<sup>203</sup>  $\text{Ti}_2\text{Nb}_{10}\text{O}_{29}$ ,<sup>204</sup>  $\text{GaNb}_{11}\text{O}_{29}$ ,  $\text{Nb}_{18}\text{W}_8\text{O}_{69}$ ,<sup>205</sup>  $\text{Mg}_2\text{Nb}_{34}\text{O}_{87}$ ,<sup>206</sup> and  $\text{MoNb}_{12}\text{O}_{33}$ .<sup>207</sup> These niobium-based Wadsley–Roth phases with the sheared octahedra stabilize the structure during intercalation by locking the  $\text{ReO}_3$ -like, edge-sharing  $\text{NbO}_6$  octahedral blocks in-place. Thus, these shear structures do not undergo phase changing and allow  $\text{Li}^+$  diffusion back and forth freely.<sup>208</sup> While the unique crystallographic shear structure of the Wadsley–Roth anode provides advantages for  $\text{Li}^+$  transport, it also presents certain challenges that hinder its performance. One significant drawback is its relatively long  $\text{Li}^+$  diffusion path, leading to slower lithiation/delithiation kinetics. Moreover, the Wadsley–Roth phase anodes suffer from poor electronic conductivity, which is reported to be as low as  $3 \times 10^{-6} \text{ S cm}^{-1}$ . This low conductivity increases the overall resistance in the electrode, causing large polarization during battery operation.<sup>209,210</sup> An additional degradation mechanism for the Wadsley–Roth anode is the generation of gas. The absence of SEI film on the anode surface allows for electrolyte degradation at the anode–electrolyte interface, leading to the release of harmful gases.<sup>211,212</sup> Buannic *et al.*<sup>213</sup> investigated the degradation of  $\text{TiNb}_2\text{O}_7$  and  $\text{Ti}_2\text{Nb}_{10}\text{O}_{29}$  and found a clear correlation between the anode's surface area and the amount of gas produced. Specifically,  $\text{TiNb}_2\text{O}_7$ , with a surface area of  $32 \text{ m}^2 \text{ g}^{-1}$ , generated significantly more gas than  $\text{TiNb}_2\text{O}_7$  with  $6 \text{ m}^2 \text{ g}^{-1}$ . The gassing is primarily attributed to water electrolysis, with trace water present in the electrolyte or adsorbed on electrode surfaces that results in hydrogen gas production, which constitutes up to 80% of the total gas. Further reactions between  $\text{Ti}^{4+}$  and carbonate solvents in the electrolyte form  $\text{CO}$ ,  $\text{CO}_2$ ,

and hydrocarbons ( $\text{C}_1\text{--C}_3$ ). These processes contribute to electrolyte degradation, producing approximately 800  $\mu\text{L}$  of gas after 30 days of cycling in  $\text{TiNb}_2\text{O}_7$ /LMNO pouch cells.

### c. Electrolytes

i. **Carbonate electrolytes.** Liao *et al.*<sup>29</sup> identified two primary degradation pathways for carbonate–electrolytes: decomposition at the electrode–electrolyte interfaces and bulk electrolyte breakdown. At the anode, the continuous insertion and extraction of  $\text{Li}^+$  cause expansion and contraction of the electrode, leading to mechanical stress that fractures the SEI. These fractures necessitate SEI repair, which continuously consumes more electrolytes and increases internal resistance, especially in anode materials like silicon that undergo significant volume changes.<sup>29,214</sup> Similarly, at the cathode, the cathode electrolyte interphase (CEI) is often non-uniform and unstable, particularly in Ni-rich materials, where anisotropic volume changes create microcracks.<sup>29</sup> These cracks expose fresh surfaces to the electrolyte, leading to further CEI formation/repair and additional electrolyte depletion. Moreover, at high voltages ( $>4.6 \text{ V}$ ), electrolyte decomposition is driven by oxidative processes, often linked to oxygen evolution from the transition metal oxide lattice.

At elevated temperatures, carbonate electrolytes undergo decomposition reactions that generate heat and toxic gaseous products. The thermal instability of carbonate-based electrolytes is exacerbated when reactive Li salts, such as  $\text{LiPF}_6$ , are dissolved in these solvents. For instance, ethyl methyl carbonate (EMC) is stable on its own but shows significant gas production when catalyzed by  $\text{LiPF}_6$ .<sup>28</sup> The decomposition pathway of  $\text{LiPF}_6$  is significantly autocatalytic, and it results in the formation of  $\text{HF}$ ,  $\text{PF}_5$ ,  $\text{CO}_2$ , and other corrosive species capable of accelerating further decomposition of the electrolyte and dissolution of transition metals in the cathode (Fig. 10a–d).<sup>28</sup> The  $\text{PF}_5$  species generated from the salt decomposition reacts with trace water molecules in the electrolyte to form  $\text{HF}$  (Fig. 10b).<sup>215</sup>  $\text{HF}$  presence in the system leads to other degradation processes, such as corrosion of the electrodes and current collectors, etching of the separators, and destruction of SEI layer (Fig. 10e).<sup>215</sup> The strong Lewis acid nature of  $\text{PF}_5$  further triggers decomposition of carbonate electrolytes.<sup>216</sup> The reaction between  $\text{PF}_5$  and the carbonate solvents is exothermic, and the increased heat and accumulation of gases can increase the internal pressure of the cell (Fig. 10d), increasing the risk of thermal runaway. The relative reactivity of the carbonate solvents with  $\text{LiPF}_6$  at elevated temperatures follow the order EC > DEC > EMC > DMC.<sup>28</sup>

A seeming solution to mitigate the thermal instability of carbonate electrolytes would be to use alternative, less reactive salts. However, studies have shown that, the solvents themselves are problematic—for instance, Lamb *et al.*<sup>28</sup> showed that EC and DEC were found to produce the most toxic gas during thermal decomposition, with each generating upwards of 1.5 moles of gas per mole of electrolyte without the presence of  $\text{LiPF}_6$ .



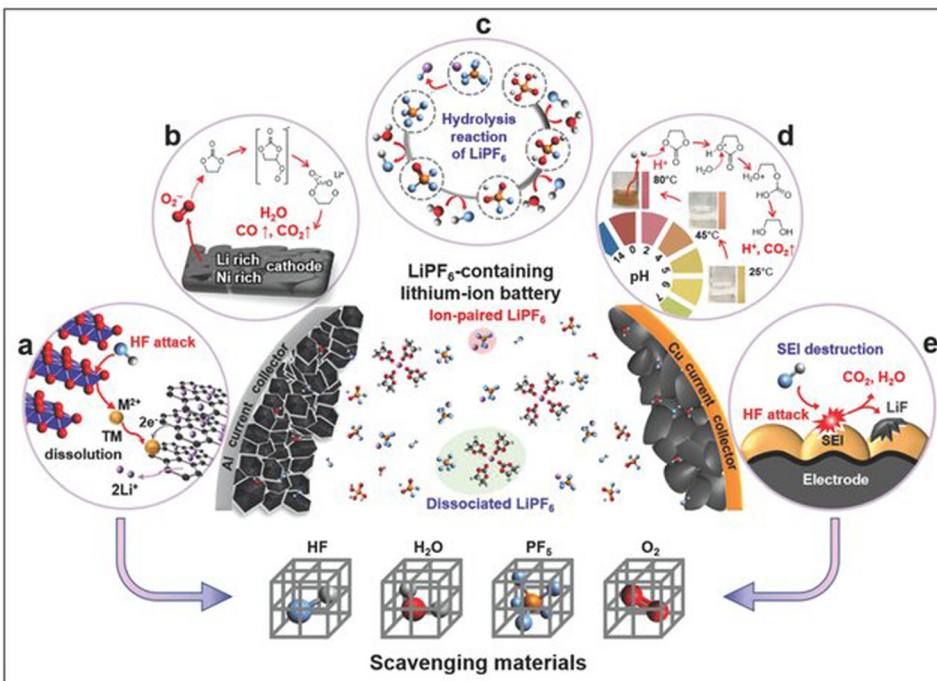


**Fig. 10** Schematic representation of the key challenges of  $\text{LiPF}_6$ -containing carbonate electrolytes. Reproduced with permission from ref. 217. Copyright Wiley-VCH: (a) transition metal dissolution resulting from HF attack, (b) gas evolution triggered by solvent decomposition, (c) hydrolysis reaction of  $\text{LiPF}_6$  to form HF and corrosive acids, (d) thermal decomposition of  $\text{LiPF}_6$ , (e) interfacial layer destruction by HF attack.

Efforts have been made to research the use of alternative Li salts with better thermal stability, conductivity, and less toxicity. To this end, LiTFSI and LiFSI have garnered considerable interest owing to their extremely high thermal stability (*i.e.*, no degradation until  $\sim 360$   $^{\circ}\text{C}$ ).<sup>128</sup> Eshetu *et al.*<sup>218</sup> conducted a detailed investigation of the thermal behavior of  $\text{LiPF}_6$  vs. LiFSI-based carbonate electrolytes. They observed that the LiFSI-based electrolytes produced fewer harmful byproducts, with significantly reduced HF output. However, LiFSI-based electrolytes still emit toxic gases such as  $\text{SO}_2$ ,  $\text{NO}$ , and  $\text{HCN}$ . Additionally, the calorimetry experiments demonstrated that the LiFSI-based electrolytes have shorter combustion durations, albeit more explosive than the  $\text{LiPF}_6$ -based electrolytes. Sångeland *et al.*<sup>219</sup> investigated the decomposition of a LiTFSI-based carbonate electrolyte (1 M LiTFSI in EC:DEC 3:7 w/w) and

noted ethylene and hydrogen (in negligible quantity) as the dominant volatile organic species formed. Moreover, the application of LiTFSI is hindered by its corrosive reaction with Al foil, which is typically used as the cathodic current collector.<sup>128</sup> Therefore, the tradeoffs in the cost and electrolyte properties must be carefully considered when switching from  $\text{LiPF}_6$  to LiTFSI/LiFSI or other Li salts. Owing to this conundrum, subsequent sections will discuss extensively modern strategies being applied to improve the thermal stability of carbonate electrolytes.

**ii. Ether electrolytes.** Ether-based electrolytes are prone to oxidative degradation and thermal decomposition, especially at elevated temperatures and high voltages, where they undergo auto-oxidation, forming peroxides and other by-products (Fig. 11b).<sup>220</sup> According to Tommaso *et al.*,<sup>221</sup> the high

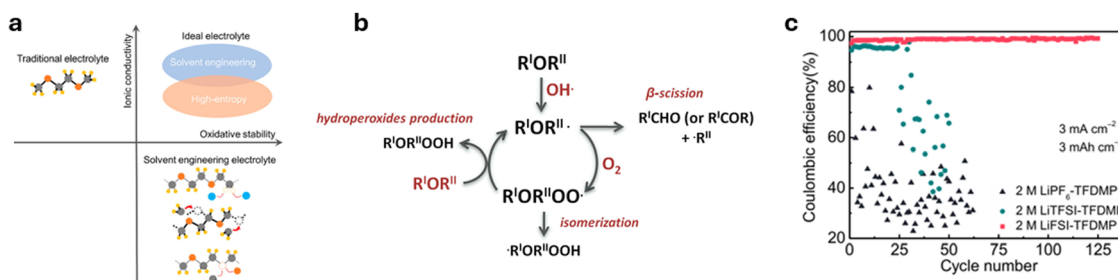


**Fig. 11** (a) Schematic of the requirements for ether electrolytes for high-voltage LIBs. Reproduced under the terms of the Creative Commons CC-BY 4.0 License.<sup>222</sup> Copyright 2024, The Authors. Published by American Chemical Society, and (b) scheme of the autoxidation mechanism of aliphatic ether solvents. Reproduced with permission from ref. 221. Copyright 2012, American Chemical Society. (c) CE test of  $\text{Li}||\text{Cu}$  cells cycled in an ether solvent (1,1,1-trifluoro-2,3-dimethoxypropane (TFDMP)) containing different salts. Reproduced under the terms of the Creative Commons CC BY license.<sup>223</sup> Copyright 2023, The Authors.



susceptibility of ethers to oxidation is primarily attributed to their chemical structure, characterized by the presence of an oxygen atom between two alkyl or aryl groups. Through an auto-oxidation process initiated by a hydroxyl radical, the oxygen in the ether structure abstracts hydrogen from an adjacent carbon atom, forming an alkyl radical under atmospheric conditions.<sup>221</sup> The process typically follows a radical chain mechanism, where the formed radicals propagate the oxidation reaction, which is severely exacerbated at elevated temperatures, leading to a cascade of flammable oxidative degradation products.<sup>221</sup>

As with carbonate electrolytes, the type of Li salt also impacts the thermal/oxidative degradation of ether electrolytes, LiPF<sub>6</sub> impedes the performance of ether electrolytes (Fig. 11c). In contrast, LiTFSI or LiFSI can significantly improve the electrochemical performance of Li-metal anodes cycled in ether electrolytes.<sup>222</sup> The easily reducible S-F bonds in the anions of LiTFSI and LiFSI salts form electron-insulating compounds such as LiF more readily than those in LiPF<sub>6</sub> salt, resulting in the formation of a more stable SEI, translating to better electrochemical performance.<sup>222</sup>

The concentration of salt in ether-based electrolytes is also paramount. The oxidative stability of ether-based electrolytes at typical Li salt concentrations of  $\sim 1$  M is considerably low. This is because, with fewer Li<sup>+</sup> available, ether molecules cannot form stable complexes that mitigate oxidation.<sup>224</sup> In contrast, carbonate electrolytes have oxygen atoms with lone-pair electrons that can form more stable complexes.<sup>224</sup> Consequently, the oxygen atoms in the ethers are more prone to losing electrons, making the electrolyte more susceptible to oxidation and eventual decomposition. The degradation of ether electrolytes is also influenced by the chain length of the ether, where shorter chain ethers tend to be more thermally unstable compared to longer-chain counterparts.<sup>225</sup>

**iii. Gel polymer electrolytes.** Gel polymer electrolytes (GPEs), which combine the mechanical stability of solid electrolytes with the ionic conductivity of liquid electrolytes, offer improved safety but still face thermal stability concerns, especially at high temperatures. GPEs typically consist of a liquid plasticizer in a polymer–salt system. The plasticizer components generally determine the electrochemical properties of GPEs, whereas the polymer matrix defines the safety, mechanical properties, and morphology of GPEs.<sup>141–143</sup> To date, two main classes of plasticizers are commonly used—low molecular weight organic solvents and ionic liquids, of which the organic solvents are the most reported.<sup>138,139</sup> When low organic solvents are used, large quantities are typically required as the low molecular weight organic solvents suffer from significant solvent loss over time. At elevated temperatures, this compromises the mechanical properties and stability of GPEs,<sup>138</sup> causing them to inherit some adverse thermal behaviors observed in conventional liquid electrolyte systems.

Moreover, a low glass transition temperature ( $T_g$ ), high decomposition temperature, and high melting temperature of the polymer matrix form important criteria for selecting a polymeric host, as these significantly affect the thermal

behavior of GPEs.<sup>142</sup> A low  $T_g$ , whilst it enhances the ionic conductivity, can reduce the overall mechanical stability of the electrolyte, leading to an increased risk of thermal decomposition. Below  $T_g$ , the polymer exists in a glassy state, and above  $T_g$ , the polymer becomes rubbery and more flexible,<sup>136</sup> bringing the material closer to melting and decomposition at elevated temperatures. Melting and decomposition of the polymer are typically distinct thermal events, but the thermal energy required for melting can bring the polymer material closer to a state of decomposition, potentially initiating the chemical breakdown of both plasticizer and polymer materials.

The chemical structure of the polymeric host also affects the thermal degradation behavior of GPEs. The varying application cases of LIBs necessitate an electrolyte that is thermally stable over a wide temperature range, making PVDF- and PAN-based GPEs more favored due to their superior thermal stability. This stability is attributed to the strong C–F bonds in PVDF<sup>142</sup> and the formation of a stable, cross-linked structure in PAN upon heating.<sup>143</sup> Conversely, GPEs based on polymers such as polyethylene glycol diacrylate (PEGDA) are PEO (and their derivates) are highly flammable.<sup>226</sup> Owing to this, fire retardants, such as organic phosphates like trimethyl phosphate (TMP), triethyl phosphate (TEP), and dimethyl methylphosphosphate (DMMP), have been employed to address the flammability issue.<sup>226,227</sup>

GPEs offer considerable advantages over carbonate- and ether-based electrolytes. However, their thermal instability still poses a major challenge that must be addressed to ensure safe and reliable applications. Hence, strategies to improve and enhance the safety of GPEs will be comprehensively discussed in Section 4.

### 3. Cell and pack level studies on understanding and mitigating thermal runaway risk

#### a. Battery abuse testing methods and mechanisms

Batteries are subjected to a wide variety of stresses when operating in various applications, including mechanical vibrations and impact, high electrical load, and extreme thermal environment. These stresses can result in accelerated degradation, gas generation, excessive swelling, internal short circuits, overheating, and gas venting, leading to thermal runaway. To fully understand and mitigate the effects of thermal runaway, abuse testing and simulations are typically performed on battery cells. In this section widely employed mechanical, electrical, and thermal abuse testing methods are discussed.

**i. Nail penetration.** Nail penetration is the most common form of mechanical abuse test to understand the failure point and safety characteristics of a battery cell.<sup>228</sup> In this type of abuse test, a nail is inserted into the battery cell with a mechanical force sufficient to penetrate through the cell casing, resulting in direct contact of the cathode and anode. This causes the battery cell to rapidly discharge and raise internal cell temperature, triggering catastrophic failure, including fire and explosion.<sup>229</sup> For instance, Finegan *et al.*<sup>229</sup> designed



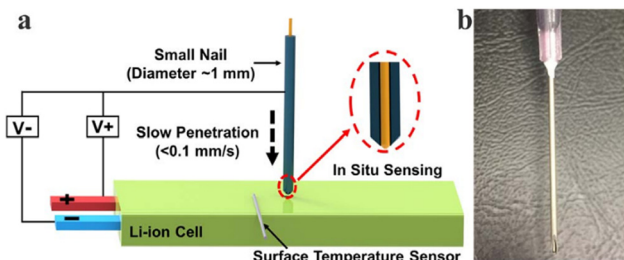


Fig. 12 (a) Schematic of the small, slow, and *in situ* sensing (3S) nail penetration test. (b) Photograph of the small, *in situ* sensing nail. Reproduced under the terms of the Creative Commons CC BY license.<sup>230</sup> Copyright 2020, The Author(s).

custom 314 stainless steel nails with an integrated insulated K-type thermocouple of 0.5 mm diameter and imaged penetrated 18 650 cells, providing comprehensive data on the thermal and structural dynamics. The variability of nail penetration position was found to directly affect the temperature rise and the failure mechanism of the cells.<sup>229</sup> Another study developed a new method for nail penetration analysis using small, slow, and *in situ* sensing, referred to as 3S.<sup>230</sup> In the study, a small nail (diameter  $\sim 1$  mm) embedded with a micro temperature sensor at the tip was used for the nail penetration test on a 3 A h pouch cell at penetration speeds of  $<0.1$  mm s $^{-1}$  (Fig. 12). The study observed that the *in situ* sensed nail tip temperature reached a maximum of over 800 °C while the surface temperature only reached about 400 °C during thermal runaway. Specifically, *in situ* monitoring helped observe three temperature peaks before its onset which could not be detected from surface temperature indicating that the *in situ* sensing can reveal critical early-stage indicators of the thermal runaway phenomena, such as intense local hot spots and precursory thermal spikes. These temperature peaks were due to the contact between the nail tip and the current collector as a result of nail piercing through the battery in a controlled manner. This contact created a low resistance internal short circuit that induced high internal short circuit current and rapid heat generation, ultimately leading to a sudden temperature rise. A rapid decrease in the temperature was also noted following each peak. This was attributed to the rupturing of the Al foil that led to the increase in contact resistance, decreasing the local current and heat generation at the site of penetration.<sup>230</sup>

This method separates internal short-circuit processes from thermal runaway. Yang *et al.*<sup>231</sup> studied the evolution in voltage, temperature, and vent gas of 8 types of cylindrical batteries using LFP cathode chemistry. It was observed that the onset was triggered by the shrinkage of the separator and the reactions between the cathode and electrolyte. It was also found that the runaway reactions were more intense when penetration was performed near the cell ends, but the nail speed had virtually no effect on the thermal and electrochemical behavior of the cell.

Chiu *et al.*<sup>232</sup> simulated the electrochemical-thermal behavior of a punctured 5.25 A h cell. The model predicted a rapid increase in current density due to an internal short circuit at

the site of nail penetration. However, as the active material was depleted, the current density predicted by the model declined. Zhao *et al.*<sup>233</sup> introduced an area-specific contact resistance to model Joule heating at the location of penetration. Their coupled electrochemical-thermal model successfully predicted the rapid temperature rise during nail penetration with current and voltage responses, and deformation of the battery. The model prediction was verified using experimental results.

**ii. Overcharge.** Overcharge-induced thermal runaway is characterized by localized internal short circuits and the rapid generation of heat and gases.<sup>234</sup> Wang *et al.*<sup>235</sup> studied the thermal runaway characteristics of 25 A h prismatic LFP/Gr cells with different states of health (SOH) (100%, 80%, 70%, and 60%) under different charge rates (2C, 1C, 0.5C, 0.3C) and noted that overcharging behavior has four stages. In the first stage, the ohmic and reversible heat were the primary contributors to the total heat generated. The second and third stages had side reactions, such as SEI decomposition and anode-solvent reaction, as the primary sources of heat. The fourth stage included heat generation due to electrolyte decomposition, cathode decomposition, binder decomposition, and internal short circuits. Zhang *et al.*<sup>236</sup> investigated the effects of slight overcharge. The main findings indicated that although slight overcharge (*i.e.*, 105% to 120% SOC) has minimal influence on the overall cell capacity, it leads to thermal instability, causing cells with different degrees of overcharge to exhibit similar behavior during adiabatic thermal runaway events. Zhou *et al.*<sup>237</sup> subjected cells to an overcharge test at various C rates (0.5C, 1C, and 2C) while applying a 10 kg preload and found that higher C rates during the overcharge test increased the risks of thermal runaway. They also found that larger preloads resulted in relatively lower crest voltages during the overcharge test but more severe reactions. Hence, the onset temperature and heat generation tend to be higher at higher preloads. Wang *et al.*<sup>238</sup> compared the differences in the thermal behavior of LIBs with three different cathode materials NCM, LFP, and LCO tested under different overcharge rates (0.5C, 1C, and 3C). The LCO batteries had the highest risk of thermal runaway, followed by NCM and LFP. The rate of overcharge (*i.e.*, C rate during overcharge tests) also had a significant impact on the thermal risk for all the cathode chemistries, and the time till runaway was significantly smaller for higher C rates. For NCM and LCO, there was a reduction in the time by 10 793 s and 5332 s, respectively, as the rate increased from 0.5C to 3C. For the LFP batteries, the time decreased by 1812 s when the rate was increased from 1C to 3C.

Huang *et al.*<sup>239</sup> experimentally investigated the internal failure mechanisms and associated external characteristics during overcharging in prismatic and pouch cells using Li[Ni<sub>0.33</sub>Co<sub>0.33</sub>Mn<sub>0.33</sub>]O<sub>2</sub>/Gr pouch and prismatic cells. The cells were charged from 0% SOC to the set end point at 1C current. During stage I (safe overcharge stage), both pouch and prismatic cells maintained low temperatures, but the pouch cells exhibited better overcharge tolerance. As overcharging progressed, the prismatic cell experienced a slower rise in temperature and deformation due to its safety valve. The maximum



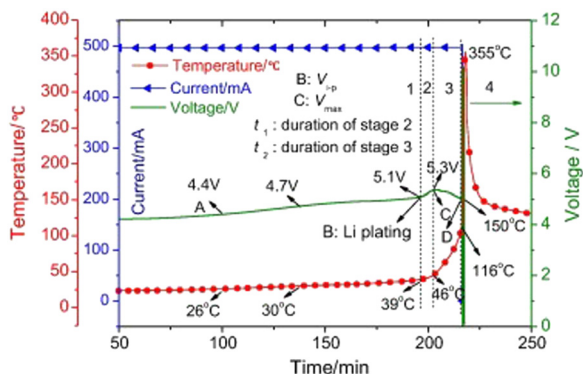


Fig. 13 Stages of overcharge induced thermal runaway based on overcharging experiments combined with ARC. Reproduced with permission from ref. 240. Copyright 2016, Elsevier Ltd.

surface temperature difference increased linearly during the test, with hotspots forming at one end of both cells, offering insights for improved design for effective heat dissipation. Ye *et al.*<sup>240</sup> investigated the dynamic thermal behaviors of commercial  $\text{LiCoO}_2 + \text{Li}(\text{Ni}_{0.5}\text{Co}_{0.2}\text{Mn}_{0.3})\text{O}_2/\text{C} + \text{SiO}_x$  cells during overcharge under adiabatic conditions by combining a multi-channel battery cycler with an accelerated rate calorimeter (ARC).

The study found that the overcharge process in LIBs follows four distinct stages, as shown in Fig. 13. (1) A to B: as the cathode delithiated and the anode lithiated, the voltage increased gradually, with low surface temperature and minimal gas evolution until decomposition accelerated above 4.5 V. (2) B to C: as the cathode approached full charge, heat generation increased due to electrolyte decomposition, producing  $\text{CH}_4$  and alkyl radicals, while gas release caused cell deformation, leading to Li plating on the edges of the graphite anode due to a change in the distance between the anode and cathode. (3) C to D: the surface temperature increased sharply above 60 °C, triggering exothermic reactions between the delithiated cathode and electrolyte, causing  $\text{CO}_2$  gas evolution, voltage drop, and structural degradation of the cathode. (4) D to terminal: when the internal temperature reached 150–160 °C, the separator shut down, leading to violent reactions involving Li, electrolyte, binder, and cathode material. This triggered thermal runaway, rupture, and gas emissions ( $\text{CO}_2$ , CO,  $\text{H}_2$ ,  $\text{CH}_4$ ,  $\text{C}_2\text{H}_6$ ,  $\text{C}_2\text{H}_4$ ). At higher C rates ( $>1.0\text{C}$ ), overpotential heat accelerated temperature rise, making electrolyte–cathode reactions more intense before Stage B.

Zhu *et al.*<sup>241</sup> systematically studied the overcharge-induced thermal runaway properties of 30 A h cells using NCM622 cathode at different C rates at 30 °C. It was found that the overcharge process consisted of four stages. Stage I entailed normal charging with stable voltage and temperature, while Stage II marked the beginning of the overcharge conditions, causing a gradual voltage increase and slight temperature increase. In Stage III, voltage plateaus and temperature increased rapidly, signaling an increased risk that escalates in Stage IV, where extreme temperature spikes led to battery rupture, fire, or explosion, accompanied by a sharp voltage

drop. Qi *et al.*<sup>242</sup> developed an overcharge model of the LIB pack by coupling the electrochemical model with the thermal abuse model. The study used a battery pack of three fully charged batteries with a capacity of 10 A h, with only the middle one overcharged. It was found that higher overcharge currents increased the thermal runaway onset temperature of the overcharged middle cell but lowered it in the adjacent non-overcharged cells. Cell spacing and clamping significantly influenced heat transfer, increasing the risk of failure in neighboring cells. The overcharged middle cell heated rapidly, transferring heat to adjacent cells.

Using both experimental and numerical methods, Mei *et al.*<sup>243</sup> demonstrated that overcharging of a commercial 26650  $\text{LiNi}_{1/3}\text{Co}_{1/3}\text{Mn}_{1/3}/\text{Gr}$  cell caused Li plating. The overcharge tests performed to induce Li plating included constant current charging at 0.2C and 0.5C to the cut-off voltage range of 4.5–4.9 V with no relaxation to stabilize the Li content within the electrode bulk. They found that Li plating begins at voltages  $>4.5$  V, with greater Li deposition occurring at higher voltages as confirmed by SEM images showing dendritic Li growth at the anode–separator interface. Furthermore, using computational simulations, they revealed that overcharge led to deeper Li penetration, increasing plating severity. The model showed a linear relationship between Li plating and C rates, indicating that higher C-rates accelerate plating, emphasizing the need for controlled charging. Increasing anode thickness while maintaining a reasonable N/P ratio (*i.e.*, 1.1–1.2) was found to reduce Li plating risk by lowering local current density and increasing Li accommodation in the electrode structure.

**iii. Internal short circuit.** Liu *et al.*<sup>244</sup> used electrochemical impedance spectroscopy to analyze the resistance of internal short circuits (ISC) with concurrent monitoring of thermal runaway propagation using high-speed X-ray imaging. The results highlighted that the expansion of the failure area is linked to the melting and collapse of the separator. Wu *et al.*<sup>245</sup> used infra-red imaging thermography to characterize the evolution process from ISC to thermal degradation inside a LIB. The ISC was triggered by heating the battery to approximately 70–75 °C. The study identified a thermal runaway boundary, where a hot spot of  $50\text{ mm}^2$  exceeding 150 °C, combined with rapid exothermic side reactions within 0.6 seconds, triggered a thermal occurrence. Batteries with high energy and low resistance ISC are more prone to runaway, while those with low energy or high resistance ISC develop temporary hot spots that cool down. Exothermic side reactions dominated the hot spot region, releasing significant heat, while the exhaust leaving the cell, which consisted of flammable gases (after  $\sim 1.5$  seconds), caused pressure buildup. The study also highlighted that temperature gradients near the ISC point influenced the severity of exothermic reactions.

Liu *et al.*<sup>246</sup> developed a 3D equivalent circuit model of a 20 A h LIB and performed ISC simulations. The study considered the effects of ISC area, resistance, penetration depth, convective heat transfer coefficient, and ISC position on thermal runaway. The results of the study demonstrated that the average cell temperature is only weakly affected by the ISC area,



penetration depth, and position. On the other hand, the ISC resistance and the convective heat transfer coefficient have large impacts on the thermal runaway propagation. A high convective heat transfer coefficient can effectively suppress this propagation. However, such a high convective heat transfer coefficient is hard to achieve at the cell surface. Finegan *et al.*<sup>247</sup> used an ISC device placed in multiple locations across the cell for controlled, on-demand, initiation of thermal runaway to study the nucleation and propagation failure within 18 650 cells through the use of high-speed X ray imaging at 2000 frames per second. It was observed that sidewall rupture was more likely when the runaway event was initiated closer to the casing of the cell. Likewise, the cylindrical mandrel in the core of the electrode assembly was shown to influence the venting process.

Huang *et al.*<sup>248</sup> reported *in situ* measurement of temperature distributions in a 2.5 A h pouch format cell during ISC and thermal runaway events. The events were triggered by nail penetration. It was observed that the *in situ* sensed nail tip temperature started to increase after 30 s and exhibited multiple peaks corresponding to the cell voltage drops. The multiple temperature peaks and voltage drops suggested that there were multiple short-circuit processes during the nail penetration process. The highest temperature of the nail tip at the internal short circuit location was measured to be 209 °C. Liu *et al.*<sup>249</sup> compared the performance of five substitute triggering methods for ISC; use of phase change materials (PCM), shape memory alloys (SMA), artificially induced dendrite growth, equivalent resistance, and nail penetration. Likewise, the thermal-electrical coupled features, controllability, similarity to real accidents, and repeatability of the test were discussed by experimental and modeling analysis. It was found that there were four different classes of ISC. The first class was the most dangerous, where the voltage rapidly drops to 0 V and has a maximum temperature rising rate of nearly 100 °C s<sup>-1</sup>. This class of ISC would be accompanied by severe thermal runaway when conducted by nail penetration or triggering Al-An type ISC by PCM and SMA. The second and third class featured less abrupt voltage failure and slow voltage drop, respectively, and both these classes demonstrated lower temperature rise of only 10 °C s<sup>-1</sup> with no thermal runaway. The fourth class showed minimal impact in both voltage drop and temperature rise.

Xu *et al.*<sup>250</sup> employed an electrochemical-thermal model, validated through experiments, to analyze how electrode design parameters influence ISCs in cylindrical LIBs. A parametric study examined the effect of parameters such as porosity, electrode/separator thickness, short-circuit area, and failure layers, revealing their effects on internal resistance, voltage drop, and temperature rise. Additionally, the study categorized different short-circuit types (An-Ca, An-Al, Ca-Cu, and Al-Cu) to enhance understanding of failure mechanisms and provide insights for safer battery designs. The study validated a coupled electrochemical-thermal model by comparing simulation results with experimental data, effectively describing electrochemical behavior during normal and short-circuit conditions. Using a 2200 mA h LCO cell, experiments, including nail penetration tests, showed that voltage remained stable until

4 mm penetration, after which temperature and voltage changed significantly. Thermal runaway occurred 300 seconds after short-circuit initiation, though model predictions deviated from measured temperatures at this stage. The study found that cathode design had a more substantial impact on internal resistance and battery safety than the anode, emphasizing the importance of optimizing cathode electrode architecture. These insights provide crucial guidance for safer LIBs designs, focusing on separator integrity, porosity, and thickness to mitigate short-circuit risks.

**iv. External short circuit.** An *et al.*<sup>251</sup> employed a variety of experimental methods to investigate the thermal behavior and mechanism during external short circuiting. Constant current discharge process at various discharge rates (30C, 25C and 20C) were simulated while also conducting experiments on small capacity batteries under external short circuit (ESC) conditions (Fig. 14). The study found that the capacity of the short-circuited batteries was recovered despite initial damage. Furthermore, in batteries with high states of charge (80% and 100%), the maximum temperature was related to the time of battery rupture. Li deposition, electrolyte evaporation, graphite particle rupture, and separator closure were observed during the discharge process of the high SOC batteries. This increased internal resistance and caused internal side reactions. The ohmic resistance experienced a permanent increase while the polarization resistance recovered to the condition prior to the ESC experiments.

Zeng *et al.*<sup>252</sup> investigated the ESC characteristics of 18 650-type NCM LIBs under different SOCs and short-circuit currents. The study involved ultra-high discharge rates (*i.e.*, 15C, 18C, 20C, 22C, 25C) for constant current discharge at 50% and 100% initial SOCs to simulate the ESC condition. The results of the study found that short circuits induced a serious risk of deleterious thermal events when the discharge rate reached 25C and the maximum temperature exceeded 500 °C. At low SOC levels, there was rapid depletion of Li<sup>+</sup>, increasing the polarization resistance and exhibiting a sharp voltage drop in

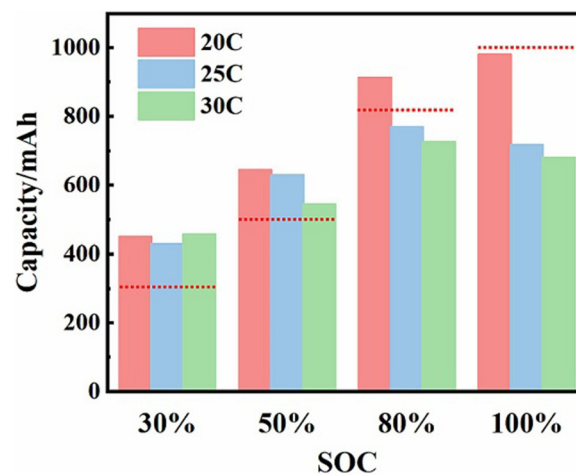


Fig. 14 Discharge capacity at different C rates. Reproduced with permission from ref. 251. Copyright 2022, Elsevier Ltd.



this instance. The high temperature during the short circuit induced a closure of the separator pores.

An *et al.*<sup>253</sup> further studied the effect of SOC and discharge rate on the ESC behavior of a 3 A h LFP graphite pouch battery. The battery damage was triggered by ESC abuse for 50% and 100% initial SOCs at discharge rates of 20C, 30C, 40C, and 50C. The results of the study indicated that maximum temperature points during ESC were always found halfway between the anode and cathode tabs for all discharge rates. Electrolyte depletion and thermal adhesion of the cathode to the electrode and wrinkling of the electrode were observed due to gas generation from heat-driven side reactions. In another study,<sup>254</sup> an analytical model to predict runaway events in prismatic and pouch cells due to ESC/ultra-high discharge rates was developed. COMSOL Multiphysics was used for validation of the analytical model, and it was found that at discharge rates above 15C, multiple decomposition reactions occur, ultimately leading to thermal runaway. The ambient temperature was also found to have a critical role, as cells discharged below 30 °C remain stable, while those at 40 °C or higher experienced a higher runaway risk due to reduced convective heat dissipation, causing excessive temperature rise. At a 15C discharge rate, only SEI decomposition occurs, generating insufficient heat to trigger further reactions. However, at a higher discharge rate of 18C, additional reactions, including negative electrode and solvent decomposition, occur, generating enough heat to initiate a chain reaction. This escalation leads to a rapid rise in temperature.

### b. Characterizing thermal stability of battery materials and cells using calorimetry

Various calorimetric tests are used to understand the behavior of LIBs during thermal abuse conditions. In these tests, batteries are typically heated in adiabatic conditions, and temperature, pressure, and their rate of increase are measured.<sup>255</sup> Differential scale calorimetry (DSC) is employed to look at the thermal stability and exothermic reactions of chemical components in a battery at the material level.<sup>255</sup> ARC is designed to study exothermic chemical reactions by simulating adiabatic conditions. By employing ARC, critical kinetic parameters, *i.e.*, the onset temperature of the reaction and the enthalpy of the exothermic process, can be acquired.<sup>256</sup>

Liu *et al.*<sup>257</sup> performed an ARC test on an aged 1.2 A h pouch cell with 95%  $\text{LiMn}_2\text{O}_4$  + 5%  $\text{Li}(\text{Ni}_{0.5}\text{Mn}_{0.2}\text{Co}_{0.3})\text{O}_2$  cathode and graphite anode to obtain the onset temperature of the SEI decomposition reaction. Ren *et al.*<sup>258</sup> investigated the thermal runaway mechanisms using DSC for a fully charged 24 A h  $\text{Li}(\text{Ni}_{1/3}\text{Co}_{1/3}\text{Mn}_{1/3})\text{O}_2$ /graphite battery. The cell components extracted from the pouch cell were tested individually and as mixtures to elucidate the mechanism and characterize exothermic reactions. Six exothermic reactions were characterized, and kinetic analysis was performed on them based on the DSC data. It was found that the heat generation was dominated by the reactions on the anode/electrolyte interface, such as the decomposition of SEI film and the reaction between anode active material and electrolyte. The data from the ARC test was

used to validate the model prediction once all the kinetic parameters were estimated using this data. Patel *et al.*<sup>259</sup> used ARC test to study the failure mechanism of commercially available 18650 cells with  $\text{Li}(\text{Ni}_{0.6}\text{Mn}_{0.2}\text{Co}_{0.2})\text{O}_2$  cathode, polymer separator, and graphite anode. The study revealed the initial exothermic event occurred between 30–50 °C and is attributed to the breakdown and reformation of the SEI layer while the second exothermic event indicating the onset of thermal runaway occurred at 175 °C. The study also quantifies the reaction rates associated with thermal failure.

Kvasha *et al.*<sup>260</sup> studied the thermal runaway of three different Li-ion cells (NCA/graphite, LFP/graphite, NCA/LTO) at 100%, 50%, and 9% SOC and conducted DSC and ARC tests to study the behavior of positive and negative electrodes at the three SOC levels. All cells underwent thermal runaway, regardless of SOC or chemistry, with higher SOC leading to lower onset temperatures and faster self-heating rates. Despite using a low-stability polyolefin separator, LFP/graphite was the most thermally stable due to its polyanionic structure, unlike the unstable NCA, which releases oxygen when heated. DSC tests confirmed that all electrodes were thermally unstable in LP30 electrolyte.

In a study by Feng *et al.*,<sup>261</sup> the DSC tests showed significantly lower heat generation in NCM cells compared to ARC, suggesting that anode reactions were not the primary heat source during thermal runaway. Instead, the process was mainly driven by redox reactions between the cathode and anode, with the cathode undergoing active material decomposition, cathode–electrolyte reactions, and electrolyte breakdown, while the anode experienced SEI layer decomposition and Li–electrolyte interactions. The ARC tests identified three key temperatures:  $T_1$  (70–150 °C) for SEI decomposition,  $T_2$  (<300 °C) as the thermal stability threshold, and  $T_3$ , which varied with energy density and determined spread rate. These findings highlight that thermal runaway is primarily dictated by cathode-driven exothermic reactions and battery design factors rather than internal short circuits. Yuan *et al.*<sup>262</sup> conducted experiments with different Li-ion cells in sealed canisters of steel and used DSC to analyze small samples of anodes, cathodes, and separators while ARC was used to heat battery cells. Cells were charged and discharged three times and were charged again to 100% SOC for testing, and each test was repeated twice to ensure reliability and repeatability. Three different cathode chemistries were selected for the study, namely NCM, LFP, and LTO. For the NCM cell, it was found from the DSC tests that anodes and cathodes exhibited sharp exothermic peaks at lower temperatures (159–174 °C for anodes, 125–200 °C for cathodes), which indicated lower stability as compared to LFP and LTO batteries. Likewise, ARC tests showed that NCM cells had a slower temperature rise before experiencing the highest peak temperature (998 °C), while LTO had the lowest peak temperature of 305 °C but had faster thermal runaway (Fig. 15). It was observed that NCM cells emitted flames while LFP cells only released smoke, indicating different behaviors at thermal failure among different chemistries.



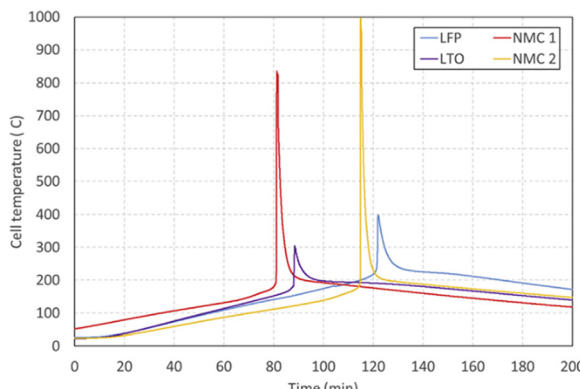


Fig. 15 Comparison of surface temperatures during ARC tests. Reproduced with permission from ref. 262. Copyright 2020, Elsevier B.V.

Fractional Thermal Runaway Calorimetry (FTRC) is also used to measure thermal runaway behavior by characterizing energy release during thermal events. FTRC measures the total heat release and fractionates it into heat emitted through the casing and heat expelled as ejecta, providing a detailed energy distribution analysis. Unlike DSC, which analyzes small material samples for heat flow and reaction enthalpies, and ARC, which evaluates whole cells under adiabatic conditions to measure self-heating rates, FTRC uniquely quantifies how heat propagates externally, making it essential for studying thermal management and containment strategies in real-world applications. Walker *et al.*<sup>263</sup> employed FTRC for GS Yuasa Li-ion cells and found the average total energy release to be 1.6 times the stored electrochemical energy, supporting the notion that energy yield scales linearly with the capacity of the cell.

### c. Cell gas build up and venting

During thermal runaway, LIBs generate flammable and toxic gases, leading to internal pressure build-up and eventual venting to prevent catastrophic failure. Several studies have investigated the composition and behavior of vented gases using techniques like gas chromatography and Fourier transform infrared spectrometry to identify key species, such as hydrogen, carbon monoxide, methane, and ethylene. These studies provide crucial insights into gas generation mechanisms, venting thresholds, and the impact of factors like SOC and cell chemistry. Understanding these processes is essential for improving battery safety, fire mitigation strategies, and thermal management systems and as such there have been numerous studies on quantifying and understanding the gas venting process during thermal runaway in batteries. Yuan *et al.*<sup>262</sup> conducted gas chromatography to study the vented gas and found that major gas concentrations of vented gases were primarily dependent on the battery chemistry used. The study used three different chemistries, namely NCM, LFP, and LTO, and found that the NCM cells produced the highest levels of CO and CH<sub>4</sub> but the lowest levels of C<sub>2</sub>H<sub>4</sub> while LFP cells produced the highest levels of H<sub>2</sub>, C<sub>2</sub>H<sub>2</sub>, C<sub>2</sub>H<sub>4</sub>, and C<sub>2</sub>H<sub>6</sub> but lowest levels of CO. On the other hand, LTO cells produced the highest levels of

CO<sub>2</sub> and lowest levels of H<sub>2</sub>, CH<sub>4</sub>, C<sub>2</sub>H<sub>2</sub>. Jiaqiang *et al.*<sup>264</sup> used gas chromatography to review models of gas generation, highlighting its role in increasing internal battery pressure. Their study found that flammable and toxic gases, including CO<sub>2</sub>, H<sub>2</sub>, CH<sub>4</sub>, and C<sub>2</sub>H<sub>6</sub>, were released, with their composition varying based on cathode materials and operating conditions. They also outlined the importance of understanding these mechanisms as crucial for assessing hazards. Using a H<sub>2</sub> detector and Fourier transform infrared spectroscopy in their study, Jia *et al.*<sup>265</sup> also found similar composition but reported differences in total gas production depending on whether thermal runaway is caused by overcharging or overheating. The overheating scenario involved larger gas production (101.3 L) suggesting a high reaction rate as compared to overcharging, which produced a gas volume of 62.1 L only. This study also identified that overcharging promotes gas release, leading to earlier venting mechanism activation by triggering the safety venting mechanism. Despite overcharging producing a lower volume of gas, it led to faster thermal runaway onset than overheating by initiating earlier gas generation that resulted in weakening of the structural integrity of the cell and triggering an internal short circuit. On the other hand, during overheating, the battery underwent progressive degradation that required a higher temperature threshold before thermal runaway was initiated, but it was more intense when it occurred. Ostanek *et al.*<sup>266</sup> developed and validated a gas generation model that computes gas generation from decomposition reactions and electrolyte vaporization. Their results indicated that modification of cell design and geometry could influence the evaporation rate, which in turn affected the vent time and time to thermal runaway. Kim *et al.*<sup>267</sup> developed a numerical model to study cell venting, internal pressure, and gas-phase dynamics behavior of 18 650 Li-ion cells. It was found that the production of flammable gases like CO, H<sub>2</sub>, and hydrocarbons led to higher internal pressure with an increase in SOC. Mao *et al.*<sup>268</sup> found a simplified relation suggesting that the gas generation rate is proportional to the temperature increase rate. They also found the peak pressure at 100% SOC to be significantly higher than at 0% SOC.

## 4. Approaches to enhancing safety

### a. Cathode

Several strategies have been proposed to address the degradation mechanisms of the LIB cathode materials. These strategies include modifying the microstructure using techniques, such as concentration gradient design and nanorod synthesis, and applying protective coatings.

#### i. Microstructure modification

*a. Concentration gradient cathodes.* Concentration gradient cathodes are engineered to enhance performance, safety, and longevity by incorporating a deliberate variation in chemical composition from the core to the shell of the cathode material. Three main configurations have been developed based on this gradient concept: core-shell gradient (CSG), full-concentration



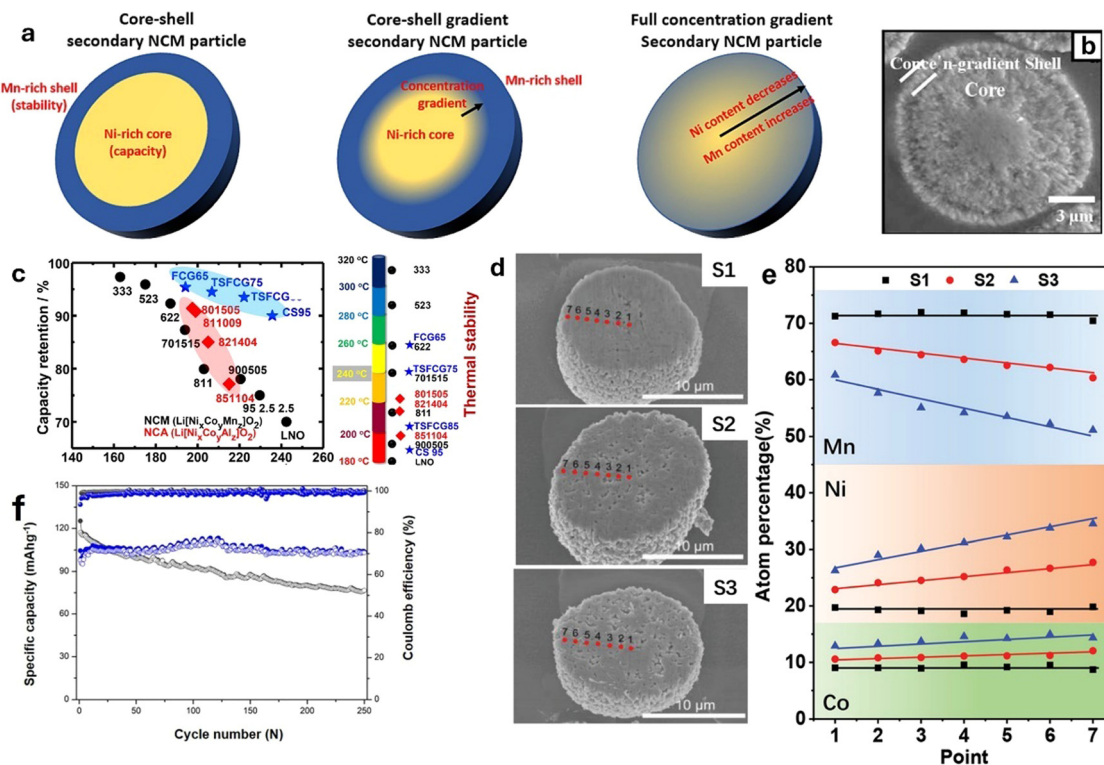


**Fig. 16** (a) Illustration of core–shell, core–shell concentration gradient, and full concentration gradient NCM particle structures. Reproduced with permission from ref. 274. Copyright 2023, Elsevier Ltd. (b) SEM images of the lithiated core–shell oxide with concentration-gradient shell particles. Reproduced with permission from ref. 273. Copyright 2010, Wiley–VCH Verlag GmbH & Co. KGaA, Weinheim. (c) Capacity retention, thermal stability versus specific capacity of gradient cathodes compared to constant concentration cathodes. Reproduced with permission from ref. 275. Copyright 2017, American Chemical Society (d) cross-sectional SEM images of the three Li-rich layered oxides (S1, S2, and S3) with different gradients and (e) gradients of representative S1, S2, and S3 semispheres as reflected by the contents of transition metals at positions 1–7 (see Fig. d) from the sphere center to the surface. Reproduced with permission from ref. 276. Copyright 2020, Wiley–VCH GmbH. (f) The comparison of cycling stability for the raw  $\text{LiMnO}_4$  and obtained  $\text{g-Li}_{1+x}\text{Mn}_{2-x}\text{O}_4$ . Reproduced with permission from ref. 277. Copyright 2022, Elsevier B.V.

gradient (FCG), and two-sloped full-concentration gradient (TSFCG) cathodes.<sup>269–271</sup> This approach provides significantly enhanced cycling stability and thermal resilience, especially under strenuous high voltage cycling conditions. For Ni-rich layered oxide, these materials feature a high concentration of Ni at the core of the cathode and a Mn-rich concentration at the shell to serve as a protective layer that reduces the reactivity at the cathode's surface (Fig. 16a).<sup>41,272,273</sup> Sun *et al.*<sup>273</sup> first introduced the concept of a concentration-gradient cathode in 2010 with the development of  $\text{Li}[\text{Ni}_{0.72}\text{Co}_{0.18}\text{Mn}_{0.10}]\text{O}_2$ , a Ni-rich layered oxide designed to enhance both electrochemical and thermal stability. This cathode featured a Ni-rich core ( $\text{Li}[\text{Ni}_{0.8}\text{Co}_{0.2}]\text{O}_2$ ) surrounded by a Mn-rich shell ( $\text{Li}[\text{Ni}_{0.55}\text{Co}_{0.15}\text{Mn}_{0.30}]\text{O}_2$ ) (Fig. 16b), creating a gradual compositional transition that mitigated structural degradation and improved cycling performance. The cathode delivered an initial discharge capacity of 193 mA h g<sup>−1</sup> and exhibited excellent cycle stability, retaining 95.3% of its capacity after 50 cycles, compared to only 66% retention for the core material alone. Thermal analysis further revealed that the exothermic decomposition peak shifted from 225 °C to 280 °C, reducing heat generation and improving safety. In 2011, this was refined with the design of  $\text{Li}[\text{Ni}_{0.83}\text{Co}_{0.07}\text{Mn}_{0.10}]\text{O}_2$ , incorporating a Ni-rich core

( $\text{Li}[\text{Ni}_{0.9}\text{Co}_{0.05}\text{Mn}_{0.05}]\text{O}_2$ ) and a Ni-depleted shell ( $\text{Li}[\text{Ni}_{0.68}\text{Co}_{0.12}\text{Mn}_{0.20}]\text{O}_2$ ). This modification increased capacity to 200 mA h g<sup>−1</sup>, with 96.9% retention after 50 cycles, compared to 79.2% for the core material alone. Thermal stability also improved, as the exothermic peak shifted to 227 °C.<sup>272</sup>

Building on this in 2012, they later introduced the FCG cathode,  $\text{LiNi}_{0.75}\text{Co}_{0.10}\text{Mn}_{0.15}\text{O}_2$ , optimizing metal distribution to achieve 215 mA h g<sup>−1</sup> and 90% retention after 1000 cycles. The exothermic reaction was further delayed to 250 °C, significantly reducing thermal risks.<sup>278</sup> This progression from core–shell (2010) to gradient (2011) to fully optimized FCG (2012) established a clear pathway for developing high-energy, long-life cathodes suited for EVs and grid storage applications. Noh *et al.*<sup>279</sup> further highlighted the superior performance of FCG nanorod-structured  $\text{Li}[\text{Ni}_{0.54}\text{Co}_{0.16}\text{Mn}_{0.30}]\text{O}_2$  cathode material compared to conventional cathode materials  $\text{Li}[\text{Ni}_{0.5}\text{Co}_{0.2}\text{Mn}_{0.3}]\text{O}_2$  (NCM523) and  $\text{Li}[\text{Ni}_{0.33}\text{Co}_{0.33}\text{Mn}_{0.33}]\text{O}_2$  (NCM333). The FCG exhibited an initial discharge capacity of 183.7 mA h g<sup>−1</sup>, outperforming the conventional constant composition NCM523 at 174.9 mA h g<sup>−1</sup> and NCM333 at 162.5 mA h g<sup>−1</sup>. After 100 cycles, the FCG material retained 93.2% of its capacity, compared to 89.9% for NCM523 and 92.4% for NCM333. At −20 °C, the FCG also showed higher capacity retention,

confirming its superior electrochemical stability and cycling performance. Chong *et al.*<sup>280</sup> demonstrated that gradient cathodes consistently achieve high discharge capacities (Fig. 16c), exceeding 200 mA h g<sup>-1</sup> across multiple configurations.

The compositional gradient, particularly in TSFCG85, also resulted in superior cycling stability, with over 90% capacity retention after 100 cycles. Concentration gradient strategies, while widely used in Ni-rich layered cathodes, are also applied to Li-rich layered oxides and 5 V spinel cathodes. Wu *et al.*<sup>276</sup> designed a Li-rich layered oxides with an FCG structure to enhance its electrochemical performance. By creating Li-rich layered oxide particles with a core-to-surface gradient, featuring a decrease in Mn and an increase in Ni and Co concentrations (Fig. 16d and e), they addressed common issues such as voltage decay and poor cycling stability. The gradient-tailored Li-rich layered oxides achieved 88.4% capacity retention after 200 cycles at 200 mA g<sup>-1</sup>, with an average voltage decay of just 0.8 mV per cycle. Additionally, thermal stability was improved, with a 41% reduction in heat release rate. This study demonstrated that the FCG design effectively suppresses voltage decay and enhances both cycling and thermal stability, making it a promising approach for Li-rich cathode materials. Similarly, Cheng *et al.*<sup>281</sup> investigated the synthesis and electrochemical performance of Li-rich Mn-based oxides with a concentration-gradient structure to improve cycling retention. They employed a co-precipitation and sol-gel method to create a CSG structure, where Mn<sub>0.75</sub>Ni<sub>0.25</sub>C<sub>2</sub>O<sub>4</sub> was used as the core and Li<sub>1.2</sub>Mn<sub>0.54</sub>Ni<sub>0.13</sub>Co<sub>0.13</sub>O<sub>2</sub> as the shell. The CSG cathode demonstrated significant improvements in cycling stability, achieving 95.4% capacity retention after 100 cycles at 1C, and the initial Coulombic efficiency increased by 12% to 85%. Structural analysis indicated that the concentration-gradient design reduced Li/Ni mixing and improved Li<sup>+</sup> diffusion, contributing to enhanced electrochemical performance and long-term stability.

For 5 V spinel cathodes, Zhang *et al.*<sup>277</sup> developed a gradient Li<sub>1+x</sub>Mn<sub>2-x</sub>O<sub>4</sub> structure to enhance cycling stability in LIBs. The gradient-Li<sub>1+x</sub>Mn<sub>2-x</sub>O<sub>4</sub> exhibited a stable capacity of ~105 mA h g<sup>-1</sup> over 250 cycles with over 99% Coulombic efficiency, outperforming raw LiMn<sub>2</sub>O<sub>4</sub>, whose capacity dropped from ~120 mA h g<sup>-1</sup> to 76 mA h g<sup>-1</sup>. The gradient design, with a Li-rich surface, mitigated Mn dissolution and the Jahn-Teller distortion, significantly improving capacity retention and stability compared to homogeneous doping. Although concentration gradient strategies provide enhanced stability by tailoring the chemical composition from the core to the surface, another effective structural modification lies in reshaping primary particles into nanorod structures.

**b. Nanorod cathode structures.** This approach entails reshaping the primary particles into tightly packed elongated rod-like structures that are oriented radially. The elongated structure of the nanorods promotes Li<sup>+</sup> movement by aligning the Li-containing (003) planes outwardly to provide a straight, shortest pathways for Li<sup>+</sup> diffusion (Fig. 17a and b). It also allows for homogenous tensile stress dissipation, allowing for better absorption of the anisotropic lattice strain caused during phase

transition. As a result, the microcrack degradation pathway is suppressed during prolonged cycling, preventing capacity fading and impedance increase from electrolyte penetration (Fig. 17c).<sup>41,282,283</sup> These nanorod structures, also observed in gradient-structured cathode materials, have been shown to outperform their constant concentration counterparts as highlighted by Sun *et al.*<sup>284</sup> where the Li[Ni<sub>0.81</sub>Co<sub>0.06</sub>Mn<sub>0.13</sub>]O<sub>2</sub> nanorod gradient cathode (NRG81), delivered a discharge capacity of 225 mA h g<sup>-1</sup> with 91% capacity retention over 100 cycles in half cells. In full cell tests, NRG81 retained 88.3% capacity after 1000 cycles, whereas its counterpart without nanorod (CC82), only retained 55.9% (Fig. 17d). Thermal stability tests performed on both cathode materials also showed that the NRG81 delayed the transition to the rock-salt phase until 390 °C compared to 320 °C for (CC82), demonstrating its improved safety under high-temperature conditions. As indicated by Noh *et al.*<sup>285</sup> these rod-shaped particles grow radially from the center of the particle and extend to lengths of up to 2.5 μm. These elongated primary particles are arranged in a crystallographic texture that aligns their *c*-axis in the transverse direction, which is crucial for improving Li<sup>+</sup> diffusion and enhancing electrochemical kinetics. This unique nanorod structure significantly contributes to the material's high-rate capability, low-temperature performance, and thermal stability.

Although nanorod-structured cathodes are characteristic of concentration gradient cathodes, they can be synthesized through doping uniform composition cathodes with high oxidation dopants. These dopants influence the crystal growth process by altering nucleation and growth kinetics, which leads to anisotropic crystal growth and the formation of elongated nanorods rather than conventional polyhedral morphologies.<sup>287–289</sup> Sun *et al.*<sup>286</sup> explored the stabilization of a highly Ni-rich cathode, Li[Ni<sub>0.89</sub>Co<sub>0.10</sub>Sb<sub>0.01</sub>]O<sub>2</sub> (NCSb89), using a flower-petal nanograin structure. This alignment improved Li<sup>+</sup> diffusion and reduced the harmful effects of the H<sub>2</sub> → H<sub>3</sub> phase transition. NCSb89 retained 95.0% of its capacity after 100 cycles in half-cells and 83.9% after 1000 cycles in full cells. It also delayed the rock-salt phase transition until 390 °C, compared to 320 °C for the undoped material. The dense nanograins minimized microcracks and electrolyte seepage, enhancing both cycling performance and safety. To further understand the role of high-oxidation-state dopants in stabilizing Ni-rich layered cathodes, Sun *et al.*<sup>290</sup> studied Mg<sup>2+</sup>, Al<sup>3+</sup>, Ti<sup>4+</sup>, Ta<sup>5+</sup>, and Mo<sup>6+</sup> in Li[Ni<sub>0.91</sub>Co<sub>0.09</sub>]O<sub>2</sub> (NC90). Ta<sup>5+</sup> and Mo<sup>6+</sup> significantly improved cycling stability, with pouch-type full cells retaining 81.5% capacity after 3000 cycles at 200 mA g<sup>-1</sup>. The dopants induced a nanorod grain structure, reducing microcracks and electrolyte infiltration. These dopants also enhanced Li/TM cation ordering, stabilizing the layered structure and suppressing the H<sub>2</sub> → H<sub>3</sub> phase transition. Charge-transfer resistance remained lower over 100 cycles, improving Li-ion transport. The study established a direct correlation between oxidation state, particle morphology, and electrochemical performance (Fig. 17e–g), offering a strategy to enhance cycle life and thermal stability in high-Ni cathodes.



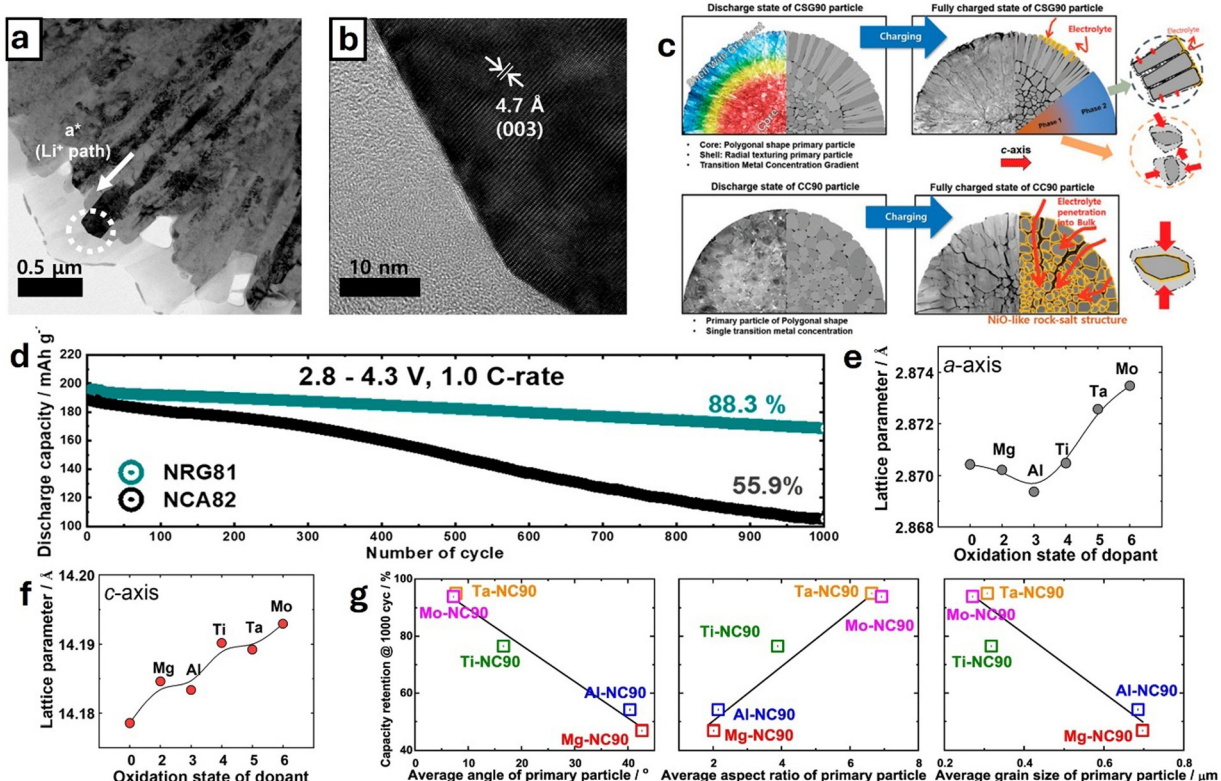


**Fig. 17** (a) TEM image of the NCSb89 grains showing the Li diffusion channels (b) HR-TEM image of the circled region in (a). Reproduced with permission from ref. 286. Copyright 2020, American Chemical Society. (c) Morphological design of nanorod cathode (top) preventing electrolyte penetration, and typical cathode (bottom) failing to prevent electrolyte penetration during charging. Reproduced under the terms of the Creative Commons CC-BY-NC-ND license.<sup>41</sup> Copyright 2020, American Chemical Society. (d) Comparison of long-term cycling (1000 cycles) performances of NRG81 vs. CC82 in pouch-type full-cells at 1.0C cycling rate. Reproduced with permission from ref. 284. Copyright 2019, American Chemical Society. (e) *a*-Axis lattice parameters. (f) *c*-Axis lattice parameters and (g) summaries of the capacity retention values after 1000 cycles as functions of average angle of primary particle, aspect ratio, and grain size. Reproduced with permission from ref. 287. Copyright 2021, The Authors.

Overall, nanorod structures contribute to a safer battery system by minimizing the formation and propagation of micro-cracks. The homogenous stress distribution and reduced impedance growth further enhance thermal stability, making nanorod cathodes a safer option for high-performance LIBs.

Li-rich layered oxide cathodes can also be synthesized into nanorods with improved rate capability and enhanced material utilization stemming from shorter electron and ion transport pathways. Chen *et al.*<sup>291</sup> synthesized porous Li-rich oxide nanorods,  $\text{Li}[\text{Li}_{0.19}\text{Mn}_{0.32}\text{Co}_{0.49}]\text{O}_2$ . The nanorods, with diameters of  $\sim 200$  nm and composed of 20 nm subunit particles, featured a hierarchical porous structure that significantly enhanced electrochemical performance. These nanorods delivered a discharge capacity of  $267 \text{ mA h g}^{-1}$  at 0.2C and retained a capacity of  $145.4 \text{ mA h g}^{-1}$  at 5C, demonstrating improved rate capability.

**ii. Surface coating.** While structural modification methods can alleviate defect formation in cathode materials, degradation caused by surface-related reactions, such as HF corrosion and CEI degradation, are not sufficiently addressed by structural modification.<sup>292</sup> To address these challenges, surface coating has emerged as a simple and effective strategy to protect the electrode surface. Doing so builds a stable surface

layer on the cathode surface that reduces the dissolution of transition metal ions and enhances surface structural stability. There is a wide range of surface coating materials available, including metal oxides like  $\text{Al}_2\text{O}_3$ ,  $\text{TiO}_2$ , and  $\text{MgO}$ ; metal fluorides such as  $\text{LiF}$  and  $\text{AlF}_3$ ; phosphates like  $\text{MnPO}_4$ ,  $\text{AlPO}_4$ , and  $\text{Si}_3(\text{PO}_4)_4$ ; solid-state electrolytes like  $\text{Li}_3\text{PO}_4$ ,  $\text{LiNbO}_3$ , and  $\text{Li}_2\text{ZrO}_3$ ; and conductive organic materials like polyimide and polyaniline.<sup>293–297</sup> Herein we focus on discussing the degradation mitigation mechanism of fluorides and phosphates as surface coating material for Ni-rich layered, Li-rich layered, and 5 V spinel cathode.

***a. Fluoride-coated cathodes.*** Fluoride-coating has emerged as a promising strategy to mitigate surface degradation in cathode materials. By forming a stable protective layer on the cathode surface, fluorine minimizes side reactions with the electrolyte, reduces transition metal dissolution, and enhances the overall electrochemical stability. Fluoride compounds are generally chemically inert and are not easily reduced or oxidized during cycling conditions. The introduction of  $\text{F}^-$  has been shown to improve the rate performance and cycling stability of LIB cathodes, while also lowering charge transfer resistance. The high electronegativity of fluoride ions facilitates the formation

of LiF, which enhances the interfacial stability of cathode materials.<sup>298–300</sup>

*i. Ni-rich layered oxide cathode.* In Ni-rich layered cathode, these coatings serve as HF passivating layers that reduce the acidity of non-aqueous electrolytes on the cathode surface and suppress metal dissolution from the cathode materials. They act as a physical protection layer that protects the cathode surface from HF attack and electrolyte decomposition (Fig. 18a).<sup>301</sup> Lee *et al.*<sup>302</sup> investigated the impact of an AlF<sub>3</sub> coating on the long-term cycling performance of Li[Ni<sub>0.8</sub>Co<sub>0.15</sub>Al<sub>0.05</sub>]O<sub>2</sub> cathodes. Using a dry coating process, they applied a 50 nm AlF<sub>3</sub> layer to the cathode surface. The AlF<sub>3</sub>-coated cathodes exhibited improved electrochemical performance, particularly at elevated temperatures. At 55 °C, the coated cathode demonstrated capacity retention of 84.7% after 100 cycles, compared to 79.1% for the uncoated version. In long-term cycling tests at room temperature, the coated cathode maintained 86.2% of its capacity after 1000 cycles, while the uncoated sample retained only 66.5%. This improvement was attributed to the AlF<sub>3</sub> layer's ability to suppress TM dissolution, reduce charge transfer resistance, and prevent particle pulverization during cycling (Fig. 18b–e), ultimately enhancing the cathode's structural

stability and thermal safety. Xie *et al.*<sup>303</sup> investigated the effects of 10 different fluoride coatings on the cycling stability of high-voltage LiNi<sub>0.5</sub>Co<sub>0.2</sub>Mn<sub>0.3</sub>O<sub>2</sub> (NCM523) cathodes, focusing on mitigating interfacial reactions between the cathode and electrolyte. They found that AlF<sub>3</sub>-coated NCM523 showed the best performance, retaining 88% of its capacity after 200 cycles at 4.5 V, compared to 56% for the uncoated sample. The 2.7 nm AlF<sub>3</sub> coating effectively suppressed interfacial reactions and maintained structural stability. Other fluorides, such as YF<sub>3</sub> and ZrF<sub>4</sub>, also improved performance, but to a lesser extent. The result showed that coatings with a suspension pH near 4.0 and small cation ionic radii provide strong protection, with AlF<sub>3</sub> being particularly effective in enhancing the longevity of NCM523 cathodes. Wang *et al.*<sup>304</sup> developed a solvothermal method using trifluoroethanol to *in situ* construct a uniform fluoride coating layer on Ni-rich LiNi<sub>0.83</sub>Co<sub>0.12</sub>Mn<sub>0.05</sub>O<sub>2</sub> (NCM) cathode materials. The fluoride coating significantly enhanced the chemical stability of NCM against air and reduced side reactions between the cathode and the electrolyte. After four weeks of air aging, the fluoride-coated NCM (NCM-F) maintained a high initial capacity of 166.96 mA h g<sup>-1</sup> compared to 105.65 mA h g<sup>-1</sup> for the uncoated NCM, with a much lower voltage polarization. The NCM-F retained 84.91% capacity

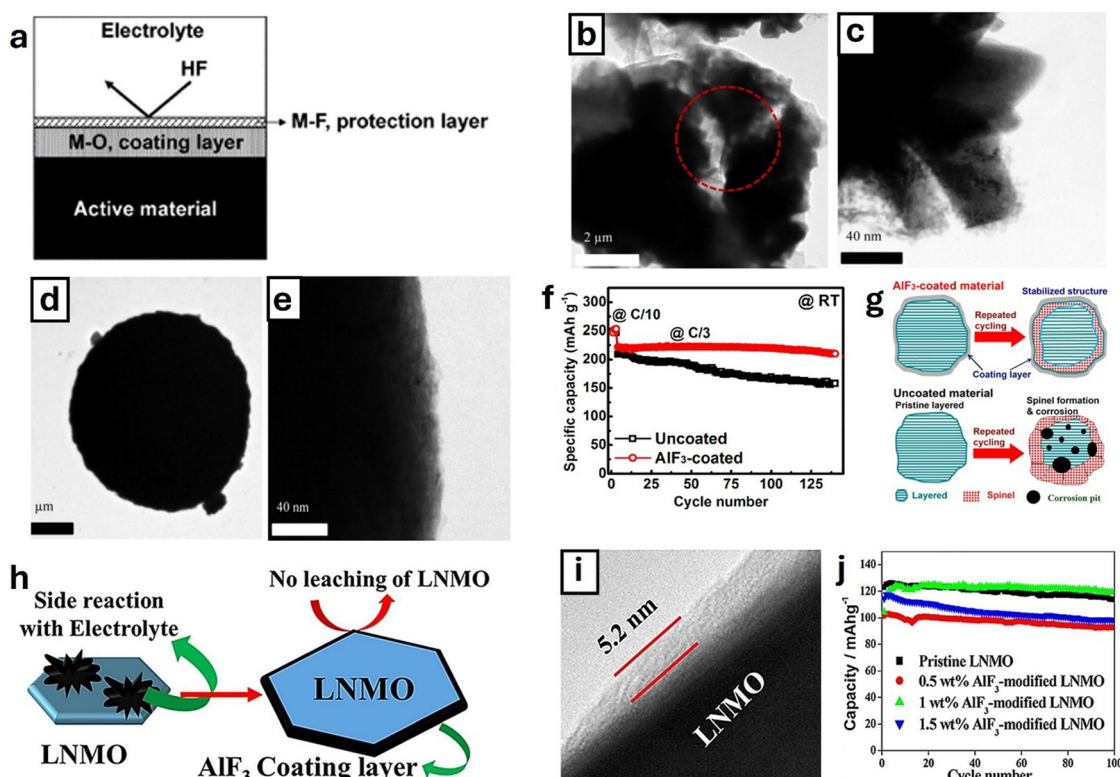


**Fig. 18** (a) Schematic drawing of the interface between the cathode and electrolyte. Reproduced from ref. 301. Copyright 2016, American Chemical Society. TEM bright-field images of (b) the pristine Li[Ni<sub>0.8</sub>Co<sub>0.15</sub>Al<sub>0.05</sub>]O<sub>2</sub>. (c) Magnified images of (b). (d) The AlF<sub>3</sub>-coated Li[Ni<sub>0.8</sub>Co<sub>0.15</sub>Al<sub>0.05</sub>]O<sub>2</sub>, and (e) magnified images of (d) after 500 cycles at 55 °C. Reproduced with permission from ref. 302. Copyright 2013, Elsevier B.V. (f) Cycling performance of uncoated and AlF<sub>3</sub>-coated Li-rich Mn-rich layered oxide (Li<sub>1.2</sub>Ni<sub>0.15</sub>Co<sub>0.10</sub>Mn<sub>0.55</sub>O<sub>2</sub>) and (g) schematics of the microstructural changes of uncoated and AlF<sub>3</sub>-coated Li-rich Mn-rich. Reproduced with permission from ref. 306. Copyright 2014, American Chemical Society. (h) Schematic of on AlF<sub>3</sub> coating on LNMO surface, (i) TEM images of 1.0% wt% AlF<sub>3</sub>-modified LNMO material, and (j) cycling performance of pristine versus AlF<sub>3</sub>-modified LNMO materials. Reproduced with permission from ref. 307. Copyright 2020, Elsevier B.V.



after 200 cycles compared to 61.32% for the uncoated sample. In a recent work by Ryu *et al.*,<sup>305</sup> fluorine coating significantly improved the stability of Ni-rich layered cathode  $\text{Li}[\text{Ni}_{0.9}\text{Co}_{0.05}\text{Mn}_{0.045}\text{Nb}_{0.005}]\text{O}_2$  (Nb-CSG90). The F-Co-washed cathode retained 65% capacity after 6000 cycles, compared to 55.2% for unwashed and 63.7% for DI-washed cathodes. In pouch-type full cells, capacity retention after 1000 cycles reached 93% for F-Co-washed cathode, outperforming 87.1% for F-coated-only and 85.6% for Co-washed-only cathode. Gas evolution at 60 °C storage was also substantially reduced, lowering battery swelling and enhancing safety. XPS analysis confirmed LiF formation, which suppressed electrolyte decomposition and HF attack, while EIS measurements showed lower resistance growth, ensuring stable Li-ion transport over prolonged cycling.

*ii. Li-rich layered oxide cathode.* In Li-rich layered cathodes, fluoride coatings suppress the release of oxygen, maintaining vacancy levels in regions where oxygen is deficient. As reported by Zheng *et al.*,<sup>306</sup>  $\text{AlF}_3$  coating on Li- and Mn-rich cathode materials, was found to significantly enhance electrochemical performance. Using STEM and electron energy loss spectroscopy, they observed microstructural and electronic changes before and after cycling and found that the  $\text{AlF}_3$  coating effectively reduced electrolyte oxidation at high voltages, suppressed the formation of a thick SEI, and protected the electrode surface from etching and corrosion (Fig. 18f). Furthermore, the coating mitigated the layered-to-spinel phase transformation in the bulk material (Fig. 18g), which is typically responsible for voltage fade. Zhao *et al.*<sup>308</sup> investigated the enhancement of Li-rich cathode materials using a eutectic melting salt treatment to apply a  $\text{LiF}-\text{MgF}_2-\text{CaF}_2$  fluoride coating and doping to  $\text{Li}_{1.2}\text{Ni}_{0.13}\text{Fe}_{0.13}\text{Mn}_{0.54}\text{O}_2$ . The fluoride coating suppressed oxygen release and mitigated transition metal dissolution, while the doping improved  $\text{Li}^+$  diffusion kinetics and stabilized the bulk crystal structure. As a result, the treated cathode achieved 90.1% capacity retention after 120 cycles at 0.2C, with improved rate capability and thermal stability. Wang *et al.*<sup>309</sup> explored the effect of fluorination on Li- and Mn-rich (LMR) layered oxide cathodes, focusing on improving their cycling performance and addressing issues like capacity and voltage fade. Using a single-crystal  $\text{Li}_{1.2}\text{Ni}_{0.2}\text{Mn}_{0.6}\text{O}_2$  platform, they applied *in situ* fluorination to develop a gradient distribution of  $\text{Mn}^{3+}$  from the surface to the bulk, contributing to the formation of a Ni-rich spinel phase on the surface and a coherent spinel-layered structure in the bulk. This structural enhancement significantly improved the specific capacity and capacity retention of the fluorinated cathodes, highlighting fluorination as a promising strategy for enhancing the stability and performance of Li-rich cathodes.

*iii. 5 V spinel cathode.* Although designing electrolytes with an electrochemical stability window of ~5 V has been proposed as a primary solution for 5 V spinel cathodes, surface coating has shown potential in minimizing the cathode's reaction with the electrolyte to prevent electrolyte decomposition, and inhibit Mn dissolution (Fig. 18h).<sup>310</sup> Zheng *et al.*<sup>311</sup> investigated the

stabilization of the 5 V spinel  $\text{LiNi}_{0.5}\text{Mn}_{1.5}\text{O}_4$  (LNMO) cathode in organic electrolytes using a liquid-applied polyvinylidene fluoride (PVdF) coating. The PVdF-wrapped LNMO retained 97.8% capacity after 300 cycles at room temperature and 86.1% at 55 °C, compared to rapid degradation in the uncoated sample. The PVdF layer effectively reduced Mn dissolution, electrolyte decomposition, and the formation of a thick SEI layer, leading to reduced impedance growth and enhanced electrochemical performance.

Chu *et al.*<sup>307</sup> demonstrated that a 1 wt%  $\text{AlF}_3$  coating on  $\text{LiNi}_{0.5}\text{Mn}_{1.5}\text{O}_4$  (LNMO) cathodes (Fig. 18i) improved high-temperature performance, where the  $\text{AlF}_3$ -modified LNMO showed 81.7% capacity retention after 100 cycles at 55 °C, compared to 70.1% for the unmodified LNMO (Fig. 18j). This enhancement is attributed to the  $\text{AlF}_3$  layer's ability to suppress electrolyte decomposition and transition metal dissolution to stabilize the electrode during cycling. Despite not increasing the initial discharge capacity, the coating effectively improved cyclability under elevated temperatures. Li *et al.*<sup>312</sup> investigated the impact of a  $\text{LaF}_3$  nanolayer coating on the performance of  $\text{LiNi}_{0.5}\text{Mn}_{1.5}\text{O}_4$  (LNMO) cathode materials. The study found that a 4 wt%  $\text{LaF}_3$  coating significantly improved capacity retention, achieving 92% retention after 150 cycles, compared to 74.7% for uncoated LNMO. Additionally, the  $\text{LaF}_3$ -coated LNMO showed improved rate capability and resistance to impedance growth during cycling.

Fluoride coatings, especially materials like  $\text{AlF}_3$ , provide a robust protective barrier against electrolyte degradation and transition metal dissolution. Their high stability and ability to suppress side reactions make them indispensable for enhancing the long-term performance and safety of high-voltage cathodes.

*b. Phosphate coating.* Phosphate-based coatings are proving to be a highly effective solution for mitigating degradation in Ni- and Li-rich layered oxide cathode materials, primarily due to the strength of the P=O bond. This bond significantly enhances the thermal stability of the cathode by preventing oxygen release from the cathode lattice, even at elevated temperatures. The improvement is largely attributed to the strong affinity of phosphorus for oxygen, which stabilizes the oxygen framework within the cathode, reducing degradation and improving overall performance.<sup>299</sup>

*i. Ni-rich layered oxide cathode.* Using first-principles calculations, Min *et al.*<sup>313</sup> reported that the electrochemical performance of  $\text{LiNi}_{0.91}\text{Co}_{0.06}\text{Mn}_{0.03}\text{O}_2$  improved after the application of metal phosphate coatings. They screened 16 metal phosphate (MP) materials based on their reactivity with lithium oxide ( $\text{Li}_2\text{O}$ ), which is known to contribute to gas generation and degradation in batteries. They identified  $\text{Mn}_3(\text{PO}_4)_2$ ,  $\text{Co}_3(\text{PO}_4)_2$ , and  $\text{Fe}_3(\text{PO}_4)_2$  as the most effective coatings for removing Li residues and reducing capacity fade (Fig. 19a). Experimental validation confirmed that  $\text{Co}_3(\text{PO}_4)_2$ -coated cathodes retained 76.68% capacity after 50 cycles, with  $\text{Fe}_3(\text{PO}_4)_2$  and  $\text{Mn}_3(\text{PO}_4)_2$  showing retention rates of 77.16% and 73.08%, respectively. In contrast,  $\text{TiPO}_4$  demonstrated poor



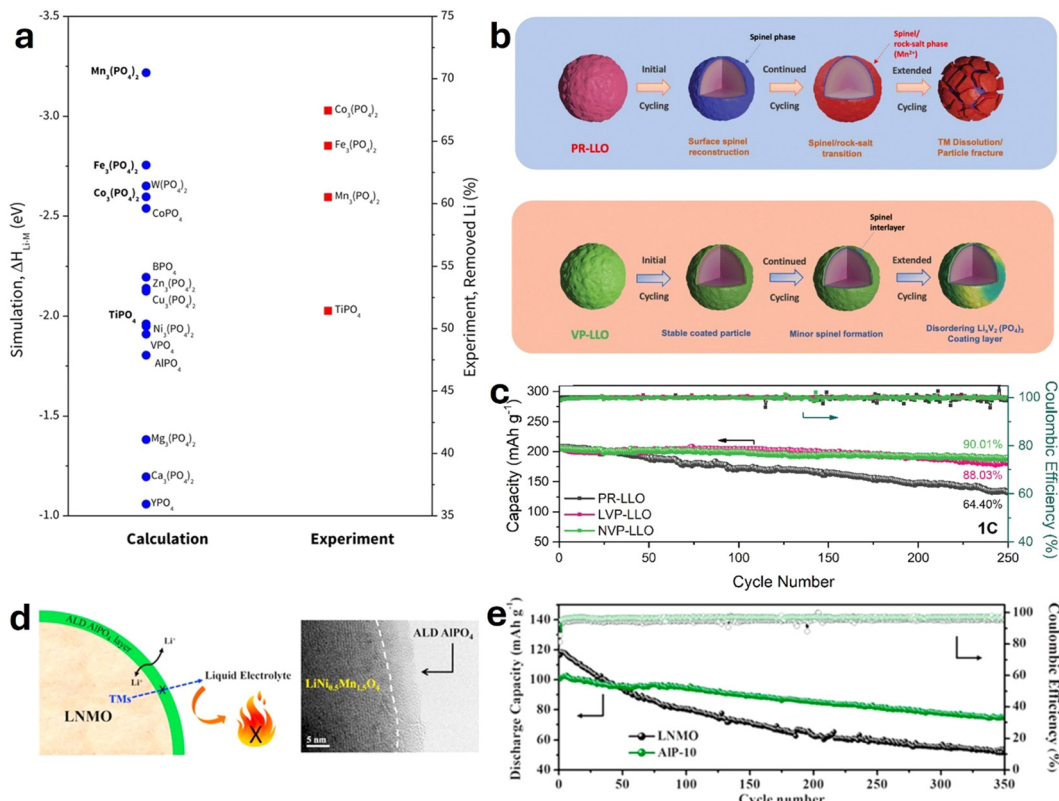


Fig. 19 (a) Comparison of Li-removal reactivity from calculations and experiments showing the most effective coatings for removing Li residues and reducing capacity fade. Reproduced with permission from ref. 313. Copyright 2017, The Author(s). (b) Schematic diagram of the chemical evolution of pristine and LVP/NVP-coated Li-rich layered oxide particles during extended cycling, and (c) cycle performance of PR-Li-rich layered oxide, LVP-Li-rich layered oxide and NVP Li-rich layered oxide across 250 cycles (1C). Reproduced with permission from ref. 315. Copyright 2022, Royal Society of Chemistry. (d) Schematics illustrating atomic layer deposition of AlPO<sub>4</sub> thin film as a coating material for LNMO electrodes to circumvent safety issues, and (e) long cycling performances and coulombic efficiency of bare LNMO and AlP-10 over 350 cycles under 0.5C. Reproduced with permission from ref. 316. Copyright 2017, Elsevier Ltd.

performance. The study concluded that  $\text{Co}_3(\text{PO}_4)_2$  is an optimal coating material for improving the cycle life and capacity retention of Ni-rich cathode materials. Long *et al.*<sup>314</sup> improved the electrochemical performance of  $\text{LiNi}_{0.8}\text{Co}_{0.1}\text{Mn}_{0.1}\text{O}_2$  (NCM811) cathodes using a composite phosphate and borate coating. The modified cathode achieved a higher specific capacity of 152 mA h g<sup>-1</sup> over the pristine NCM811 at 5C and retained 85.4% capacity after 200 cycles at 4.5 V. The coating reduced charge transfer resistance and enhanced thermal stability, making the cathode more suitable for high-voltage and high-temperature applications.

*ii. Li-rich layered oxide cathode.* Strong phosphate–oxygen bonds have been utilized to prevent oxygen loss from the Li-rich layered cathode lattice. The robust covalent bond between the  $\text{PO}_4^{3-}$  polyanion and the metal ions in the phosphate coating limits interaction between the Li-rich layered cathode and the electrolyte, enhancing both the structural and thermal stability of the material.<sup>317</sup>

Jenkins *et al.*<sup>315</sup> investigated the regulation of surface oxygen activity through the application of  $\text{Li}_3\text{V}_2(\text{PO}_4)_3$  and  $\text{Na}_3\text{V}_2(\text{PO}_4)_3$  surface coating, where the electronic bond structure between the  $\text{Li}_{1.2}\text{Mn}_{0.54}\text{Ni}_{0.13}\text{Co}_{0.13}\text{O}_2$  vanadium phosphate coatings

were aligned. This alignment mitigated common issues such as oxygen release, voltage fade, and the layered-to-spinel phase transition (Fig. 19b). As a result, the vanadium phosphate-coated Li-rich layered oxides showed capacity retention of up to 90% and a reduced voltage fade of  $-0.315$  V after 250 cycles, significantly outperforming pristine samples (Fig. 19c). They concluded that band-aligned surface coatings can effectively lower charge transfer resistance and improve the structural stability of high-energy cathode materials.

*iii. 5 V spinel cathode.* Phosphate coating in 5 V spinel cathode has also shown improvement. For example, Yi *et al.*<sup>318</sup> explored the application of a  $\text{FePO}_4$  coating on  $\text{LiNi}_{0.5}\text{Mn}_{1.5}\text{O}_4$  (LNMO) cathodes, which was synthesized *via* a sol-gel method, with various coating levels (0.5 wt%, 1 wt%, 3 wt%). The coating level of 1 wt%  $\text{FePO}_4$  was the most optimal, where the  $\text{FePO}_4$ -coated LNMO retained a discharge capacity of 117 mA h g<sup>-1</sup> at a 2C rate, compared to only 50 mA h g<sup>-1</sup> for the uncoated LNMO after 80 cycles. The  $\text{FePO}_4$  coating effectively stabilized the interface between the LNMO cathode and the electrolyte, reducing charge transfer resistance and improving  $\text{Li}^+$  diffusion, which contributes to the improved performance of the battery. Deng *et al.*<sup>316</sup> explored the use of ultrathin atomic layer

deposition (ALD) of  $\text{AlPO}_4$  on  $\text{LiNi}_{0.5}\text{Mn}_{1.5}\text{O}_4$  cathode to improve its electrochemical performance and safety (Fig. 19d). The study demonstrated that applying 10 ALD cycles of  $\text{AlPO}_4$  on  $\text{LiNi}_{0.5}\text{Mn}_{1.5}\text{O}_4$  cathode showed an excellent capacity retention of 94% after 100 cycles, compared to 69% for the uncoated LNMO (Fig. 19e). The coating also reduced side reactions, minimized Mn dissolution, and improved thermal stability, with the exothermic peak of the  $\text{AlPO}_4$ -coated LNMO appearing at 225.2 °C, compared to the 217.6 °C of bare LNMO.

*iv. Dual-function phosphate coating.* Lithium phosphate ( $\text{Li}_3\text{PO}_4$ ) has been reported to serve a dual function as a coating material, with  $\text{Li}^+$  facilitating charge transfer reactions across the electrode–electrolyte interface. Li *et al.*<sup>319</sup> demonstrated the dual functionality of an *in situ*  $\text{Li}_3\text{PO}_4/\text{AlPO}_4$  coating formed *via*  $\text{LiH}_2\text{PO}_4$ -assisted  $\text{Li}_2\text{CO}_3$  washing to enhance NCA cathodes. The coating removed residual Li compounds, stabilizing the surface and suppressing electrolyte decomposition. The modified NCA exhibited a higher discharge capacity (185.0 mA h g<sup>-1</sup> at 0.2C) and 90.3% capacity retention after 500 cycles at 1C, outperforming uncoated samples. EIS confirmed a lower charge transfer resistance, CV showed reduced voltage polarization and stabilized phase transitions, and a uniform phosphate layer was verified using TEM. These results establish  $\text{Li}_3\text{PO}_4$  as a dual-function coating, providing both surface protection and  $\text{Li}^+$  conductivity.

Lie *et al.*<sup>320</sup> reported similar dual functionality in Li-rich cathodes. They investigated the *in situ* application of a lithium phosphate ( $\text{Li}_3\text{PO}_4$ ) coating on Li-rich Mn-based cathode materials. The coating was formed during synthesis through a carbonate–phosphate precipitate conversion reaction, creating a  $\text{Li}_3\text{PO}_4$  layer less than 30 nm thick on the cathode surface. The coated Li-rich Mn-based cathode showed enhanced cycling stability, retaining 81.8% of capacity after 175 cycles at 0.5C, compared to 72.9% for uncoated materials. Additionally, the  $\text{Li}_3\text{PO}_4$  coating reduced voltage decay to 1.09 mV per cycle and improved  $\text{Li}^+$  transport, leading to overall better performance and reduced side reactions with the electrolyte.

## b. Anode

*i. Composite anode.* Composite anodes represent a key area of research aimed at improving the safety and performance of LIBs by combining two or more materials to balance high energy density with mechanical stability and long cycle life. A prominent example is the silicon–carbon composite anode, such as silicon-graphite. In silicon-graphite composites, the graphite is a buffer that accommodates Si's volume changes, maintaining structural integrity and electrical conductivity throughout cycling.<sup>321</sup> This buffering effect of graphite reduces the mechanical degradation and capacity loss associated with silicon anodes. Besides graphite, other carbon materials, such as carbon nanotubes, carbon nanofibers, graphene, and amorphous carbon have been employed as suitable carbon matrixes as well.<sup>322</sup>

Recent advancements have focused on optimizing silicon–carbon composites through nano structuring and introducing

artificial solid electrolyte interphase (A-SEI) layers.<sup>86</sup> The nano structuring approach, such as embedding Si nanoparticles in carbon/graphite matrices, minimizes the stress on individual Si particles and improves the overall contact between active materials and the conductive carbon network, offering improved performance and safety. For instance, Liu *et al.*<sup>323</sup> demonstrated a nano-/micro structured silicon–carbon composite with high tap density, where Si nanoparticles were uniformly embedded into a carbon matrix. This design improved volumetric energy density, enhanced structural stability, and provided 3D electron-transfer pathways. The composite exhibited excellent cycling performance, maintaining 600 mA h g<sup>-1</sup> after 1000 cycles.  $\text{SiO}_x/\text{C}$  composites are also considered promising, as the high specific capacity and minimal volume fluctuations of  $\text{SiO}_x$  stem from strong Si–O bonds and the formation of  $\text{Li}_2\text{O}$  during cycling.<sup>86</sup> These attributes make  $\text{SiO}_x$  composites highly attractive, offering better mechanical stability than pure Si anodes.

Applying A-SEI layers on Si anodes is another strategy to prevent electrolyte decomposition and stabilize  $\text{Li}^+$  transport in composite Si anodes. For instance, Abdollahifar *et al.*<sup>324</sup> developed a multifunctional polymeric, A-SEI protective layer to enhance the cycling stability and performance of silicon-on-graphite composite anodes (Fig. 20a–f). This approach addressed the inherent instability of the *in situ* SEI by applying a sulfonated chitosan (SCS) coating crosslinked with glutaraldehyde to form a robust and conductive A-SEI layer. The SCS coating not only improved the ionic conductivity but also provided mechanical strength to accommodate the volumetric expansion of silicon during cycling. Due to the cation-selective nature of the A-SEI, electrolyte decomposition and the parasitic reactions that typically lead to SEI thickening and capacity fading were significantly minimized. Furthermore, the study showed that the silicon-on-graphite/C-SCS anodes achieved a high specific capacity of over 600 mA h g<sup>-1</sup> at 0.1C and maintained long cycling stability, with over 67% capacity retention after 1000 cycles at 0.3C. In contrast to uncoated or conventionally coated electrodes, the SCS-modified anodes demonstrated reduced polarization and stable impedance profiles throughout prolonged cycling.

Zhu *et al.*<sup>325</sup> used a low-cost and scalable sol–gel method to deposit  $\text{Al}_2\text{O}_3$  coating as an A-SEI layer on silicon-graphite composite anodes. The  $\text{Al}_2\text{O}_3$  coating transformed into a  $\text{Li}^+$  conductive Li–Al–O layer during lithiation, enhancing ionic conductivity while physically shielding the electrode from electrolyte decomposition. The coated composite anode exhibited significantly improved cycling performance and capacity retention, maintaining 76.4% capacity after 100 cycles at room temperature, compared to 56.4% for uncoated anode material (Fig. 20g and h). Additionally, at 55 °C, the  $\text{Al}_2\text{O}_3$  coated anodes offered a capacity retention of 66.8% over 80 cycles, while the uncoated anodes retained only 27.6%.

*ii. Oxide anode.* While significant progress has been made in improving cathode materials, anodes have traditionally relied on graphite because of its incomparable balance of relatively low cost, abundance, high energy density, power



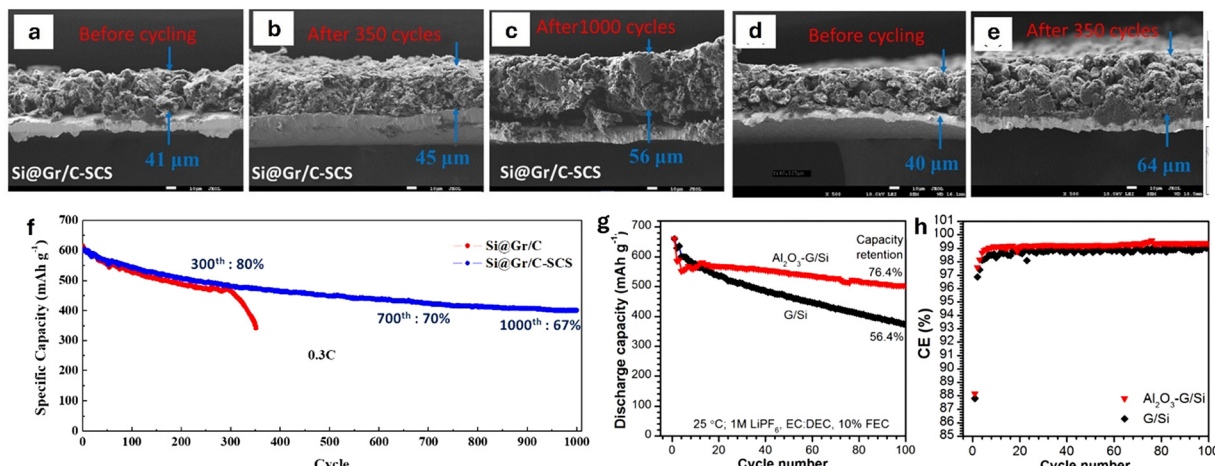


**Fig. 20** (a)–(c) Cross-sectional SEM images of silicon-graphite composite having A-SEI protective layer made of sulfonated chitosan (SCS) Si@Gr/C-SCS, and (d) and (e) silicon on graphite without A-SEI Si@Gr/C electrodes before and after cycling. (f) Cycling performance of the electrodes at 0.3C. Reproduced with permission from ref. 324. Copyright 2022, American Chemical Society. Cycling stability (g) and CE (h) of graphite-silicon (G/Si) and Al<sub>2</sub>O<sub>3</sub> coating on G/S composite anode. Reproduced with permission from ref. 325. Copyright 2021, IOP Publishing Ltd.

density, and very long cycle life.<sup>326</sup> However, the inherent low-capacity problem of graphite and its safety under high charge rate necessitates the need for higher-capacity alternatives to meet the market demand.<sup>327</sup> As discussed in the second section, graphite anodes face safety risks at high charge rates due to Li plating, where Li deposits on the surface as metal, forming dendrites that cause internal short circuits and thermal runaway.

Acknowledging these limitations, researchers have turned their focus toward oxide anodes as viable alternatives. Oxide anodes have emerged as a promising class of materials owing to their higher theoretical capacities and enhanced thermal stability from a reduced tendency for Li plating. These materials encompass a broad range of materials that can be categorized into two main types based on their Li storage mechanisms: conversion and intercalation type anodes. Fig. 21a shows a

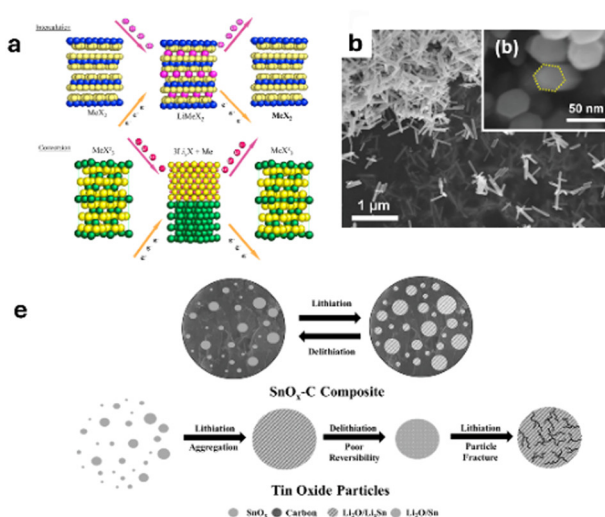


**Fig. 21** (a) Comparison of an intercalation and conversion mechanisms for the lithiation/delithiation of electrode materials. Reproduced with permission from ref. 331. Copyright 2007, Elsevier B.V. Illustration of conversion-type electrode lithiation behavior. (b) SEM images of  $\alpha$ -Fe<sub>2</sub>O<sub>3</sub> nanorods at a low magnification and (b) end-view at a high magnification. The yellow dashed line in panel b outlines the hexagonal structure of a single nanorod, (c) reversible capacities of  $\alpha$ -Fe<sub>2</sub>O<sub>3</sub> electrodes made with nanorods, submicrometer particles, and micrometer-sized particles. All electrodes cycled at 0.2C rate (201 mA g<sup>-1</sup>), and (d) electrochemical impedance spectroscopy of electrodes with  $\alpha$ -Fe<sub>2</sub>O<sub>3</sub> nanorods, submicrometer particles  $\alpha$ -Fe<sub>2</sub>O<sub>3</sub>, and micrometer-sized particles  $\alpha$ -Fe<sub>2</sub>O<sub>3</sub>. All measured after 100 cycles at 0.5C rate. Reproduced with permission from ref. 332. Copyright 2011, American Chemical Society. (e) Comparison of Sn<sub>Ox</sub>-C lithiation/delithiation versus unsupported tin oxide particle lithiation/delithiation and (f) long-term cyclic voltammograms of Sn<sub>Ox</sub>-C. Reproduced with permission from ref. 333. Copyright 2019, American Chemical Society. (g) Schematic Illustration of the nanoengineering strategies for high-performance conversion type anode materials for next-generation LIBs. Reproduced with permission from ref. 25. Copyright 2018, Elsevier Inc.



comparison of these two mechanisms. Conversion-type anodes, such as silicon oxides ( $\text{SiO}_x$ ), tin oxides ( $\text{SnO}_2$ ), and certain transition metal oxides, such as iron oxide ( $\text{Fe}_2\text{O}_3$ ,  $\text{Fe}_3\text{O}_4$ ), cobalt oxide ( $\text{Co}_3\text{O}_4$ ), manganese oxide ( $\text{MnO}_2$ ), and nickel oxide ( $\text{NiO}$ ), are known for their high theoretical capacities.<sup>328</sup> Intercalation-type anodes, including lithium titanate ( $\text{Li}_4\text{Ti}_5\text{O}_{12}$ ), titanium dioxide ( $\text{TiO}_2$ ), and lithium vanadate (LVO), offer excellent reversibility.<sup>329,330</sup> These materials operate at a higher potential ( $> 1.55 \text{ V versus Li/Li}^+$ ) and maintain zero-strain during cycling enhances their durability, making them particularly suitable for applications requiring high power and energy densities.

A key advantage of oxide anodes over graphite is their reduced risk of dendrite formation, which leads to improved reversibility. Hou *et al.*<sup>334</sup> demonstrated this by synthesizing a two-dimensional lamellar lithium titanate ( $\text{Li}_4\text{Ti}_5\text{O}_{12}$ , LTO) anode material, which effectively suppressed Li dendrite formation. With a high  $\text{Li}^+$  diffusion coefficient and minimal volume changes, LTO enhances both safety and performance. Synthesized from a titanium-based MXene precursor, the lamellar structure improved  $\text{Li}^+$  transport and charge transfer. Electrochemical tests showed that LTO achieved  $173 \text{ mA h g}^{-1}$  after 100 cycles at  $0.1\text{C}$  and retained 82% of its capacity after 1000 cycles at  $2\text{C}$ , positioning it as a strong candidate for alternative anode material suitable in high-performance batteries. Liu *et al.*<sup>335</sup> synthesized self-supported  $\text{Li}_4\text{Ti}_5\text{O}_{12}\text{-C}$  (LTO-C) nanotube arrays directly on stainless steel foil using a scalable template-based method. These arrays, designed for use as anode materials in flexible LIBs, demonstrated exceptional performance with reversible capacities of  $135 \text{ mA h g}^{-1}$ ,  $105 \text{ mA h g}^{-1}$ , and  $80 \text{ mA h g}^{-1}$  at charge/discharge rates of  $30\text{C}$ ,  $60\text{C}$ , and  $100\text{C}$ , respectively. The arrays also exhibited excellent cycling stability, retaining 93% of their capacity after 500 cycles at  $10\text{C}$ , with a capacity retention of  $144 \text{ mA h g}^{-1}$ . The carbon coating on the nanotubes significantly enhanced the electronic conductivity, contributing to a high-rate capability and long-term stability.

Conversion-type oxides, such as  $\text{Fe}_2\text{O}_3$  and  $\text{Fe}_3\text{O}_4$ , have proven to be promising high-capacity anode materials due to their affordability, high capacity, and nontoxic nature. Lin *et al.*<sup>332</sup> found that  $\alpha\text{-Fe}_2\text{O}_3$  nanorods as an anode material delivered high reversible capacities of  $908 \text{ mA h g}^{-1}$  at a  $0.2\text{C}$  rate and  $837 \text{ mA h g}^{-1}$  at a  $0.5\text{C}$  rate. The  $\alpha\text{-Fe}_2\text{O}_3$  nanorods averaged  $\sim 40 \text{ nm}$  in diameter and  $\sim 400 \text{ nm}$  in length, providing a short path for  $\text{Li}^+$  diffusion, reduced charge transfer resistance, and effective accommodation of the strain generated from the volume expansion during the lithiation/delithiation process (Fig. 21b-d). Chen *et al.*<sup>336</sup> designed a sea urchin-like  $\text{Fe}_3\text{O}_4\text{@C@NS-rGO}$  composite with nitrogen and sulfur co-doped graphene coating to improve the conductivity and provide fast ion-diffusion pathways. The composite exhibited a high reversible capacity of  $532.5 \text{ mA h g}^{-1}$  after 100 cycles at  $100 \text{ mA g}^{-1}$  with an energy density of  $232.1 \text{ W h kg}^{-1}$  when paired with a  $\text{LiCoO}_2$  cathode. Other oxide anodes, such as  $\text{SnO}_2$ , offer high capacity with stable cycling. Weeks *et al.*<sup>333</sup> developed a tin oxide–carbon ( $\text{SnO}_x\text{-C}$ ) composite through the

pyrolysis of a tin-citrate precursor. The resulting composite contained tin oxide nanocrystals surrounded by a flexible porous carbon framework. This structure enhanced reversibility during  $\text{Li}_2\text{O}$  formation (Fig. 21f), reduced particle aggregation, suppressed volume expansion, and improved cycling stability to deliver a high initial capacity of  $542 \text{ mA h g}^{-1}$  and retained 80.6% of this capacity after 400 cycles at  $1\text{C}$ .

Oxide anodes represent a significant advancement in LIB technology, offering enhanced safety, higher performance, and the potential for innovation. Their high theoretical capacities and improved thermal stabilities address the key limitations of traditional graphite anodes. Intercalation-type oxides provide excellent cycling stability and are suitable for high-rate applications due to their minimal volume change and higher operating potential. Conversion-type oxides offer the advantage of higher capacities to meet the demand for increased energy density. Continued research and development of these oxide anode materials are crucial for advancing LIBs technology to meet future energy storage needs (Fig. 21g).

### c. Electrolyte

Given the growing demand for safer, higher-energy-density batteries, extensive research has been conducted to develop newer electrolyte systems that enhance safety while maintaining or improving performance. This section discusses additives, solid electrolytes and aqueous electrolyte as approaches to improving electrolyte safety.

**i. Additives.** One widely employed strategy for improving LIB safety is the incorporation of electrolyte additives. Additives represent an economical and efficient approach to improving electrolyte performance and safety and has been a core direction of research in the field.<sup>337</sup>

Currently, additives are classified based on their specific roles, such as SEI film formation and flame retardancy. Film-forming additives are crucial for creating protective surface films on the electrodes. So far, reductive compounds comprising fluorine donating functional groups have been the most explored as SEI-forming additives, particularly for high-specific capacity anodes such as Li metal and Si. It is worth noting that fluorinated solvents, including ethers, attract considerable attention as electrolyte additions, owing to their wider electrochemical stability window, low flammability, and inherent ability to form effective surface films on electrodes and current collectors. Among these, Fluoroethylene carbonate (FEC) is the most commonly used. Schroder *et al.*<sup>338</sup> showed that FEC, when added to an EC/DEC electrolyte, significantly enhances the formation of a stable,  $\text{LiF}$ -rich SEI layer on Si anodes (Fig. 22a-f). They demonstrated that adding FEC resulted in a thicker SEI (35.1 nm) compared to the thinner SEI (23.1 nm) formed in the absence of FEC. The thicker, inorganic species-rich SEI effectively stabilized the anode surface, minimizing capacity loss during repeated cycling. The Si-anodes cycled in the FEC-containing electrolyte maintained a discharge capacity  $> 3000 \text{ mA h g}^{-1}$  after 100 cycles compared to  $1252 \text{ mA h g}^{-1}$  in the FEC absent electrolyte (Fig. 22g). From a safety perspective, this shows the FEC-containing electrolyte better curtails the



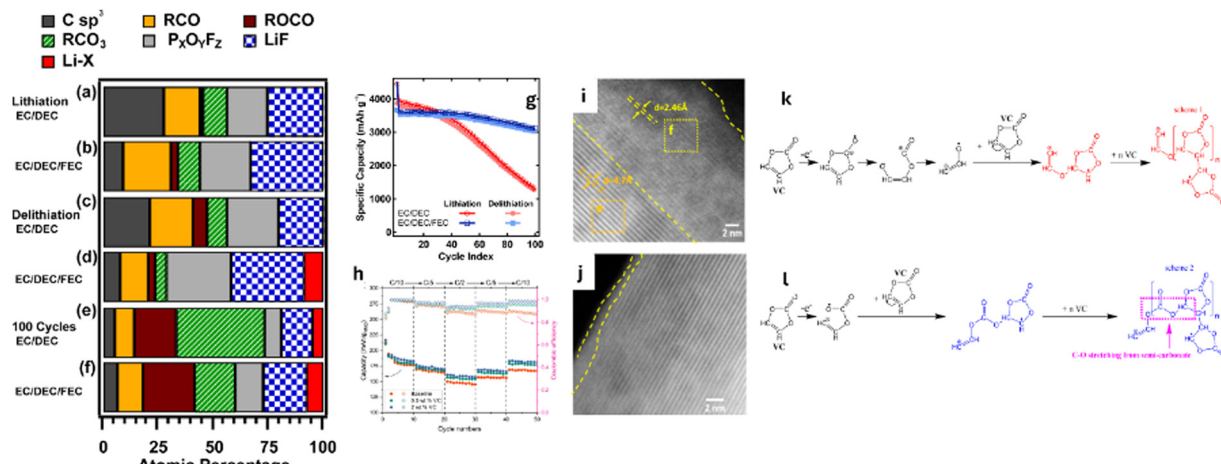


**Fig. 22** Relative composition of the 10 nm SEI layer formed on an amorphous Si anode after: (a) first lithiation cycle in EC/DEC, (b) first lithiation cycle in EC/DEC/FEC, (c) first delithiation cycle in EC/DEC, (d) first delithiation cycle in EC/DEC/FEC, (e) 100 cycles in EC/DEC, and (f) 100 cycles in EC/DEC/FEC. Reproduced with permission from ref. 338. Copyright 2015 American Chemical Society. (g) 100 cycle performance of amorphous Si||Li cell. Reproduced with permission from ref. 338. Copyright 2015 American Chemical Society. (h) Rate capability performance of NCM811||Li half cells cycled in baseline (1 M LiPF<sub>6</sub> in EC : DEC (50 : 50 v/v)), and baseline electrolytes with 0.5 and 2 wt% VC, respectively. Reproduced under the terms of the Creative Commons CC-BY 4.0 license.<sup>339</sup> Copyright 2024, The Authors. HAADF-STEM images of NCM811 after 100 cycles in (i) baseline electrolyte, and (j) Baseline + 2 wt% VC. (k) and (l) VC oxidation and polymerization pathways that allow the formation of stable CEI. Reproduced under the terms of the Creative Commons CC-BY 4.0 license.<sup>339</sup> Copyright 2024 The Authors.

degradation mechanisms of Si-anodes that result in catastrophic cell failures.

FEC has also demonstrated its effectiveness as additive for high voltage operations.<sup>275</sup> Zou *et al.*<sup>340</sup> investigated the impact of FEC in a fluorinated ester-based electrolyte, designed to enhance cycling stability and power capability under extreme temperature conditions, fast charging, and high voltage. Their study revealed that FEC improved the electrolyte stability, oxidation resistance, and Li<sup>+</sup> solvation dynamics, thereby enhancing the performance of NCM 811||Gr cells at > 4.3 V. The addition of FEC into the MDFA/PFPN/FEC electrolyte resulted in significantly improved initial CE (87.0%) and long-term cycling stability, with an 85.2% capacity retention after 200 cycles and 80.3% after 500 cycles.

In contrast, electrolytes lacking FEC exhibited rapid degradation, with significantly lower capacity retention. Hwang *et al.*<sup>341</sup> showed that while FEC facilitates the *in situ* formation of a mechanically stable, electrically conductive, and elastic SEI layer, when combined with other additives, such as LiDFOB, and an *ex situ* LiNO<sub>3</sub> anode treatment, which promotes Li<sub>2</sub>O formation in the SEI, better performance is attainable. Their study paired an Al-doped FCG Li[Ni<sub>0.75</sub>Co<sub>0.10</sub>Mn<sub>0.15</sub>]O<sub>2</sub> cathode with the modified electrolyte/anode and reported an unprecedented high areal capacity of 4.1 mA h cm<sup>-2</sup> and 80% capacity retention after 300 cycles at a current density of 3.6 mA cm<sup>-2</sup>. Moreover, pouch-type cells assembled using the modification approach retained 90% of their initial capacity over 500 cycles at a high current density of 1.8 mA cm<sup>-2</sup>, highlighting the practicality of this approach.

Vinylene carbonate (VC) is another additive that enhances the stability of the cathode electrolyte interface (CEI). VC undergoes oxidation at the cathode electrode at potentials

lower than other carbonate solvents, resulting in the formation of insoluble products that contribute to the stability of the CEI, particularly at high voltages, by forming a polymeric protective layer that suppresses electrolyte decomposition at elevated temperatures.<sup>339</sup> Dai *et al.* proposed that a uniform and cohesive CEI could protect the cathode by preventing transition metal mixing, dissolution, and surface construction at voltages up to 4.8 V.<sup>339</sup> They suggested that VC oxidizes and initiates a polymerization process that forms a cohesive polymeric layer on the cathode (Fig. 22k). The protective polymeric layer inhibits the detrimental rock-salt-like phase that forms on NCM cathode surfaces along with a dense, uniform CEI that suppresses electrolyte decomposition, reducing the likelihood of suitable environments for thermal runaway events (Fig. 22h–j).

Flame retardant additives, often containing organic halogens, phosphorus, and phosphazene compounds, help mitigate the risk of thermal runaway.<sup>342</sup> Among these, organic phosphorus compounds, such as trimethyl phosphate (TMP), triethyl phosphate (TEP), triphenyl phosphate (TPP), and dimethyl methyl phosphonate (DMMP) are the most commonly used due to their high efficiency, low toxicity, and low cost.

Typically, when the temperature within a LIB cell increases, these additives decompose, forming free radicals that replace hydrogen and hydroxy free radicals formed from electrolyte decomposition/combustion, leading to the termination of the combustion reaction.<sup>343</sup> Dong *et al.*<sup>344</sup> demonstrated a fire-retardant electrolyte consisting of 2.8 M LiTFSI in TEP with 10% FEC. The electrolyte composition demonstrated good thermal stability, with peak heat release rates (PHRR) elevated to 290 °C and negligible volatility below 150 °C, compared to conventional carbonate electrolytes with PHRR around 190 °C



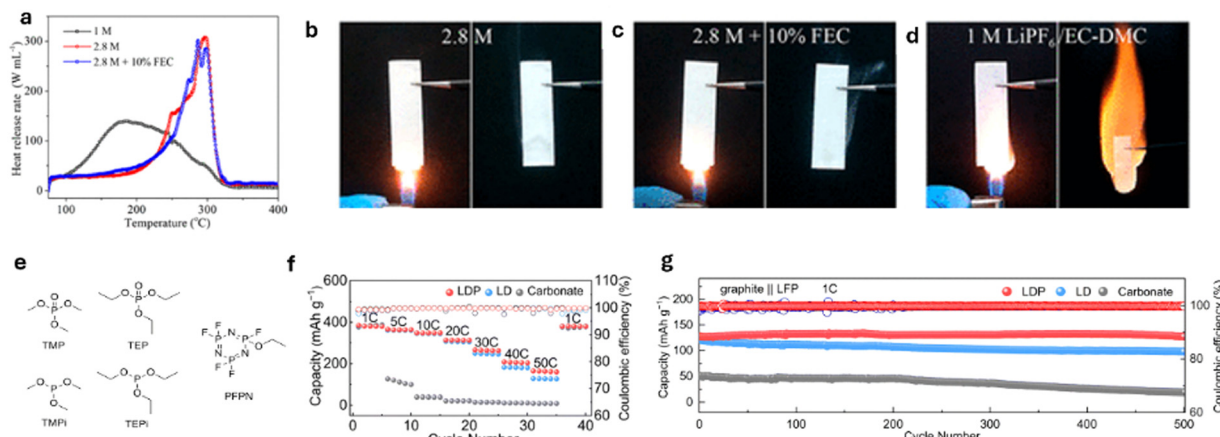


**Fig. 23** (a) Heat release profiles of TEP-based electrolytes (1 M LiTFSI in TEP, 2.8 M LiTFSI in TEP, and 2.8 M LiTFSI in TEP + 10 vol% FEC) obtained by microscale combustion calorimeter. Reproduced with permission from ref. 344. Copyright 2019, American Chemical Society. Photographs of ignition tests of glass fiber strips saturated with (b) 2.8 M LiTFSI electrolyte, (c) 2.8 M LiTFSI + 10 vol% FEC electrolyte, and (d) 1 M LiPF<sub>6</sub> in EC:DMC (1:1, v/v). Reproduced with permission from ref. 344. Copyright 2019, American Chemical Society. (e) Structures of common flame retardant additives. Reproduced with permission from ref. 345. Copyright 2024, The Authors. (f) Rate performance of LFP||Li cells cycled in 1 M LiTFSI in DOL:PFPN (9:1, v/v) (LDP), 1 M LiTFSI in DOL (LD) and 1 M LiPF<sub>6</sub> in DMC:EC (7:3, v/v) (carbonate electrolyte). Reproduced with permission from ref. 346. Copyright 2024, The Royal Society of Chemistry. (g) Long-term cycling performance of LFP||Gr cells cycled in LDP, DL, and carbonate electrolytes at 1C. Reproduced with permission from ref. 346. Copyright 2024, The Royal Society of Chemistry.

(Fig. 23a). The electrolyte was considerably nonflammable (Fig. 23b-d) and formed a stable LiF-rich SEI, leading to the high performance of dendrite-free Li||LFP cells that retained 90% of their capacity over 2000 cycles at 1C. Its effectiveness was shown in high-voltage cathodes (NCM811), with a 95.7% capacity retention after 100 cycles.

Although effective, these phosphate-based additives suffer from poor reduction stability, especially when in contact with the graphite anode. To balance the flame-retarding effect and electrochemical performance of LIB electrolytes, cyclophosphazenes are an emerging category of flame-retardant additives. Cyclophosphazenes have ring structures consisting of alternating nitrogen and phosphorus atoms (Fig. 23e).<sup>347</sup> The phosphorus molecules act as radical scavengers and promote char formation to enhance thermal insulation.<sup>347</sup> The nitrogen molecules release non-combustible gases, such as NH<sub>3</sub> and N<sub>2</sub>, further suppressing combustion. Liu *et al.*<sup>345</sup> showed that adding 3 wt% ethoxy (pentafluoro) cyclotriphosphazene (PFPN) to a base electrolyte of 1 M LiTFSI in EC (1:1) significantly improved the electrolyte's flame retardancy, reducing the self-extinguishing time to 10 s g<sup>-1</sup>. The PFPN electrolyte also showed better compatibility with graphite cells, resulting in a 97.25% capacity retention after 100 cycles. Under fast charge conditions, the addition of PFPN to a 1 M LiTFSI-based electrolyte in 1,3-dioxolane significantly improved both ionic conductivity and the formation of a stable, highly conductive SEI to enable superior fast-charging performance.<sup>346</sup> PFPN not only enhanced the non-flammability of the electrolyte but also mitigated the corrosion of Al foil triggered by the LiTFSI salt. Under extremely fast charge conditions, Li||Gr cells delivered high reversible capacities of 314.2 mA h g<sup>-1</sup> at 20C and 164.4 mA h g<sup>-1</sup> at 50C (Fig. 23f). Additionally, LFP||Gr pouch

cells with an N/P ratio of 1.4 delivered an initial capacity of 127.9 mA h g<sup>-1</sup> and maintained 127.5 mA h g<sup>-1</sup> after 500 cycles (Fig. 23g).

**ii. Solid electrolytes.** Solid electrolytes present another significant advancement for enhancing the safety of LIBs. By replacing volatile and flammable liquid organic solvents with non-flammable solid-state materials, the adverse effects of these solvents are curbed. Moreover, eliminating liquid containment also simplifies cell design and mitigates safety risks, such as electrolyte leakage and thermal runaway, which are common in liquid electrolyte systems. The wider electrochemical stability window of certain solid electrolytes (up to 7 V)<sup>348</sup> and their temperature stability enable the application of high-voltage cathode materials and operation in a wider temperature range.<sup>349</sup>

Generally, two classes of materials are used as solid electrolytes in LIBs—inorganic ceramics and organic polymers,<sup>347</sup> with hybrid ceramic–polymer-type solid electrolytes emerging recently.<sup>349</sup> Inorganic ceramics are recognized for their solid-state ionic conductivity translating into high ionic conductivities exceeding the order of 10<sup>-2</sup> S cm<sup>-1</sup>,<sup>350</sup> particularly at elevated temperatures, and their mechanical stability. Some widely studied ceramic materials include halides, sulfides, garnets, and perovskites, such as Li<sub>3</sub>N, La<sub>0.5</sub>Li<sub>0.5</sub>TiO<sub>3</sub>, La<sub>3.25</sub>Ge<sub>0.25</sub>P<sub>0.75</sub>S<sub>4</sub>, Li<sub>7</sub>La<sub>3</sub>Zr<sub>2</sub>O<sub>12</sub>, Li<sub>10</sub>GeP<sub>2</sub>S<sub>12</sub>, Li<sub>10</sub>SnP<sub>2</sub>S<sub>12</sub>.<sup>350</sup> Owing to the robust mechanical properties (high Young's modulus) of solid-state electrolytes, internal short-circuiting resulting from dendritic growth is suppressed,<sup>349</sup> allowing better pairing of these electrolytes with Li metal anodes for higher energy densities. However, these materials are susceptible to oxidative instability and electronic percolation because of their high electronic conductivity, especially at high current

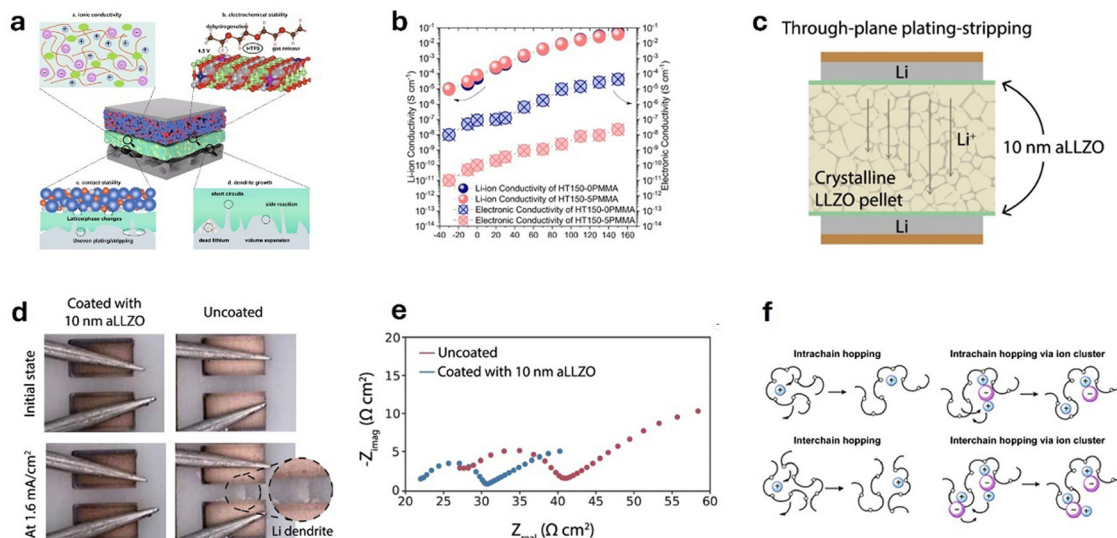


**Fig. 24** (a) Key issues new GPE approaches should mitigate. Reproduced with permission from ref. 352. Copyright 2023, The Authors. Photographs of ignition tests of glass fiber strips saturated with (b)  $\text{Li}^+$  and electronic conductivities of PMMA absent  $\text{LiBH}_4$  electrolyte (HT150-0PMMA) and 5% PMMA present  $\text{LiBH}_4$  electrolyte (HT150-5PMMA). Reproduced with permission from ref. 353. Copyright 2023, The Royal Society of Chemistry. (c) Schematic of the through-plane Li/aLLZO/LLZO/aLLZO/Li configuration employed. Reproduced with permission from ref. 354. Copyright 2021, The Authors. (d) Optical images of the LLZO pellet surface on the uncoated and aLLZO-coated side at the beginning of the plating-stripping process and after reaching a current density of  $1.6 \text{ mA cm}^{-2}$ . Magnified image shows a Li filament short-circuiting the Li contacts in the uncoated side of the pellet. Reproduced with permission from ref. 354. Copyright 2021, The Authors. (e) Nyquist plot of the impedance response of the uncoated and aLLZO-coated LLZO pellets. Reproduced with permission from ref. 354. Copyright 2021, The Authors. (f) Schematic of  $\text{Li}^+$  diffusion through polar groups and segment movement of polymer chains in composite polymer electrolytes. Reproduced with permission from ref. 352. Copyright 2023, The Authors.

densities, which can still lead to dendrite formation.<sup>351</sup> Hence, modifying the electrolyte structure to withstand dendrite formation and suppress electronic conductivity while maintaining high ionic conductivity is crucial to ensure the full adoption of solid electrolytes (Fig. 24a).

To address this, Wei *et al.*<sup>353</sup> explored an *in situ* melting reaction between lithium borohydride ( $\text{LiBH}_4$ ) and polymethyl methacrylate (PMMA). They observed that forming a covalently bonded coordination layer on the surface of the solid electrolyte particles *via* the *in situ* melting reaction blocks electronic percolation pathways by “locking” excess electrons in place (Fig. 24b), extends the oxidative stability of the electrolyte to suppress dendrite growth.

The coordination layer acted as a binder that strengthened the mechanical properties of the solid electrolyte, enabling it to withstand the stress and strain during Li plating/stripping. Additionally, the *in situ* modification extended the voltage window of the electrolyte to 10 V, offering unprecedented cycling stability for high-voltage applications. Sastre *et al.*<sup>354</sup> proposed using amorphous Li-La-Zr-O (aLLZO) as a solution to Li dendrite formation in solid-state batteries (Fig. 24c). Unlike the crystalline version, the amorphous phase eliminates grain boundaries, which are common pathways for dendrites. The ultrathin 10 nm aLLZO films effectively blocked dendrite growth, allowing the battery to operate at current densities of up to  $3.2 \text{ mA cm}^{-2}$  with reduced impedance (Fig. 24d and e).

Organic polymers, particularly poly(ethylene oxide) (PEO), are another category of favorable materials for solid electrolytes because of their flexibility, lower cost, and easier processability

compared to inorganic ceramics. Unlike gel polymer electrolytes with solvents confined in a polymer matrix, in solvent-free solid polymer electrolytes, Li salts are solvated by polymer chains. Compared with traditional liquid electrolytes, solid polymer electrolytes not only alleviate the danger of flammability and detrimental side reactions of the electrolyte with electrodes but also retain excellent adhesion and film-forming properties of polymers. However, while organic polymer electrolytes, such as the PEO-based electrolytes, exhibit good compatibility with Li salts and can stabilize the Li metal interface, their low ionic conductivity at room temperature remains a challenge, often requiring higher operating temperatures.

To overcome these limitations, hybrid solid electrolytes, which combine ceramic and polymer materials, have emerged as a promising solution to balance the benefits of both systems. Ceramic-polymer composite electrolytes offer high ionic conductivity along with the flexibility and processability of polymers. They are formed by adding ceramic fillers into polymeric solid electrolytes.<sup>352</sup> Moreover,  $\text{Li}^+$  diffusion in this class of electrolyte is due to the polar groups and segment movement of polymer chains (Fig. 24f). Ceramic fillers like  $\text{Li}_2\text{La}_3\text{Zr}_2\text{O}_{12}$  and  $\text{Al}_2\text{O}_3$  act not only as ion conductors but also as structural reinforcements that prevent polymer crystallization, a major factor limiting the ionic mobility of pure polymer electrolytes.<sup>352</sup> These fillers also create continuous ion-conducting pathways while increasing the electrolyte's shear modulus, effectively suppressing Li dendrite growth.<sup>293</sup> The fillers' ability to interact with  $\text{Li}^+$  and prevent undesirable reactions with the anode or cathode extends the



electrochemical stability window, making these hybrid electrolytes compatible with high-voltage layered oxide cathodes. Additionally, the ceramic particles improve the thermal stability of the electrolyte to reduce the risk of thermal runaway, especially under high-temperature operating conditions.<sup>352</sup> By enhancing both the mechanical and electrochemical properties, hybrid polymer-ceramic electrolytes address the inherent weaknesses of liquid and polymer-only systems, thus significantly boosting the overall safety and performance of LIBs.

**iii. Aqueous electrolytes.** Aqueous rechargeable metal batteries were introduced by Li *et al.* in 1994.<sup>355</sup> Aqueous electrolytes offer potential solutions to safety concerns in LIBs, particularly when compared to their organic carbonate-based counterparts, which are prone to flammability and thermal runaway. Due to the absence of volatile organic compounds, aqueous electrolytes are inherently non-flammable, reducing the risk of fires and explosions that occur due to short-circuiting. This makes aqueous electrolytes especially attractive for large-scale or stationary energy storage applications. However, traditional aqueous systems are limited by their narrow electrochemical stability window (ESW) of 1.23 V.<sup>356</sup> Beyond this ESW, H<sub>2</sub> evolution, occurring between 2.21 to 3.04 V *vs.* Li, coupled with O<sub>2</sub> evolution deteriorates electrode structures. These side reactions limit the choice of electrode materials compatible with the ESW of aqueous electrolytes.

Adjusting the electrolyte's alkalinity is a common approach to widening the ESW. While this suppresses hydrogen evolution, it compromises anodic stability against oxygen evolution, resulting in high self-discharge rates.<sup>356,357</sup> To address this limitation and widen the ESW of aqueous electrolytes whilst maintaining the safety aspects of aqueous electrolytes, the “water-in-salt” electrolyte (WiSE) concept has been developed. WiSE refers to aqueous electrolytes where the concentration of salt in water exceeds 5 M. In these systems, the salt molecules

outnumber those of the solvent by both weight and volume,<sup>357</sup> resulting in super-concentrated aqueous electrolytes. The enlargement of ESW offered by WiSE has been ascribed to the modification of the Li<sup>+</sup> solvation sheaths (Fig. 25a), allowing a preferential decomposition of salt anions that form stable SEIs on the anode interface. Unlike non-aqueous electrolyte systems where SEI layers form and protect the electrodes, traditional aqueous electrolyte systems lack decomposition products capable of forming dense, stable interphases on the electrodes. This makes the WiSE approach promising, especially from a safety perspective.

The most frequently studied WiSE systems are based on one Li salt, typically bis(trifluoromethane sulfonyl)imide (LiTFSI) or TFSI-derived salts because of their high solubility in water, ability to form fluorine-rich SEIs, and stability and lesser likelihood to undergo hydrolysis to form harmful byproducts, such as HF, compared to LiPF<sub>6</sub>. In 2015, Suo *et al.*<sup>357</sup> demonstrated the suitability of WiSE using a LiTFSI-based electrolyte with molality  $>n$ . This allowed the formation of a SEI-beneficial anion-containing Li<sup>+</sup> solvation sheath, causing the formation of a stable, passivating interphase on a Mo<sub>6</sub>S<sub>8</sub> anode interface (Fig. 25c and d). The highly concentrated salt provided an ESW of  $\sim 3$  V (Fig. 25b), and the fully aqueous LiMn<sub>2</sub>O<sub>4</sub>||Mo<sub>6</sub>S<sub>8</sub> cell demonstrated high CEs for up to 1000 cycles at both low (0.15C) and high (4.5C) rates with a cell voltage of 2.3 V. This significant increase in the ESW allows more cathode and anode materials to be applied to aqueous LIBs, offering improved performance without sacrificing the inherent safety benefits of aqueous electrolytes.

Despite the promises of WiSe, limitations still exist. Drouget *et al.*<sup>359</sup> demonstrated the instability of the SEI formed at the anode in this electrolyte system. They showed that the SEI in WiSE is not protective enough to prevent continuous parasitic reactions, such as water reduction and hydrogen evolution. For

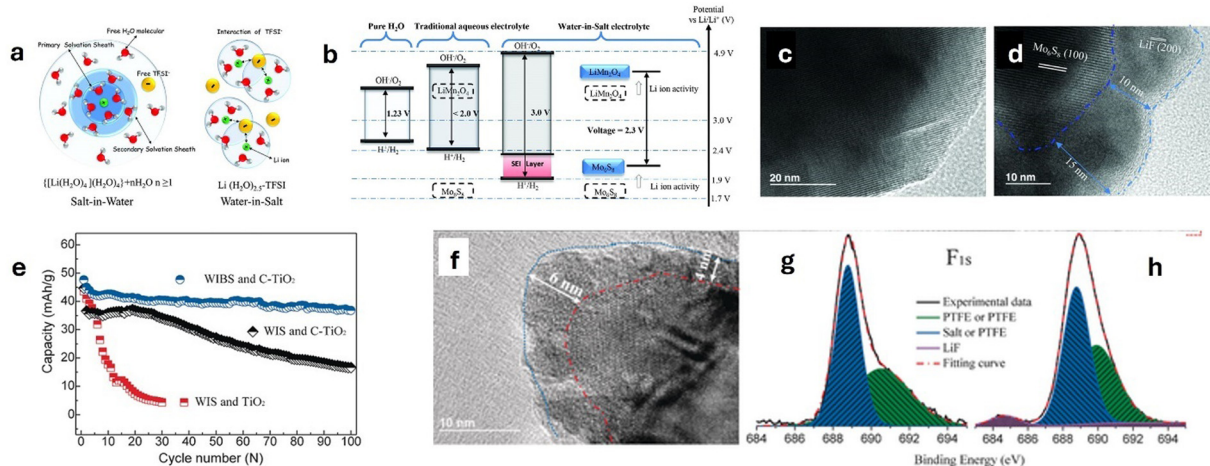


**Fig. 25** Performance of WiSE Reproduced with permission from ref. 357. Copyright 2015, American Association for Advancement of Science: (a) illustration of the evolution of the Li<sup>+</sup> primary solvation sheath in diluted vs. water-in-salt solutions, (b) illustration of expanded electrochemical stability window for water-in-salt electrolytes paired with LiMn<sub>2</sub>O<sub>4</sub> cathode and Mo<sub>6</sub>S<sub>8</sub> anode, (b) TEM images of pristine Mo<sub>6</sub>S<sub>8</sub> (c) and cycled Mo<sub>6</sub>S<sub>8</sub> (d) in WiSE electrolyte. Performance of WIBS electrolytes. Reproduced with permission from ref. 358. Copyright 2016, Wiley-VCH: (e) cycling stability of LiMn<sub>2</sub>O<sub>4</sub>||c-TiO<sub>2</sub>/TiO<sub>2</sub> anodes in 12 M LiTFSI in water (WIS) and 21 M LiTFSI + 7 M LiOTf (WIBS) electrolytes, (f) TEM images of C-TiO<sub>2</sub> recovered after 143 cycles in WIBS at 1C, (g) and (h) XPS of C-TiO<sub>2</sub> anode before and after 10 cycles at 0.5C, respectively in WIBS electrolyte.



instance, when a  $\text{Mo}_6\text{S}_8\text{||LFP}$  system was cycled with WiSE, significant gas evolution and capacity loss were observed. This was attributed to the SEI's inability to fully block hydrogen evolution, limiting the long-term cycling and thermal stability of WiSE-based systems. Moreover, the high concentration of LiTFSI used in WiSE is close to the saturation point of the salt at room temperature, indicating that further salt concentration cannot improve SEI.

To address the underlying issues of WiSE, super concentrated electrolytes using either two Li-based salts or one Li-based and one non-Li-based salt, called Water-in-Bisalt (WiBS), are also gaining momentum in aqueous electrolytes research. Greater salt concentrations are possible in WiBS systems due to the solubility of Li-based salts being increased by asymmetric ions. Since a hydrated salt, considered a saturated electrolyte, can dissolve another un-hydrated salt with similar chemical properties, it is possible to form mixed salt systems with higher cation/water ratios. Based on this, Suo *et al.*<sup>358</sup> utilized a 21 M LiTFSI-based WiSE to dissolve lithium trifluoromethane sulphonate (LiOTf), resulting in a WiBS consisting of 21 M LiTFSI and 7 M LiOTf that offered better electrochemical performance (Fig. 25e) and formed a more efficient SEI (Fig. 25f-h). Additionally, bisalt electrolytes further reduce the electrochemical activity of water, reducing its likelihood for gas evolution, while depressing the liquidus temperature of the electrolyte.<sup>358</sup>

While WiSE and WiBS approaches demonstrate significant promises for enhancing the safety of aqueous LIBS, further research that focuses on the SEI stability in aqueous electrolyte systems is paramount to harness the full safety benefits of these electrolyte systems.

#### d. Cell level thermal runaway mitigation strategies

There are two main categories of thermal runaway mitigation strategies reported in the literature, namely the prevention in a cell and suppression of propagation across multiple cells. Kong *et al.*<sup>360</sup> suggest various methods, like thermally responsive materials and the implementation of real-time monitoring systems. A study by Lai *et al.*<sup>361</sup> investigated the effect of introducing a poison agent ( $\text{Al}_2(\text{SO}_4)_3 \cdot 16\text{H}_2\text{O}$ ) in high-energy batteries. They found that the maximum thermal runaway temperature can be reduced by more than 300 °C due to a new reaction sequence regulation. Two poisoning mechanisms were identified that revealed how the poison agent worked. The hydrate could react with  $\text{LiPF}_6$  and EC to hinder further exothermic reactions that relate to EC and the hydrate could poison the lithiated graphite and prevent the redox reaction between the cathode and the anode. It was noted that due to the significant reduction in the maximum temperature by the self-poisoning design of the system, more work needed to be conducted to test the feasibility of the toxic agent for practical applications.

Friesen *et al.*<sup>362</sup> investigated the safety behavior after thermal and mechanical abuse of 18650 Li-ion cells with  $\text{Al}_2\text{O}_3$  coating on the anode surface and their aging at low temperatures. Post-mortem analysis showed a thick, irreversibly deposited Li metal layer beneath a mostly intact  $\text{Al}_2\text{O}_3$  coating on the

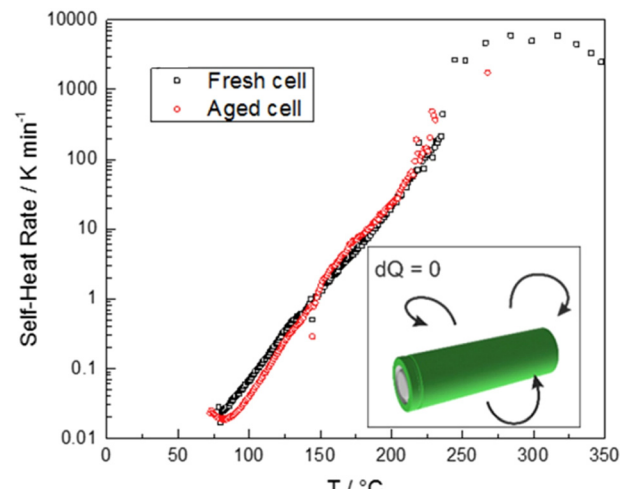


Fig. 26 Thermal abuse ARC experiments under quasi-adiabatic conditions. Reproduced with permission from ref. 362. Copyright 2017, Elsevier B.V.

negative electrode. Safety tests in an open system confirmed that the coating remained effective despite Li deposition, ensuring a safe response for both fresh and aged cells. Under quasi-adiabatic conditions, aged cells exhibited increased reactivity, but both fresh and aged cells showed similar responses to thermal abuse (Fig. 26).

Naguib *et al.*<sup>363</sup> developed a battery system with breakable electrodes for mitigating abuse by electrically isolating the internally shorted part of the battery from the rest of the cell before the separator is punctured. It was found that thermal runaway could be prevented by limiting the current passing through the shorted area. Likewise, FEM simulations were performed to identify the level of separation needed. The breakable electrodes were realized by introducing a certain slit pattern using a modified clicker die without affecting the conventional roll-to-roll production for battery electrodes. Batteries with slotted electrodes exhibited capacities and voltage profiles similar to those of standard batteries. When mechanically abused by heavy deformation, the modified battery did not short-circuit, while the standard one shorted and became nonfunctional. The modified battery was found to retain 93% of its capacity after the mechanical abuse test and was electrochemically viable.

Ji *et al.*<sup>364</sup> developed a thermal shutdown separator with a shutdown temperature of 90 °C by coating thermoplastic ethylene-vinyl acetate copolymer (EVA) microspheres onto a conventional polyolefin membrane film and tested for thermal protection. The experimental results demonstrated that owing to the melting of the EVA coating layer at a critical temperature, this separator could promptly cut off the  $\text{Li}^+$  transport between the electrodes and thus shut down the battery reactions to protect the cell. In addition, this type of separator had no negative impact on the normal battery performance, therefore providing an internal and self-protecting mechanism. Shi *et al.*<sup>365</sup> investigated alkanes (octane, pentadecane, and icosane) as thermal-runaway retardants. In nail penetration tests

on coin cells, 4 wt% pentadecane reduced the maximum temperature by 60%. Similarly, in the impact test on pouch cells, 5 wt% pentadecane reduced the maximum temperature by 90%. The high mitigation effectiveness of pentadecane is attributed to its high wettability of the separator and its immiscibility with electrolyte. By forming a physical barrier between the cathode and anode, pentadecane interrupted  $\text{Li}^+$  transport and increased the charge transfer resistance by nearly two orders of magnitude. The diffusion rate of pentadecane in the electrode layer stack was measured to be  $580 \mu\text{m s}^{-1}$ .

Wen *et al.*<sup>366</sup> investigated the effects of oxygen levels and dilution gases on thermal runaway propagation. They used a combustion chamber for pressure and gas control and analyzed the internal changes like electrode structure degradation, droplet formation, and decomposition of electrolyte and binder using X-ray computed tomography. They found that reduced oxygen concentration leads to decreased mass loss, weakening the progression and decreasing the heat and gas production, which leads to less structural degradation. It was observed that oxygen concentration control and inert gas diffusion were effective strategies for battery fire safety and thermal management. Another mitigation strategy is the introduction of hollow gas microspheres plates as thermal barriers. Niu *et al.*<sup>367</sup> found that increasing the hollow gas microspheres plates decreased the propagation rate. Thermal runaway can be triggered in adjacent cells within a 3 mm distance, so mini channel cooling has also been studied by Xu *et al.*<sup>368</sup> This method can prevent propagation, but it is not effective in stopping runaway in a single cell. On the other hand, Hu *et al.*<sup>369</sup> proposed the use of water mist, which could significantly reduce the maximum battery temperature and decrease the likelihood of thermal runaway. It also explores the use of phase change material and composites.

Xu *et al.*<sup>370</sup> tested three different extinguishing agents, including  $\text{CO}_2$ , HFC-227ea, and water mist on the fire and their extinguishing properties on NCM/graphite cells. The NCM/graphite cells produced black smoke and violent jet fire, necessitating effective suppression measures to prevent fire propagation and ignition of battery materials. Among the tested extinguishing agents, only water mist effectively suppressed the fires. The cooling effects of these agents vary, with

water mist providing the most significant temperature reduction, followed by HFC-227ea, which is slightly more effective than  $\text{CO}_2$ . Temperature measurements before agent depletion show that water mist reduces peak average temperatures by up to  $133^\circ\text{C}$ , significantly more than the other agents. Zhang *et al.*<sup>371</sup> established a coupled electrochemical-thermal simulation model of thermal runaway propagation to supplement experimental data and public datasets for model training and verification. Multi-mode and multi-task thermal propagation forecasting neural network was established for advanced multi-step prediction along with a temperature-based propagation grading warning strategy. The validation of the simulation model involved experiments on single battery cells and battery modules. Single-cell tests were conducted in an ARC to precisely measure temperature changes, while module tests were performed on a specialized platform simulating real-world conditions.

## 5. Operational considerations: temperature and mechanical factors

One critical environmental condition that LIBs need to adapt to is a wide range of temperatures. With the advent of a thermal management system at relatively moderate temperatures, it is often necessary to account for their storage and start-up under extreme operating conditions.<sup>372</sup> Applications such as space, deep-sea exploration, and military use, require optimal performance across extremely broad temperature ranges.<sup>373–375</sup> Operating LIBs at such temperatures will often lead to significant changes in the ion diffusion kinetics and  $\text{Li}^+$  migration within the SEI layer.<sup>373,376</sup> To address these challenges, significant efforts have been made to explore the thermodynamics and kinetics of anodes, cathodes, electrolytes, and additives, with the aim of enhancing the performance.<sup>377,378</sup> A summary of the key operational considerations is shown in Fig. 27a.

For the operation at subzero temperatures, electrochemical reactions are expected to become kinetically sluggish compared to standard temperatures, leading to a significant decrease in electrolyte conductivity and diffusion coefficients. Furthermore, a significant increase in viscosity at these temperatures

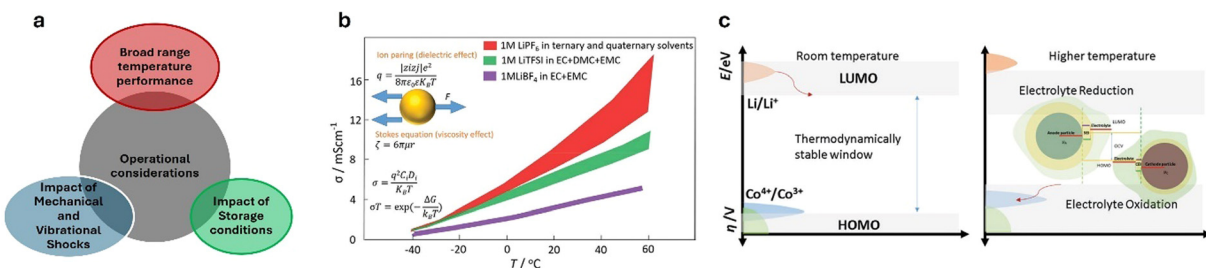


Fig. 27 (a) Schematic of key operational considerations for practical LIBs. (b) Conductivities of three Li salts in various electrolytes versus temperature. Data extracted from Jet Propulsion Laboratory reported studies and (c) electron energy levels and electrode potential correlated with the HOMO/LUMO levels of the electrolyte governing thermodynamic stability with increasing temperature, and insets showing the SEI and CEI formed on the anode and cathode particle surfaces. Reproduced with permission from ref. 379. Copyright 2020, Wiley-VCH.



can cause the electrolyte to freeze, potentially leading to open circuits.<sup>380</sup> Therefore, it is desirable to find an electrolyte with high conductivity and a low freezing point to avoid ohmic polarization induced by the reduced diffusion coefficient. The Jet Propulsion Laboratory showed the ternary mixture of ethylene carbonate (EC), diethyl carbonate (DEC), and dimethyl carbonate (DMC) yielded approximately  $1 \text{ mS cm}^{-1}$ , which is higher at  $-40^\circ\text{C}$  (Fig. 27b) compared to other combinations, facilitating Li intercalation–deintercalation processes.<sup>381</sup> Aliphatic esters and ethers such as 1,2-dimethoxyethane (DME), have been included to design the new solvent mixtures to lower the viscosity and freezing points of electrolyte solutions.<sup>382,383</sup> In addition to having high ionic conductivity, it is also crucial for the electrolyte solution to have the ability to form a stable SEI on the anode electrode. The ability to form a stable SEI for the electrolyte solution including ester mixture was found to be lowest for low molecular weight esters and this enhanced as the polymer chain length increased.<sup>384,385</sup>

In contrast, different challenges must be met when operating LIBs at high temperatures. Even though the enhancement in solid/liquid diffusivity can be seen, the thermodynamics and kinetics of both SEI and CEI layers are significantly modified at high temperatures near  $40^\circ\text{C}$ .<sup>379,386,387</sup> Shifting of the highest occupied molecular orbit (HOMO) and lowest unoccupied molecular orbit (LUMO) yields a narrower energy gap between them, rendering the SEI and CEI unstable at higher temperatures (Fig. 27c). Electrolytes with low volatility are desirable to minimize the loss of liquid electrolyte in solution. Vapor pressure is often used to assess the thermal stability and safety of electrolytes for the design of LIBs.<sup>388</sup> Due to the instability of LiFP<sub>6</sub> at high temperatures, various new salts, including a Li salt based on a chelated borate anion (LiBOB), were studied for the formation of stable SEI.<sup>389</sup> These new types of salts demonstrated similar battery capacity with LiFP<sub>6</sub>, but with improved capacity retention at  $60^\circ\text{C}$ . Another challenge with high-temperature operations will be understanding the complex interfaces at the anode and cathode, including how the lithiated anode and delithiated cathode interact directly with the electrolyte and its degraded products through the SEI/CEI layers.<sup>390–392</sup>

When installing LIBs in new locations within a military vehicle, it is essential to consider both the temperature conditions and the mounting method.<sup>393</sup> To ensure reliable performance and extend battery life, batteries should be protected from extreme temperatures and securely mounted to minimize vibration. Mounting batteries outside the engine bay can help manage battery temperature more effectively. However, if the distance from the alternator or starter motor is increased, longer electrical cables will be required, leading to greater electrical losses and reduced system efficiency. Additionally, if LIBs are installed in the passenger or operator compartment, appropriate measures must be taken to safely vent potentially harmful gases.

Understanding the effects of mechanical shocks and vibrations on battery performance in extreme operational environments is another crucial aspect to consider for the LIB system.

The battery pack structure can be compromised when exposed to vibration and shock conditions, and electrical connection within the pack can be unstable during vehicle movements.<sup>394,395</sup> Hooper *et al.* explored the degradation of cell materials caused by vibrations, using 18650 oxide-based battery cells.<sup>396,397</sup> The direct current resistance of the oxide-based cells increases drastically when subjected to a vibration cycle representative of a 10-year vehicle life. Somerville *et al.* also demonstrated that surface films on battery cells formed due to vibrations contribute towards increased cell degradation, capacity loss, and higher cell impedance.<sup>398</sup> Overall, understanding the correlation between vibrations and degraded battery performance is essential for ensuring the safety and optimal performance of LIBs.

## 6. Battery use in military operational settings

The operational considerations discussed regarding vibrations, shocks, and operation of LIBs in widely varying temperature environments are particularly concerning for military, first responder, and space operations that routinely use these batteries for energy storage. Since military and first responder operations are often characterized by extreme environments, additional design considerations for LIBs must be applied. The physical design of the internal battery components is important from a reliability standpoint. Rough handling of the battery when installed or transported in vehicles designed for rough terrain has been shown to adversely impact battery performance through degradation of internal connections. Changes in internal battery connections resulting in either short circuiting or large resistances can lead to thermal runaway or large voltage drops respectively.<sup>399</sup>

Military operations often occur in extreme environments; desert heat to arctic cold, with wide ranges in humidity, and LIBs are often used in communications and optical equipment inherent to these operations. First responders, particularly firefighters, often operate in high-temperature environments. For safe operation of battery-powered equipment, the batteries must be able to maintain operation in these environments.<sup>400</sup> Additionally, the batteries must be stable and maintain functionality over long periods of non-use, such as prolonged shelf-life in long-term storage. Military organizations often procure equipment in large quantities and store it for future use. The storage facilities for equipment may not be climate controlled, and storing batteries for long periods of time at high ambient temperatures can lead to significant decreases in battery life. A study on the degradation of LIBs due to long-term storage (two months) in temperature-controlled laboratory conditions led to a 3% drop in useful capacity.<sup>399</sup>

When worn on the body of military personnel, LIBs may be damaged due to ballistic impacts. While it may be of secondary importance relative to the impacts on personnel, the damage sustained by the battery may increase the danger to military personnel through violent exothermic reactions that could



result in severe burns. The significance of safety issues inherent in ballistic impacts to battery casings was highlighted in a study focused on evaluating the feasibility of using LIB as supplemental body armor.<sup>401</sup> This study used standard 7.62 × 39 mm ammunition fired at battery packs in combination with body armor used by current military forces. In this experiment, battery packs were mounted either in front of the body armor, or behind, and the ballistic protection afforded by the battery pack and the resulting damage to the battery was examined. In all tests, the batteries were crushed and perforated, and in the tests with partially charged batteries, the temperature of the battery pack rose to over 100 °C within 2 minutes of impact.<sup>401</sup> These results lead to increased risk of burns and toxic fume inhalation by personnel.

Non-ballistic damage to LIBs can still result in the same safety issues due to short circuiting because of crushing or penetration of the battery housing. Mechanical failures can often arise during military operations that include transportation over rough terrain, equipment or personnel drops from aircraft, and equipment handling operations by heavy equipment or large numbers of personnel. Often battery failure due to these operations is a result of puncture or deformation of the battery case. Puncture tests on batteries have shown that foreign objects penetrating the battery case often result in a short circuit within the battery, leading to undesired side reactions and thermal runaway.<sup>402</sup>

Battery performance requirements for technology applications used by first responders and emergency personnel are based on reliability, safety, and longevity. These same requirements are essential for military applications. Programs such as the System Assessment and Validation for Emergency Responders (SAVER) program were initiated by the U.S. Department of Homeland Security (DHS) for developing specifications and performance requirements for emergency responder equipment and procurement.<sup>403</sup> For example, both single-use and rechargeable Li-ion batteries with a cycle life of 400 cycles are required for firefighting equipment such as the self-contained breathing apparatus (SCBA).<sup>404</sup> Single-use AA batteries and C cell batteries had the best performance in SCBAs at elevated temperatures. At -20 °C (-4 °F), an SCBA with C-cell batteries showed the lowest performance, lasting about 1.5 hours in full alarm mode with electronic safety features active.<sup>405</sup> Moreover, single-use CR123 Li batteries did not discharge in high-temperature conditions. Testing results concluded that non-rechargeable back-up Li batteries failed to discharge at 54 °C (129 °F).<sup>405</sup> Li-based batteries are best for use for first responder and military applications at extremely low temperatures and not advised for fire conditions due to thermal runaway at 140 °C (284 °F).<sup>406</sup>

The total weight of battery systems and components is a primary concern for their design, as they are mostly used for unmanned aerial vehicle (UAV) power supplies. For UAVs, two key performance parameters are energy capacity and overall battery weight.<sup>407</sup> High energy density and low weight are important to sustain long UAV mission times. In addition to UAVs, military applications, including electromagnetic launch

systems, directed energy weapons, and other high-power equipment, require LIBs capable of sustaining ultrahigh-rate discharge profiles of 10C to 20C for prolonged periods.<sup>408,409</sup> These demanding conditions also necessitate a long charge/discharge cycle life. For example, the LIBs used in the 2003 Mars Exploration Rover were capable of exceeding 1000 cycles while maintaining 80% of their original capacity.<sup>410</sup> Looking ahead, future ground vehicles for military applications will likely follow the growth in electric vehicle development in the civilian sector, decreasing reliance on petroleum-based fuels.<sup>411</sup>

Achieving higher energy density, improved energy efficiency, extended cycle life, and longer calendar life in LIBs also requires careful handling, storage, and charging procedures to mitigate associated risks. According to safety guidance from United States Naval Sea Systems Command,<sup>412–414</sup> the total stored Li battery energy aboard ships must not exceed 1000 watt-hours in a single location, and that location must be approved by the Damage Control Assistant or Fire Marshal. In the event of thermal runaway, gases vented from burning Li cells may contain hazardous substances, such as HF. To minimize structural damage during such events, deliberate measures need to be placed to mitigate the direct impingement of hot gases from cell vents onto critical structural components of military platforms.

Furthermore, the catastrophic failure of LIBs can result in the release of large volumes of gas. To address this, pressure vessels are generally engineered with intentional failure mechanisms, preventing structural rupture using Belleville washers on bulkhead fasteners, urethane springs, and pressure relief devices such as discs, ports, or flapper valves.<sup>412–415</sup> The battery system must also be engineered to minimize the risk of short circuits caused by operator error or system malfunctions. Such mitigation can be achieved through the strategic use of electrical interruption devices and/or physical design layouts that protect both the user and the battery from injury or catastrophic failure. Electrical safety devices (ESDs), such as contactors, fuses, circuit breakers, need to be validated through testing under voltage and current conditions representative of both normal operation and potential failure scenarios.<sup>412–414</sup>

## 7. Conclusion

The interconnection between electrochemical reactions and mechanical stress has been shown to influence the performance and lifespan of LIB components. In particular, cathode degradation, which is driven by microcracking, phase transitions, and oxygen release, coupled with the intrinsic challenges of anode materials and electrolytes trigger a complex matrix of failure pathways that culminate in catastrophic thermal events. Advanced strategies to mitigate these risks have emerged as key enablers for next-generation LIBs. Structural modifications such as concentration-gradient designs and the development of nanorod cathode architectures have significantly improved Li<sup>+</sup> transport and mechanical integrity, while surface coating techniques using fluoride and phosphate compounds have



been effective in suppressing parasitic side reactions and stabilizing interfacial layers. On the anode side, composite architectures and A-SEI layers have demonstrated the potential to balance high energy density with enhanced mechanical stability. Moreover, electrolyte engineering has contributed to reducing flammability risks and extending the electrochemical stability window.

Operational factors, including extreme temperature variations and mechanical stresses, further complicate LIB performance, especially in demanding applications such as military operations. The integration of novel materials and engineering approaches that account for thermal and mechanical influences is critical for ensuring long-term reliability and safety. While significant progress has been achieved in understanding and mitigating degradation mechanisms in LIBs, ongoing research is essential. Future research should focus on improving the interfacial behaviors between electrodes and electrolytes by considering multifunctional electrolyte additives/solvents to develop better SEI layers that can withstand mechanical and thermal stresses. There is also a need to explore new electrolyte formulations that minimize parasitic reactions and enhance thermal stability, particularly in aqueous systems where current SEI layers are inadequate. Research should also focus on innovative electrode architectures, particularly cathodes, as cathode design has a more substantial impact on internal resistance and battery safety than anodes. Given the unique challenges faced in military and first responder applications, future work should specifically address the performance of LIBs under military-specific conditions, prioritizing focus on operations under harsh temperatures, mechanical shocks, and vibrations. Investigating advanced thermal management strategies is also crucial. This would be to develop materials that can dissipate heat more effectively and prevent thermal runaway events. Additionally, while not extensively covered in this review article, future research should focus on improving the mechanical and thermal stability of LIB separators, given the highlighted cell and pack-level risks that internal short circuits and damage to separators pose. These efforts will not only enhance battery performance and safety but will also pave the way for the broader adoption of LIB technology in safety-critical applications.

## Author contributions

The manuscript was written with contributions from all authors. All authors have approved the final version of the manuscript. Idris Adebanjo and Juliana Eko: original manuscript writing, editing, and formatting. Anita Gift Agbeyegbe: original manuscript writing and reviewing. Jang-Yeon Hwang and H. Hohyun Sun: idea conceptualization, supervision, and manuscript review. Simuck F. Yuk, Enoch A. Nagelli, Samuel V. Cowart, F. John Burpo, Jan L. Allen, and Dat T. Tran: original manuscript writing (military perspective). Nishma Bhattacharai: original manuscript writing. Krishna Shah: supervision and manuscript review.

## Data availability

The review paper is based on an analysis of existing literature. No primary research results have been included, and no new data was generated. The references used in this paper are publicly available and can be accessed through online databases.

## Conflicts of interest

There are no conflicts to declare.

## Acknowledgements

This work was supported by the University of Alabama College of Engineering startup funding. The views expressed herein are those of the authors and do not reflect the position of the United States Military Academy, the Department of the Army, or the Department of Defense.

## References

- 1 J. P. Pender, G. Jha, D. H. Youn, J. M. Ziegler, I. Andoni, E. J. Choi, A. Heller, B. S. Dunn, P. S. Weiss, R. M. Penner and C. B. Mullins, *Electrode Degradation in Lithium-Ion Batteries*, *ACS Nano*, 2020, **14**, 1243–1295.
- 2 S. Chen, Z. Gao and T. Sun, Safety Challenges and Safety Measures of Li-ion Batteries, *Energy Sci. Eng.*, 2021, **9**, 1647–1672.
- 3 D. Ren, X. Feng, L. Lu, M. Ouyang, S. Zheng, J. Li and X. He, An Electrochemical-Thermal Coupled Overcharge-to-Thermal-Runaway Model for Lithium-Ion Battery, *J. Power Sources*, 2017, **364**, 328–340.
- 4 E. A. Kapp, D. S. Wroth and J. T. Chapin, Analysis of Thermal Runaway Incidents Involving Lithium Batteries in U.S. Commercial Aviation, *Transp. Res. Rec.*, 2020, **2674**, 584–592.
- 5 Q. Wang, P. Ping, X. Zhao, G. Chu, J. Sun, C. Chen, Q. Wang, P. Ping, X. Zhao, G. Chu, J. Sun and C. Chen, Thermal Runaway Caused Fire and Explosion of Lithium-Ion Battery, *J. Power Sources*, 2012, **208**, 210–224.
- 6 J. Lamb, C. J. Orendorff, L. A. M. Steele and S. W. Spangler, Failure Propagation in Multi-Cell Lithium-Ion Batteries, *J. Power Sources*, 2014, **283**, 517–523.
- 7 J. Mouawad, Report on Boeing 787 Dreamliner Battery Flaws Finds Lapses at Multiple Points, 2014, <https://www.nytimes.com/2014/12/02/business/report-on-boeing-787-dreamliner-batteries-assigns-some-blame-for-flaws>, (accessed September 2024).
- 8 United States Consumer Product Safety Commission, Samsung Recalls Galaxy Note7 Smartphones Due to Serious Fire and Burn Hazards, 2017, <https://www.cpsc.gov/Recalls/2017/Samsung-Expands-Recall-of-Galaxy-Note7-Smartphones-Based-on-Additional-Incidents-with-Replacement-Phones>, (accessed September 2024).



9 M. McKinnon, S. DeCrane and S. Kerber, Four Firefighters Injured in Lithium-Ion Battery Energy Storage System Explosion-Arizona, 2020, DOI: [10.54206/102376/TEHS4612](https://doi.org/10.54206/102376/TEHS4612), (accessed September 2024).

10 A. Blum and T. Bensen, Victorian Big Battery Fire: July 30, 2021: Report of Technical Findings, 2021, <https://infrastructure.planninginspectorate.gov.uk/wp-content/uploads/projects/EN010106/EN010106-004097-DL2%20-%20Edmund%20Fordham%20EF20.pdf>, (accessed September 2024).

11 K. Liu, Y. Liu, D. Lin, A. Pei and Y. Cui, Materials for Lithium-Ion Battery Safety, *Sci. Adv.*, 2018, **168**, 110520.

12 H. H. Ryu, K. J. Park, C. S. Yoon and Y. K. Sun, Capacity fading of Ni-rich  $\text{Li}[\text{Ni}_x\text{Co}_y\text{Mn}_{1-x-y}]\text{O}_2$  ( $0.6 \leq x \leq 0.95$ ) Cathodes for High-Energy-Density Lithium-Ion Batteries: Bulk or Surface Degradation?, *Chem. Mater.*, 2018, **30**, 1155–1163.

13 J. Chen, H. Yang, T. Li, C. Liu, H. Tong, J. Chen, Z. Liu, L. Xia, Z. Chen, J. Duan and L. Li, The Effects of Reversibility of  $\text{H}_2\text{-H}_3$  Phase Transition on Ni-Rich Layered Oxide Cathode for High-Energy Lithium-Ion Batteries, *Front. Chem.*, 2019, **7**, 500.

14 T. Li, X. Z. Yuan, L. Zhang, D. Song, K. Shi and C. Bock, Degradation Mechanisms and Mitigation Strategies of Nickel-Rich NMC-Based Lithium-Ion Batteries, *Electrochem. Energy Rev.*, 2020, **3**, 43–80.

15 M. Jiang, D. L. Danilov, R. A. Eichel and P. H. L. Notten, A Review of Degradation Mechanisms and Recent Achievements for Ni-Rich Cathode-Based Li-Ion Batteries, *Adv. Energy Mater.*, 2021, **11**, 2103005.

16 K. J. Park, J. Y. Hwang, H. H. Ryu, F. Maglia, S. J. Kim, P. Lamp, C. S. Yoon and Y. K. Sun, Degradation Mechanism of Ni-Enriched NCA Cathode for Lithium Batteries: Are Microcracks Really Critical?, *ACS Energy Lett.*, 2019, **4**, 1394–1400.

17 H. H. Ryu, G. T. Park, C. S. Yoon and Y. K. Sun, Microstructural Degradation of Ni-Rich  $\text{Li}[\text{Ni}_x\text{Co}_y\text{Mn}_{1-x-y}]\text{O}_2$  Cathodes During Accelerated Calendar Aging, *Small*, 2018, **14**, 1803179.

18 L. Wu, K. W. Nam, X. Wang, Y. Zhou, J. C. Zheng, X. Q. Yang and Y. Zhu, Structural Origin of Overcharge-Induced Thermal Instability of Ni-Containing Layered-Cathodes for High-Energy-Density Lithium Batteries, *Chem. Mater.*, 2011, **23**, 3953–3960.

19 H. H. Sun, A. Doloçan, J. A. Weeks, R. Rodriguez, A. Heller and C. B. Mullins, In Situ Formation of a Multicomponent Inorganic-rich SEI layer Provides a Fast Charging and High Specific Energy Li-metal Battery, *J. Mater. Chem. A*, 2019, **7**, 17782–17789.

20 M. Jiang, D. L. Danilov, R. A. Eichel and P. H. L. Notten, A Review of Degradation Mechanisms and Recent Achievements for Ni-Rich Cathode-Based Li-Ion Batteries, *Adv. Energy Mater.*, 2021, **11**, 2103005.

21 Z. Zhang, S. Said, A. J. Lovett, R. Jervis, P. R. Shearing, D. J. L. Brett and T. S. Miller, The Influence of Cathode Degradation Products on the Anode Interface in Lithium-Ion Batteries, *ACS Nano*, 2024, **18**, 9389–9402.

22 L. Huang, G. Xu, X. Du, J. Li, B. Xie, H. Liu, P. Han, S. Dong, G. Cui and L. Chen, Uncovering LiH Triggered Thermal Runaway Mechanism of a High-Energy  $\text{LiNi}_{0.5}\text{Co}_{0.2}\text{Mn}_{0.3}\text{O}_2$ /Graphite Pouch Cell, *Adv. Sci.*, 2021, **8**, 2100676.

23 S. J. Gross, M. T. Hsieh, D. R. Mumm, L. Valdevit and A. Mohraz, Alleviating Expansion-Induced Mechanical Degradation in Lithium-Ion Battery Silicon Anodes via Morphological Design, *Extreme Mech. Lett.*, 2022, **54**, 101746.

24 M. T. McDowell, S. W. Lee, W. D. Nix and Y. Cui, 25th anniversary article: Understanding the Lithiation of Silicon and Other Alloying Anodes for Lithium-Ion Batteries, *Adv. Mater.*, 2013, **25**, 4966–4985.

25 Y. Lu, L. Yu and X. W. (David) Lou, Nanostructured Conversion-Type Anode Materials for Advanced Lithium-Ion Batteries, *Chem.*, 2018, **4**, 972–996.

26 S. H. Kim, K. Dong, H. Zhao, A. A. El-Zoka, X. Zhou, E. V. Woods, F. Giuliani, I. Manke, D. Raabe and B. Gault, Understanding the Degradation of a Model Si Anode in a Li-Ion Battery at the Atomic Scale, *J. Phys. Chem. Lett.*, 2022, **13**, 8416–8421.

27 Q. K. Zhang, X. Q. Zhang, H. Yuan and J. Q. Huang, Thermally Stable and Nonflammable Electrolytes for Lithium Metal Batteries: Progress and Perspectives, *Small Sci.*, 2021, **1**, 2100058.

28 J. Lamb, C. J. Orendorff, E. P. Roth and J. Langendorf, Studies on the Thermal Breakdown of Common Li-Ion Battery Electrolyte Components, *J. Electrochem. Soc.*, 2015, **162**, A2131–A2135.

29 Y. Liao, H. Zhang, Y. Peng, Y. Hu, J. Liang, Z. Gong, Y. Wei and Y. Yang, Electrolyte Degradation During Aging Process of Lithium-Ion Batteries: Mechanisms, Characterization, and Quantitative Analysis, *Adv. Energy Mater.*, 2024, **14**, 2304295.

30 Z. Zhu and J. Chen, Review—Advanced Carbon-Supported Organic Electrode Materials for Lithium (Sodium)-Ion Batteries, *J. Electrochem. Soc.*, 2015, **162**, A2393–A2405.

31 R. Febrian, N. L. W. Septiani, M. Iqbal and B. Yuliarto, Review—Recent Advances of Carbon-Based Nanocomposites as the Anode Materials for Lithium-Ion Batteries: Synthesis and Performance, *J. Electrochem. Soc.*, 2021, **168**, 110520.

32 F. Wang, O. Borodin, M. S. Ding, M. Gobet, J. Vatamanu, X. Fan, T. Gao, N. Edison, Y. Liang, W. Sun, S. Greenbaum, K. Xu and C. Wang, Hybrid Aqueous/Non-aqueous Electrolyte for Safe and High-Energy Li-Ion Batteries, *Joule*, 2018, **2**, 927–937.

33 S. Khalid, N. Pianta, P. Mustarelli and R. Ruffo, Use of Water-In-Salt Concentrated Liquid Electrolytes in Electrochemical Energy Storage: State of the Art and Perspectives, *Batteries*, 2023, **9**, 9010047.

34 J. Yang, X. Liang, H. H. Ryu, C. S. Yoon and Y. K. Sun, Ni-rich Layered Cathodes for Lithium-Ion Batteries: From Challenges to the Future, *Energy Storage Mater.*, 2023, **63**, 102969.



35 H. Zhang, Z. Zeng, S. Cheng and J. Xie, Recent Progress and Perspective on Lithium Metal Battery with Nickel-Rich Layered Oxide Cathode, *eScience*, 2024, **4**, 100265.

36 Q. Tao, L. Wang, C. Shi, J. Li, G. Chen, Z. Xue, J. Wang, S. Wang and H. Jin, Understanding the Ni-rich Layered Structure Materials for High-Energy Density Lithium-Ion Batteries, *Mater. Chem. Front.*, 2021, **5**, 2607–2622.

37 Y. Chen, G. X. Wang, K. Konstantinov, H. K. Liu and S. X. Dou, Synthesis and Characterization of  $\text{LiCo}_x\text{Mn}_y\text{Ni}_{1-x-y}\text{O}_2$  as a Cathode Material for Secondary Lithium Batteries, *J. Power Sources*, 2023, **119–121**, 184–188.

38 Y. K. Sun, S. T. Myung, B. C. Park, J. Prakash, I. Belharouak and K. Amine, High-Energy Cathode Material for Long-Life and Safe Lithium Batteries, *Nat. Mater.*, 2009, **8**, 320–324.

39 S. T. Myung, F. Maglia, K. J. Park, C. S. Yoon, P. Lamp, S. J. Kim and Y. K. Sun, Nickel-Rich Layered Cathode Materials for Automotive Lithium-Ion Batteries: Achievements and Perspectives, *ACS Energy Lett.*, 2017, **2**, 196–223.

40 R. Lin, S. M. Bak, Y. Shin, R. Zhang, C. Wang, K. Kisslinger, M. Ge, X. Huang, Z. Shadike, A. Pattammattel, H. Yan, Y. Chu, J. Wu, W. Yang, M. S. Whittingham, H. L. Xin and X. Q. Yang, Hierarchical Nickel Valence Gradient Stabilizes High-Nickel Content Layered Cathode Materials, *Nat. Commun.*, 2021, **12**, 1–10.

41 H. H. Sun, H. H. Ryu, U. H. Kim, J. A. Weeks, A. Heller, Y. K. Sun and C. B. Mullins, Beyond Doping and Coating: Prospective Strategies for Stable High-Capacity Layered Ni-Rich Cathodes, *ACS Energy Lett.*, 2020, **5**, 1136–1146.

42 Y. K. Sun, Z. Chen, H. J. Noh, D. J. Lee, H. G. Jung, Y. Ren, S. Wang, C. S. Yoon, S. T. Myung and K. Amine, Nanostructured High-Energy Cathode Materials for Advanced Lithium Batteries, *Nat. Mater.*, 2012, **11**, 942–947.

43 J. H. Ge, M. Y. Xie, Q. F. Zhao, S. Q. Zhang and H. Sun, Advances in Co-Free Layered Cathode Materials for Li-Ion Batteries, *Int. J. Electrochem. Sci.*, 2023, **18**, 100292.

44 S. Aryal, J. L. Durham, A. L. Lipson, K. Z. Pupek and O. Kahvecioglu, Roles of Mn and Co in Ni-Rich Layered Oxide Cathodes Synthesized Utilizing a Taylor Vortex Reactor, *Electrochim. Acta*, 2021, **391**, 138929.

45 E. Jo, J. H. Park, J. Park, J. Hwang, K. Y. Chung, K. W. Nam, S. M. Kim and W. Chang, Different Thermal Degradation Mechanisms: Role of Aluminum in Ni-rich Layered Cathode Materials, *Nano Energy*, 2020, **78**, 105367.

46 Y. Su, Q. Zhang, L. Chen, L. Bao, Y. Lu, S. Chen and F. Wu, Stress Accumulation in Ni-Rich Layered Oxide Cathodes: Origin, Impact, and Resolution, *J. Energy Chem.*, 2022, **65**, 236–253.

47 S. Zhao, Z. Guo, K. Yan, S. Wan, F. He, B. Sun and G. Wang, Towards High-Energy-Density Lithium-Ion Batteries: Strategies for Developing High-Capacity Lithium-Rich Cathode Materials, *Energy Storage Mater.*, 2021, **34**, 716–734.

48 S. Cao, C. Wu, X. Xie, H. Li, Z. Zang, Z. Li, G. Chen, X. Guo and X. Wang, Suppressing the Voltage Decay Based on a Distinct Stacking Sequence of Oxygen Atoms for Li-Rich Cathode Materials, *ACS Appl. Mater. Interfaces*, 2021, **13**, 17639–17648.

49 X. Cao, H. Li, Y. Qiao, M. Jia, P. He, J. Cabana and H. Zhou, Achieving Stable Anionic Redox Chemistry in Li-Excess  $\text{O}_2$ -type layered oxide cathode via chemical ion-exchange strategy, *Energy Storage Mater.*, 2021, **38**, 1–8.

50 W. He, W. Guo, H. Wu, L. Lin, Q. Liu, X. Han, Q. Xie, P. Liu, H. Zheng, L. Wang, X. Yu and D.-L. Peng, Challenges and Recent Advances in High Capacity Li-Rich Cathode Materials for High Energy Density Lithium-Ion Batteries, *Adv. Mater.*, 2021, **33**, 2005937.

51 H. Xie, J. Xiao, H. Chen, B. Zhang, K. N. Hui, S. Zhang, C. Liu, D. Luo and Z. Lin, Fundamental Understanding of Voltage Decay in Li-rich Mn-Based Layered Oxides Cathode Materials, *AAPPS Bull.*, 2024, **34**, 1–34.

52 Y. Xie, Y. Jin and L. Xiang, Li-Rich Layered Oxides: Structure, Capacity and Voltage Fading Mechanisms and Solving Strategies, *Particuology*, 2022, **61**, 1–10.

53 Z. Wang, H. Luo, H. Liu, F. Wu, C. Zhang, Z. Wang and P. Yu, Electrochemical Performance and Structural Stability of Layered Li–Ni–Co–Mn Oxide Cathode Materials in Different Voltage Ranges, *Ceram. Int.*, 2021, **47**, 8490–8497.

54 B. Li, Z. Zhuo, L. Zhang, A. Iadecola, X. Gao, J. Guo, W. Yang, A. V. Morozov, A. M. Abakumov and J. M. Tarascon, Decoupling the roles of Ni and Co in Anionic Redox Activity of Li-rich NMC Cathodes, *Nat. Mater.*, 2023, **22**, 1370–1379.

55 Q. Li, D. Ning, D. Wong, K. An, Y. Tang, D. Zhou, G. Schuck, Z. Chen, N. Zhang and X. Liu, Improving the Oxygen Redox Reversibility of Li-Rich Battery Cathode Materials via Coulombic Repulsive Interactions Strategy, *Nat. Commun.*, 2022, **13**, 1123.

56 Z. Li, S. Cao, J. Chen, L. Wu, M. Chen, H. Ding, R. Wang, W. Guo, Y. Bai, M. Liu and X. Wang, Modulating Surface Architecture and Electronic Conductivity of Li-rich Manganese-Based Cathode, *Small*, 2024, **20**, 2400641.

57 H. He, H. Li, X. Bai, Z. Chang, Z. Gao, X. Zhang and Z. Ren, Comparative Study of High-Temperature Cycling and Thermal Stability of LLOs and NCMs under Medium-High Voltage, *Energy Fuels*, 2023, **37**, 6854–6864.

58 X. Li, Q. Gu, B. Qiu, C. Yin, Z. Wei, W. Wen, Y. Zhang, Y. Zhou, H. Gao, H. Liang, Z. He, M. Zhang, Y. S. Meng and Z. Liu, Rational Design of Thermally Stable Polymorphic Layered Cathode Materials for Next Generation Lithium Rechargeable Batteries, *Mater. Today*, 2022, **61**, 91–103.

59 H. Zheng, X. Han, W. Guo, L. Lin, Q. Xie, P. Liu, W. He, L. Wang and D. L. Peng, Recent Developments and Challenges of Li-Rich Mn-Based Cathode Materials for High-Energy Lithium-Ion Batteries, *Mater. Today Energy*, 2020, **18**, 100518.

60 J. Liu, J. Wang, Y. Ni, K. Zhang, F. Cheng and J. Chen, Recent Breakthroughs and Perspectives of High-Energy Layered Oxide Cathode Materials for Lithium Ion Batteries, *Mater. Today*, 2021, **43**, 132–165.

61 L. de Biasi, B. Schwarz, T. Brezesinski, P. Hartmann, J. Janek and H. Ehrenberg, Chemical, Structural, and Electronic Aspects of Formation and Degradation Behavior on Different Length Scales of Ni-Rich NCM and Li-Rich



HE-NCM Cathode Materials in Li-Ion Batteries, *Adv. Mater.*, 2019, **31**, 1900985.

62 X. Zhu, A. Huang, I. Martens, N. Vostrov, Y. Sun, M. I. Richard, T. U. Schülli and L. Wang, High-Voltage Spinel Cathode Materials: Navigating the Structural Evolution for Lithium-Ion Batteries, *Adv. Mater.*, 2024, **36**, 2403482.

63 W. D. Johnston and R. R. Heikes, A Study of the  $\text{Li}_x\text{Mn}_{(1-x)}\text{O}$  System, *J. Am. Chem. Soc.*, 1956, **78**, 3255–3260.

64 S. Liu, B. Wang, X. Zhang, S. Zhao, Z. Zhang and H. Yu, Reviving the Lithium-Manganese-Based Layered Oxide Cathodes for Lithium-Ion Batteries, *Matter*, 2021, **4**, 1511–1527.

65 X. Zhu, A. Huang, I. Martens, N. Vostrov, Y. Sun, M. I. Richard, T. U. Schülli and L. Wang, High-Voltage Spinel Cathode Materials: Navigating the Structural Evolution for Lithium-Ion Batteries, *Adv. Mater.*, 2024, **36**, 2403482.

66 W. Wen, B. Kumarasamy, S. Mukerjee, M. Auinat and Y. Ein-Eli, Origin of 5 V Electrochemical Activity Observed in Non-Redox Reactive Divalent Cation Doped  $\text{LiM}_{0.5-x}\text{Mn}_{1.5+x}\text{O}_4$  ( $0 < 0.5$ ) Cathode Materials In Situ XRD and XANES Spectroscopy Studies, *J. Electrochem. Soc.*, 2005, **152**, A1902.

67 M. Armand, P. Axmann, D. Bresser, M. Copley, K. Edström, C. Ekberg, D. Guyomard, B. Lestriez, P. Novák, M. Petranikova, W. Porcher, S. Trabesinger, M. Wohlfahrt-Mehrens and H. Zhang, Lithium-Ion Batteries – Current State of the Art and Anticipated Developments, *J. Power Sources*, 2020, **479**, 228708.

68 Y. Huang, Y. Dong, S. Li, J. Lee, C. Wang, Z. Zhu, W. Xue, Y. Li and J. Li, Lithium Manganese Spinel Cathodes for Lithium-Ion Batteries, *Adv. Energy Mater.*, 2021, **11**, 2000997.

69 Y. Deng, L. He, J. Ren, Q. Zheng, C. Xu and D. Lin, Reinforcing Cycling Stability and Rate Capability of  $\text{LiNi}_{0.5}\text{Mn}_{1.5}\text{O}_4$  Cathode by Dual-Modification of Coating and Doping of a Fast-Ion Conductor, *Mater. Res. Bull.*, 2018, **100**, 333–344.

70 S. Geller and J. L. Durand, Refinement of the Structure of  $\text{LiMnPO}_4$ , *Acta Crystallogr.*, 1960, **13**, 325–331.

71 A. K. Padhi, K. S. Nanjundaswamy and J. B. Goodenough, Phospho-Olivines as Positive-Electrode Materials for Rechargeable Lithium Batteries, *J. Electrochem. Soc.*, 1997, **144**, 1188–1194.

72 J. Li and Z.-F. Ma, Past and Present of  $\text{LiFePO}_4$ : From Fundamental Research to Industrial Applications, *Chem.*, 2019, **5**, 3–6.

73 T. V. S. L. Satyavani, A. Srinivas Kumar and P. S. V. Subba Rao, Methods of Synthesis and Performance Improvement of Lithium Iron Phosphate for High Rate Li-Ion Batteries: A Review, *Eng. Sci. Technol., Int. J.*, 2016, **19**, 178–188.

74 S. W. Oh, S. T. Myung, S. M. Oh, K. H. Oh, K. Amine, B. Scrosati and Y. K. Sun, Double Carbon Coating of  $\text{LiFePO}_4$  as High Rate Electrode for Rechargeable Lithium Batteries, *Adv. Mater.*, 2010, **22**, 4842–4845.

75 S. W. Oh, S. T. Myung, H. J. Bang, C. S. Yoon, K. Amine and Y. K. Sun, Nanoporous Structured  $\text{LiFePO}_4$  with Spherical Microscale Particles having High Volumetric Capacity for Lithium Batteries, *Electrochem. Solid-State Lett.*, 2009, **12**, A181.

76 K. Y. Park, I. Park, H. Kim, G. Yoon, H. Gwon, Y. Cho, Y. S. Yun, J. J. Kim, S. Lee, D. Ahn, Y. Kim, H. Kim, I. Hwang, W. S. Yoon and K. Kang, Lithium-Excess Olivine Electrode for Lithium Rechargeable Batteries, *Energy Environ. Sci.*, 2016, **9**, 2902–2915.

77 Q. Zhao, Y. Zhang, Y. Meng, Y. Wang, J. Ou, Y. Guo and D. Xiao, Phytic Acid Derived  $\text{LiFePO}_4$  Beyond Theoretical Capacity as High-Energy Density Cathode for Lithium Ion Battery, *Nano Energy*, 2017, **34**, 408–420.

78 Z. Yang and S. Wang, High Cycling Performance Cathode Material: Interconnected  $\text{LiFePO}_4$ /Carbon Nanoparticles Fabricated by Sol-Gel Method, *J. Nanomater.*, 2014, **2014**, 1–7.

79 M. Yang, Y. Ye, A. Yang, Z. Jiang, X. Wang, H. Yuan and M. Rong, Comparative Study on Aging and Thermal Runaway of Commercial  $\text{LiFePO}_4$ /Graphite Battery Undergoing Slight Overcharge Cycling, *J. Energy Storage*, 2022, **50**, 104691.

80 Y. Zhang, S. Cheng, W. Mei, L. Jiang, Z. Jia, Z. Cheng, J. Sun and Q. Wang, Understanding of thermal runaway mechanism of  $\text{LiFePO}_4$  battery in-depth by three-level analysis, *Appl. Energy*, 2023, **336**, 120695.

81 L. Song, Z. Huang, W. Mei, Z. Jia, Y. Yu, Q. Wang and K. Jin, Thermal Runaway Propagation Behavior and Energy Flow Distribution Analysis of 280 A h  $\text{LiFePO}_4$  Battery, *Process Saf. Environ. Prot.*, 2023, **170**, 1066–1078.

82 H. Chen, K. Yang, Y. Liu, M. Zhang, H. Liu, J. Liu, Z. Qu and Y. Lai, Experimental Investigation of Thermal Runaway Behavior and Hazards of a 1440 A h  $\text{LiFePO}_4$  Battery Pack, *Energies*, 2023, **16**, 3398.

83 F. Qian, H. Wang, M. Li, C. Li, H. Shen, J. Wang, Y. Li and M. Ouyang, Thermal Runaway Vent Gases from High-Capacity Energy Storage  $\text{LiFePO}_4$  Lithium Iron, *Energies*, 2023, **16**, 3485.

84 K. Feng, M. Li, W. Liu, A. G. Kashkooli, X. Xiao, M. Cai and Z. Chen, Silicon-Based Anodes for Lithium-Ion Batteries: From Fundamentals to Practical Applications, *Small*, 2018, **14**, 1702737.

85 F. K. Tareq and S. Rudra, Enhancing the Performance of Silicon-Based Anode Materials for Alkali Metal (Li, Na, K) Ion Battery: A Review on Advanced Strategies, *Mater. Today Commun.*, 2024, **39**, 108653.

86 M. Khan, S. Yan, M. Ali, F. Mahmood, Y. Zheng, G. Li, J. Liu, X. Song and Y. Wang, Innovative Solutions for High-Performance Silicon Anodes in Lithium-Ion Batteries: Overcoming Challenges and Real-World Applications, *Nano-Micro Lett.*, 2024, **16**, 179.

87 X. Meng, Y. Xu, H. Cao, X. Lin, P. Ning, Y. Zhang, Y. G. Garcia and Z. Sun, Internal Failure of Anode



Materials for Lithium Batteries—A Critical Review, *Green Energy Environ.*, 2020, **5**, 22–36.

88 K. Feng, M. Li, W. Liu, A. G. Kashkooli, X. Xiao, M. Cai and Z. Chen, Silicon-Based Anodes for Lithium-Ion Batteries: From Fundamentals to Practical Applications, *Small*, 2018, **14**, 1702737.

89 M. A. Rahman, G. Song, A. I. Bhatt, Y. C. Wong and C. Wen, Nanostructured Silicon Anodes for High-Performance Lithium-Ion Batteries, *Adv. Funct. Mater.*, 2016, **26**, 647–678.

90 G. G. Eshetu, H. Zhang, X. Judez, H. Adenusi, M. Armand, S. Passerini and E. Figgemeier, Production of High-Energy Li-Ion Batteries Comprising Silicon-Containing Anodes and Insertion-Type Cathodes, *Nat. Commun.*, 2021, **12**, 5459.

91 W. Yang, H. Ying, S. Zhang, R. Guo, J. Wang and W. Q. Han, Electrochemical Performance Enhancement of Porous Si Lithium-Ion Battery Anode by Integrating with Optimized Carbonaceous Materials, *Electrochim. Acta*, 2020, **337**, 135687.

92 K. Pan, F. Zou, M. Canova, Y. Zhu and J. H. Kim, Systematic Electrochemical Characterizations of Si and SiO Anodes for High-Capacity Li-Ion Batteries, *J. Power Sources*, 2019, **413**, 20–28.

93 P. Poizot, S. Laruelle, S. Grugeon, L. Dupont and J.-M. Tarascon, Nano-Sized Transition-Metal Oxides as Negative-Electrode Materials for Lithium-Ion Batteries, *Nature*, 2000, **407**, 496–499.

94 A. S. Aricò, P. Bruce, B. Scrosati, J.-M. Tarascon and W. van Schalkwijk, Nanostructured Materials for Advanced Energy Conversion and Storage Devices, *Nat. Mater.*, 2005, **4**, 366–377.

95 S. H. Yu, S. H. Lee, D. J. Lee, Y. E. Sung and T. Hyeon, Conversion Reaction-Based Oxide Nanomaterials for Lithium Ion Battery Anodes, *Small*, 2016, **12**, 2146–2172.

96 G. A. Li, C. Y. Wang, W. C. Chang and H. Y. Tuan, Phosphorus-Rich Copper Phosphide Nanowires for Field-Effect Transistors and Lithium-Ion Batteries, *ACS Nano*, 2016, **10**, 8632–8644.

97 J. Zhu, L. Bai, Y. Sun, X. Zhang, Q. Li, B. Cao, W. Yan and Y. Xie, Topochemical Transformation Route to Atomically thick  $\text{Co}_3\text{O}_4$  Nanosheets Realizing Enhance Lithium Storage Performance, *Nanoscale*, 2013, **5**, 5241–5246.

98 S. Zhang, B. V. R. Chowdari, Z. Wen, J. Jin and J. Yang, Constructing Highly Oriented Configuration by Few-Layer  $\text{MoS}_2$ : Toward High-Performance Lithium-Ion Batteries and Hydrogen Evolution Reactions, *ACS Nano*, 2015, **9**, 12464–12472.

99 L. Yu, L. Zhang, H. Bin Wu, G. Zhang and X. W. Lou, Controlled Synthesis of Hierarchical  $\text{Co}_x\text{Mn}_{3-x}\text{O}_4$  Array Micro-/Nanostructures with Tunable Morphology and Composition as Integrated Electrodes for Lithium-Ion Batteries, *Energy Environ. Sci.*, 2013, **6**, 2664–2671.

100 F. X. Ma, H. Hu, H. Bin Wu, C. Y. Xu, Z. Xu, L. Zhen and X. W. Lou, Formation of Uniform  $\text{Fe}_3\text{O}_4$  Hollow Spheres Organized by Ultrathin Nanosheets and Their Excellent Lithium Storage Properties, *Adv. Mater.*, 2015, **27**, 4097–4101.

101 P. Wang, H. Sun, Y. Ji, W. Li, X. Wang, P. Wang, Y. Ji, W. Li, X. Wang and H. Sun, Three-Dimensional Assembly of Single-Layered  $\text{MoS}_2$ , *Adv. Mater.*, 2014, **26**, 964–969.

102 J. Asenbauer, T. Eisenmann, M. Kuenzel, A. Kazzazi, Z. Chen and D. Bresser, The Success Story of Graphite as a Lithium-Ion Anode Material—Fundamentals, Remaining Challenges, and Recent Developments Including Silicon (Oxide) Composites, *Sustainable Energy Fuels*, 2020, **4**, 5387–5416.

103 J. Asenbauer, T. Eisenmann, M. Kuenzel, A. Kazzazi, Z. Chen and D. Bresser, The Success Story of Graphite as a Lithium-Ion Anode Material—Fundamentals, Remaining Challenges, and Recent Developments Including Silicon (Oxide) Composites, *Sustainable Energy Fuels*, 2020, **4**, 5387–5416.

104 J. He, J. Meng and Y. Huang, Challenges and Recent Progress In Fast-Charging Lithium-Ion Battery Materials, *J. Power Sources*, 2023, **570**, 232965.

105 J. Qian, W. A. Henderson, W. Xu, P. Bhattacharya, M. Engelhard, O. Borodin and J. G. Zhang, High Rate and Stable Cycling of Lithium Metal Anode, *Nat. Commun.*, 2015, **6**, 1–9.

106 W.-Z. Huang, P. Xu, X.-Y. Huang, C.-Z. Zhao, X. Bie, H. Zhang, A. Chen, E. Kuzmina, E. Karaseva, V. Kolosnitsyn, X. Zhai, T. Jiang, L.-Z. Fan, D. Wang and Q. Zhang, Lithium Metal Anode: Past, Present, and Future, *MetalMat*, 2024, **1**, e6.

107 J. Gao, R. He, P. Wu and K. H. Luo, Unravelling Multi-Layered Structure of Native SEI on Lithium Metal Electrode and Various Electrolytes Using Reactive Molecular Dynamics, *J. Energy Storage*, 2025, **106**, 114919.

108 N. Sarfraz, N. Kanwal, M. Ali, K. Ali, A. Hasnain, M. Ashraf, M. Ayaz, J. Ifthikar, S. Ali, A. Hendi, N. Baig, M. F. Ehsan, S. S. Shah, R. Khan and I. Khan, Materials Advancements In Solid-State Inorganic Electrolytes for Highly Anticipated All Solid Li-Ion Batteries, *Energy Storage Mater.*, 2024, **71**, 103619.

109 J. Deng, X. Yang and G. Zhang, Simulation Study on Internal Short Circuit of Lithium Ion Battery Caused by Lithium Dendrite, *Mater. Today Commun.*, 2022, **31**, 103570.

110 C. Hogrefe, T. Waldmann, M. Hözlé and M. Wohlfahrt-Mehrens, Direct Observation of Internal Short Circuits by Lithium Dendrites in Cross-Sectional Lithium-Ion In Situ Full Cells, *J. Power Sources*, 2023, **556**, 232391.

111 USABC, USABC Goals for Low-Cost/Fast-Charge Advanced Batteries for Electric Vehicles, 2023, <https://uscar.org/usabc/>, (accessed September 2024).

112 M. Weiss, R. Ruess, J. Kasnatscheew, Y. Levartovsky, N. R. Levy, P. Minnmann, L. Stolz, T. Waldmann, M. Wohlfahrt-Mehrens, D. Aurbach, M. Winter, Y. Ein-Eli and J. Janek, Fast Charging of Lithium-Ion Batteries: A Review of Materials Aspects, *Adv. Energy Mater.*, 2021, **11**, 2101126.



113 X. Ding, Q. Zhou, X. Li and X. Xiong, Fast-Charging Anodes for Lithium Ion Batteries: Progress and Challenges, *Chem. Commun.*, 2014, **60**, 2472–2488.

114 J. T. Han, Y. H. Huang and J. B. Goodenough, New Anode Framework for Rechargeable Lithium Batteries, *Chem. Mater.*, 2011, **23**, 2027–2029.

115 M. Odziomek, F. Chaput, A. Rutkowska, K. Świerczek, D. Olszewska, M. Sitarz, F. Lerouge and S. Parola, Hierarchically Structured Lithium Titanate for Ultrafast Charging in Long-Life High Capacity Batteries, *Nat. Commun.*, 2017, **8**, 1–7.

116 Z. N. Ezyeh, M. Khodaei and F. Torabi, Review on Doping Strategy in  $\text{Li}_4\text{Ti}_5\text{O}_{12}$  as an Anode Material for Lithium-Ion Batteries, *Ceram. Int.*, 2023, **49**, 7105–7141.

117 C. P. Sandhya, B. John and C. Gouri, Lithium Titanate as Anode Material for Lithium-Ion Cells: A Review, *Ionics*, 2014, **20**, 601–620.

118 J. L. Allen, X. Ren, C. K. Nguyen, D. C. Horn, H. H. Sun and D. T. Tran, High Conductivity and Rate Capability of  $\text{NaNb}_{13}\text{O}_{33}$  Wadsley–Roth Phase as a Fast-Charging Li-Ion Anode, *ChemElectroChem*, 2023, **10**, e202300267.

119 Y. Yang and J. Zhao, Wadsley–Roth Crystallographic Shear Structure Niobium-Based Oxides: Promising Anode Materials for High-Safety Lithium-Ion Batteries, *Adv. Sci.*, 2021, **8**, 2004855.

120 M. Saber, S. S. Behara and A. Van der Ven, Redox Mechanisms, Structural Changes, and Electrochemistry of the Wadsley–Roth  $\text{Li}_x\text{TiNb}_2\text{O}_7$  Electrode Material, *Chem. Mater.*, 2023, **35**, 9657–9668.

121 M. Saber and A. Van der Ven, Redox Mechanisms upon the Lithiation of Wadsley–Roth Phases, *Inorg. Chem.*, 2024, **63**, 11041–11052.

122 M. B. Preefer, M. Saber, Q. Wei, N. H. Bashian, J. D. Bocarsly, W. Zhang, G. Lee, J. Milam-Guerrero, E. S. Howard, R. C. Vincent, B. C. Melot, A. Van Der Ven, R. Seshadri and B. S. Dunn, Multielectron Redox and Insulator-to-Metal Transition upon Lithium Insertion in the Fast-Charging, Wadsley–Roth Phase  $\text{PNb}_9\text{O}_{25}$ , *Chem. Mater.*, 2020, **32**, 4553–4563.

123 K. Xu, Nonaqueous Liquid Electrolytes for Lithium-Based Rechargeable Batteries, *Chem. Rev.*, 2004, **104**, 4303–4417.

124 B. Flamme, G. Rodriguez Garcia, M. Weil, M. Haddad, P. Phansavath, V. Ratovelomanana-Vidal and A. Chagnes, Guidelines to Design Organic Electrolytes for Lithium-Ion batteries: Environmental Impact, Physicochemical and Electrochemical Properties, *Green Chem.*, 2017, **19**, 1828–1849.

125 S. Kainat, J. Anwer, A. Hamid, N. Gull and S. M. Khan, Electrolytes in Lithium-Ion Batteries: Advancements in the Era of Twenties (2020's), *Mater. Chem. Phys.*, 2024, **313**, 128796.

126 L. Chen, J. Shu, Y. Huang, Z. Shi, H. Luo, Z. Liu and C. Shen, Engineering Solid Electrolyte Interphase for the Application of Propylene Carbonate Solvent for Graphite Anode in Low Temperate Battery, *Appl. Surf. Sci.*, 2022, **598**, 153740.

127 J. Lee, Y. J. Kim, H. S. Jin, H. Noh, H. Kwack, H. Chu, F. Ye, H. Lee and H. T. Kim, Tuning Two Interfaces with Fluoroethylene Carbonate Electrolytes for High-Performance Li/LCO Batteries, *ACS Omega*, 2019, **4**, 3220–3227.

128 S. J. An, J. Li, C. Daniel, D. Mohanty, S. Nagpure and D. L. Wood, The State of Understanding of the Lithium-Ion-Battery Graphite Solid Electrolyte Interphase (SEI) and Its Relationship to Formation Cycling, *Carbon*, 2016, **105**, 52–76.

129 X. Han, L. Lu, Y. Zheng, X. Feng, Z. Li, J. Li and M. Ouyang, A Review on the Key Issues of the Lithium Ion Battery Degradation Among the Whole Life Cycle, *eTransportation*, 2019, **1**, 100005.

130 J. P. Pender, G. Jha, D. H. Youn, J. M. Ziegler, I. Andoni, E. J. Choi, A. Heller, B. S. Dunn, P. S. Weiss, R. M. Penner and C. B. Mullins, Electrode Degradation in Lithium-Ion Batteries, *ACS Nano*, 2020, **14**, 1243–1295.

131 S. Wang, J. Shi, Z. Liu and Y. Xia, Advanced Ether-Based Electrolytes for Lithium-ion Batteries, *Adv. Energy Mater.*, 2024, **14**, 2401526.

132 D. Luo, M. Li, Y. Zheng, Q. Ma, R. Gao, Z. Zhang, H. Dou, G. Wen, L. Shui, A. Yu, X. Wang and Z. Chen, Electrolyte Design for Lithium Metal Anode-Based Batteries Toward Extreme Temperature Application, *Adv. Sci.*, 2021, **8**, 2101051.

133 C. Barchasz, J. C. Leprêtre, S. Patoux and F. Alloin, Electrochemical Properties of Ether-Based Electrolytes for Lithium/Sulfur Rechargeable Batteries, *Electrochim. Acta*, 2013, **89**, 737–743.

134 Z. Li, H. Rao, R. Atwi, B. M. Sivakumar, B. Gwalani, S. Gray, K. S. Han, T. A. Everett, T. A. Ajantiwalay, V. Murugesan, N. N. Rajput and V. G. Pol, Non-Polar Ether-Based Electrolyte Solutions for Stable High-Voltage Non-Aqueous Lithium Metal Batteries, *Nat. Commun.*, 2023, **14**, 868.

135 M. S. Park, S. B. Ma, D. J. Lee, D. Im, S. G. Doo and O. Yamamoto, A Highly Reversible Lithium Metal Anode, *Sci. Rep.*, 2014, **4**, 3815.

136 F. Baskoro, H. Q. Wong and H. J. Yen, Strategic Structural Design of a Gel Polymer Electrolyte toward a High Efficiency Lithium-Ion Battery, *ACS Appl. Energy Mater.*, 2019, **2**, 3937–3971.

137 G. Feuillade and P. Perche, Ion-Conductive Macromolecular Gels and Membranes for Solid Lithium Cells, *J. Appl. Electrochem.*, 1975, **5**, 63–69.

138 J. Castillo, A. Santiago, X. Judez, I. Garbayo, J. A. Coca Clemente, M. C. Morant-Miñana, A. Villaverde, J. A. González-Marcos, H. Zhang, M. Armand and C. Li, Safe, Flexible, and High-Performing Gel-Polymer Electrolyte for Rechargeable Lithium Metal Batteries, *Chem. Mater.*, 2021, **33**, 8812–8821.

139 L. Long, S. Wang, M. Xiao and Y. Meng, Polymer Electrolytes for Lithium Polymer Batteries, *J. Mater. Chem. A*, 2016, **4**, 10038–10039.

140 W. Yang, W. Yang, J. Zeng, Y. Chen, Y. Huang, J. Liu, J. Gan, T. Li, H. Zhang, L. Zhong and X. Peng, Biopolymer-Based Gel Electrolytes for Electrochemical Energy Storage:



Advances and Prospects, *Prog. Mater. Sci.*, 2024, **144**, 101264.

141 J. Hassoun and B. Scrosati, Review—Advances in Anode and Electrolyte Materials for the Progress of Lithium-Ion and beyond Lithium-Ion Batteries, *J. Electrochem. Soc.*, 2015, **162**, A2582–A2588.

142 W. Chae, B. Kim, W. S. Ryoo and T. Earmme, A Brief Review of Gel Polymer Electrolytes Using In Situ Polymerization for Lithium-ion Polymer Batteries, *Polymers*, 2023, **15**, 803.

143 X. Lu, Y. Wang, X. Xu, B. Yan, T. Wu and L. Lu, Polymer-Based Solid-State Electrolytes for High-Energy-Density Lithium-Ion Batteries – Review, *Adv. Energy Mater.*, 2023, **13**, 2301746.

144 X. Cheng, J. Pan, Y. Zhao, M. Liao and H. Peng, Gel Polymer Electrolytes for Electrochemical Energy Storage, *Adv. Energy Mater.*, 2018, **8**, 1702184.

145 A. Arya and A. L. Sharma, Polymer Electrolytes for Lithium Ion Batteries: A Critical Study, *Ionics*, 2017, **23**, 497–540.

146 Z. Li, G. Su, X. Wang and D. Gao, Micro-Porous P(VDF-HFP)-Based Polymer Electrolyte Filled with  $\text{Al}_2\text{O}_3$  Nanoparticles, *Solid State Ionics*, 2005, **176**, 1903–1908.

147 H. Tsukasaki, W. Fukuda, H. Morimoto, T. Arai, S. Mori, A. Hayashi and M. Tatsumisago, Thermal Behavior and Microstructures of Cathodes for Liquid Electrolyte-Based Lithium Batteries, *Sci. Rep.*, 2018, **8**, 15613.

148 Y. Li, X. Liu, L. Wang, X. Feng, D. Ren, Y. Wu, G. Xu, L. Lu, J. Hou, W. Zhang, Y. Wang, W. Xu, Y. Ren, Z. Wang, J. Huang, X. Meng, X. Han, H. Wang, X. He, Z. Chen, K. Amine and M. Ouyang, Thermal Runaway Mechanism of Lithium-Ion battery with  $\text{LiNi}_{0.8}\text{Mn}_{0.1}\text{Co}_{0.1}\text{O}_2$  Cathode Materials, *Nano Energy*, 2021, **85**, 105878.

149 Y. Chu, Y. Mu, L. Zou, F. Wu, L. Yang, Y. Feng and L. Zeng, Oxygen Release in Ni-Rich Layered Cathode for Lithium-Ion Batteries: Mechanisms and Mitigating Strategies, *ChemElectroChem*, 2024, **11**, e202300653.

150 N. Y. Park, G. T. Park, S. Bin Kim, W. Jung, B. C. Park and Y. K. Sun, Degradation Mechanism of Ni-Rich Cathode Materials: Focusing on Particle Interior, *ACS Energy Lett.*, 2022, **7**, 2362–2369.

151 H. H. Ryu, K. J. Park, C. S. Yoon and Y. K. Sun, Capacity Fading of Ni-rich  $\text{Li}[\text{Ni}_x\text{Co}_y\text{Mn}_{1-x-y}]\text{O}_2$  ( $0.6 \leq x \leq 0.95$ ) Cathodes for High-Energy-Density Lithium-Ion Batteries: Bulk or Surface Degradation?, *Chem. Mater.*, 2018, **30**, 1155–1163.

152 H. H. Sun, H. H. Ryu, U. H. Kim, J. A. Weeks, A. Heller, Y. K. Sun and C. B. Mullins, Beyond Doping and Coating: Prospective Strategies for Stable High-Capacity Layered Ni-Rich Cathodes, *ACS Energy Lett.*, 2020, **5**, 1136–1146.

153 Y. S. Kang, S. Y. Park, K. Ito, Y. Kubo, Y. Shin, D. Y. Kim, D. H. Seo, S. Kim, J. H. Park, S. G. Doo, M. Koh, J. A. Seo and K. Park, Revealing the Structural Degradation Mechanism of the Ni-rich Cathode Surface: How Thick is the Surface?, *J. Power Sources*, 2021, **490**, 229542.

154 E. Trevisanello, R. Ruess, G. Conforto, F. H. Richter and J. Janek, Polycrystalline and Single Crystalline NCM Cathode Materials—Quantifying Particle Cracking, Active Surface Area, and Lithium Diffusion, *Adv. Energy Mater.*, 2021, **11**, 2003400.

155 H. J. Noh, S. Youn, C. S. Yoon and Y. K. Sun, Comparison of the Structural and Electrochemical Properties of Layered  $\text{Li}[\text{Ni}_x\text{Co}_y\text{Mn}_z]\text{O}_2$  ( $x = 1/3, 0.5, 0.6, 0.7, 0.8$  and  $0.85$ ) Cathode Material for Lithium-ion batteries, *J. Power Sources*, 2013, **233**, 121–130.

156 K. Chen, W. Cai, Z. Hu, Q. Huang, A. Wang, Z. Zeng, J. Song, Y. Sun, Q. Kong, W. Feng, T. Chen, Z. Wu, Y. Song, X. Guo, X. Guo and T. Chen, Damage Mechanisms and Recent Research Advances in Ni-rich Layered Cathode Materials for Lithium-ion Batteries, *Electron.*, 2024, **2**, e27.

157 J. Cui, X. Ding, D. Luo, H. Xie, Z. Zhang, B. Zhang, F. Tan, C. Liu and Z. Lin, Effect of Cationic Uniformity in Precursors on Li/Ni Mixing of Ni-Rich Layered Cathodes, *Energy Fuels*, 2021, **35**, 1842–1850.

158 Z. Chen, J. Li and X. C. Zeng, Unraveling Oxygen Evolution in Li-Rich Oxides: A Unified Modeling of the Intermediate Peroxo/Superoxo-like Dimers, *J. Am. Chem. Soc.*, 2019, **141**, 10751–10759.

159 H. Chen and M. S. Islam, Lithium Extraction Mechanism in Li-Rich  $\text{Li}_2\text{MnO}_3$  Involving Oxygen Hole Formation and Dimerization, *Chem. Mater.*, 2016, **28**, 6656–6663.

160 J. Li, Z. Liu, Y. Wang and R. Wang, Investigation of facial  $\text{B}_2\text{O}_3$  Surface Modification Effect on the Cycling Stability and High-rate Capacity of  $\text{LiNi}_{1/3}\text{Co}_{1/3}\text{Mn}_{1/3}\text{O}_2$  Cathode, *J. Alloys Compd.*, 2020, **834**, 155150.

161 R. Shunmugasundaram, R. Senthil Arumugam and J. R. Dahn, High Capacity li-rich Positive Electrode Materials with Reduced First-cycle Irreversible Capacity Loss, *Chem. Mater.*, 2015, **27**, 757–767.

162 Z. Lu and J. R. Dahn, Understanding the Anomalous Capacity of  $\text{Li}/\text{Li}[\text{Ni}_x\text{Li}_{(1/3-2x/3)}\text{Mn}_{(2/3-x/3)}]\text{O}_2$  Cells Using In situ X-ray Diffraction and Electrochemical Studies, *J. Electrochem. Soc.*, 2002, **149**, A815–A822.

163 R. A. House, G. J. Rees, M. A. Pérez-Osorio, J. J. Marie, E. Boivin, A. W. Robertson, A. Nag, M. Garcia-Fernandez, K. J. Zhou and P. G. Bruce, First-cycle Voltage Hysteresis in Li-Rich 3d Cathodes Associated with Molecular  $\text{O}_2$  Trapped in the Bulk, *Nat. Energy*, 2020, **5**, 777–785.

164 Q. Li, D. Ning, D. Wong, K. An, Y. Tang, D. Zhou, G. Schuck, Z. Chen, N. Zhang and X. Liu, Improving the Oxygen Redox Reversibility of Li-rich Battery Cathode Materials via Coulombic Repulsive Interactions Strategy, *Nat. Commun.*, 2022, **13**, 1–13.

165 S. Tao, W. Huang, S. Chu, B. Qian, L. Liu and W. Xu, Dynamic Structural Evolution of Oxygen Vacancies in Lithium rich layered Composites Cathodes for Li-Ion Batteries, *Mater. Today Phys.*, 2021, **18**, 100403.

166 M. Gu, I. Belharouak, J. Zheng, H. Wu, J. Xiao, A. Genc, K. Amine, S. Thevuthasan, D. R. Baer, J. G. Zhang, N. D. Browning, J. Liu and C. Wang, Formation of the Spinel Phase in the Layered Composite Cathode Used in Li-Ion Batteries, *ACS Nano*, 2013, **7**, 760–767.



167 T. Kawamura, A. Kimura, M. Egashira, S. Okada and J. I. Yamaki, Thermal Stability of Alkyl Carbonate Mixed-solvent Electrolytes for Lithium-Ion Cells, *J. Power Sources*, 2002, **104**, 260–264.

168 J. H. Kim, N. P. W. Pieczonka, Z. Li, Y. Wu, S. Harris and B. R. Powell, Understanding the Capacity Fading Mechanism in  $\text{LiNi}_{0.5}\text{Mn}_{1.5}\text{O}_4$ /graphite Li-Ion Batteries, *Electrochim. Acta*, 2013, **90**, 556–562.

169 H. H. Ryu, K. J. Park, C. S. Yoon and Y. K. Sun, Capacity fading of ni-rich  $\text{Li}[\text{Ni}_x\text{Co}_y\text{Mn}_{1-x-y}]\text{O}_2$  ( $0.6 \leq x \leq 0.95$ ) Cathodes for High-Energy-Density Lithium-Ion Batteries: Bulk or Surface Degradation?, *Chem. Mater.*, 2018, **30**, 1155–1163.

170 H. Wang, F. Liu, R. Yu, Z. Xiao, Z. Zhu, L. Zhou and J. Wu, Co-gradient Li-rich Cathode Relieving the Capacity Decay in Lithium-ion Batteries, *Nano Energy*, 2022, **100**, 107439.

171 B. Liang, Y. Liu and Y. Xu, Silicon-based Materials as High-Capacity Anodes for Next Generation Lithium-ion Batteries, *J. Power Sources*, 2014, **267**, 469–490.

172 A. Ulvestad, A. H. Reksten, H. F. Andersen, P. A. Carvalho, I. J. T. Jensen, M. U. Nagell, J. P. Mæhlen, M. Kirkengen and A. Y. Koposov, Crystallinity of Silicon Nanoparticles: Direct Influence on the Electrochemical Performance of Lithium-Ion Battery Anodes, *ChemElectroChem*, 2020, **7**, 4349–4353.

173 G. M. Veith, L. Baggetto, R. L. Sacci, R. R. Unocic, W. E. Tenhaeff and J. F. Browning, Direct Measurement of the Chemical Reactivity of Silicon Electrodes with  $\text{LiPF}_6$ -based Battery Electrolytes, *Chem. Commun.*, 2014, **50**, 3081–3084.

174 J. W. Choi and D. Aurbach, Promise and Reality of Post-Lithium-ion Batteries with High Energy Densities, *Nat. Rev. Mater.*, 2016, **1**, 16013.

175 X. Wang, Y. Tan, W. Wang and Y. Sun, Over-Lithiation Regulation of Silicon-Based Anodes for High-Energy Lithium-Ion batteries, *ChemSusChem*, 2024, **33**, 2001358.

176 J. K. Seo, H. M. Cho, K. Takahara, K. W. Chapman, O. J. Borkiewicz, M. Sina and Y. Shirley Meng, Revisiting the Conversion Reaction Voltage and the Reversibility of the  $\text{CuF}_2$  Electrode in Li-Ion Batteries, *Nano Res.*, 2017, **10**, 4232–4244.

177 Q. Huang, K. Turcheniuk, X. Ren, A. Magasinski, A. Y. Song, Y. Xiao, D. Kim and G. Yushin, Cycle Stability of Conversion-type Iron Fluoride Lithium Battery Cathode at Elevated Temperatures in Polymer Electrolyte Composites, *Nat. Mater.*, 2019, **18**, 1343–1349.

178 F. Wu and G. Yushin, Conversion Cathodes for Rechargeable Lithium and Lithium-Ion Batteries, *Energy Environ. Sci.*, 2017, **10**, 435–459.

179 M. T. McDowell, Z. Lu, K. J. Koski, J. H. Yu, G. Zheng and Y. Cui, In situ Observation of Divergent Phase Transformations in Individual Sulfide Nanocrystals, *Nano Lett.*, 2015, **15**, 1264–1271.

180 T. Li, Z. X. Chen, Y. L. Cao, X. P. Ai and H. X. Yang, Transition-metal Chlorides as Conversion Cathode Materials for Li-ion Batteries, *Electrochim. Acta*, 2012, **68**, 202–205.

181 B. Shao, S. Tan, Y. Huang, L. Zhang, J. Shi, X. Q. Yang, E. Hu and F. Han, Enabling Conversion-Type Iron Fluoride Cathode by Halide-Based Solid Electrolyte, *Adv. Funct. Mater.*, 2022, **32**, 2206845.

182 D. S. Ashby, J. S. Horner, G. Whang, A. S. Lapp, S. A. Roberts, B. Dunn, I. V. Kolesnichenko, T. N. Lambert and A. A. Talin, Understanding the Electrochemical Performance of  $\text{FeS}_2$  Conversion Cathodes, *ACS Appl. Mater. Interfaces*, 2022, **14**, 26604–26611.

183 V. A. Sethuraman, L. J. Hardwick, V. Srinivasan and R. Kostecki, Surface Structural Disordering in Graphite Upon Lithium Intercalation/Deintercalation, *J. Power Sources*, 2010, **195**, 3655–3660.

184 H. Michael, F. Iacoviello, T. M. M. Heenan, A. Llewellyn, J. S. Weaving, R. Jervis, D. J. L. Brett and P. R. Shearing, A Dilatometric Study of Graphite Electrodes During Cycling with X-Ray Computed Tomography, *J. Electrochem. Soc.*, 2021, **168**, 010507.

185 M. Ko, S. Jayasubramaniyan, S. Kim, J. Kim, D. Kim, N. S. Reddy, H. Ma, S. Y. Nam and J. Sung, Surface Fluorinated Graphite Suppressing the Lithium Dendrite Formation for Fast Chargeable Lithium-ion Batteries, *Carbon*, 2024, **219**, 118808.

186 Y. Liu, Y. Zhu and Y. Cui, Challenges and Opportunities Towards Fast-charging Battery Materials, *Nat. Energy*, 2019, **4**, 540–550.

187 D. E. Brown, E. J. McShane, Z. M. Konz, K. B. Knudsen and B. D. McCloskey, Detecting onset of Lithium Plating During Fast Charging of Li-ion Batteries using Operando Electrochemical Impedance Spectroscopy, *Cell. Rep. Phys. Sci.*, 2021, **2**, 100589.

188 F. Wu, Y. X. Yuan, X. B. Cheng, Y. Bai, Y. Li, C. Wu and Q. Zhang, Perspectives for Restraining Harsh Lithium Dendrite Growth: Towards Robust Lithium Metal Anodes, *Energy Storage Mater.*, 2018, **15**, 148–170.

189 X. Xu, S. Wang, H. Wang, C. Hu, Y. Jin, J. Liu and H. Yan, Recent Progresses in The Suppression Method Based on the Growth Mechanism of Lithium Dendrite, *J. Energy Chem.*, 2018, **27**, 513–527.

190 K. N. Wood, M. Noked and N. P. Dasgupta, Lithium Metal Anodes: Toward an Improved Understanding of Coupled Morphological, Electrochemical, And Mechanical Behavior, *ACS Energy Lett.*, 2017, **2**, 664–672.

191 X. Meng, Y. Xu, H. Cao, X. Lin, P. Ning, Y. Zhang, Y. G. Garcia and Z. Sun, Internal Failure of Anode Materials for Lithium Batteries—A Critical Review, *Green Energy Environ.*, 2020, **5**, 22–36.

192 X. Han, H. Zhong, K. Li, X. Xue, W. Wu, N. Hu, X. Lu, J. Huang, G. Xiao, Y. Mai and T. Guo, Operando Monitoring of Dendrite Formation In Lithium Metal Batteries Via Ultrasensitive Tilted Fiber Bragg Grating Sensors, *Light: Sci. Appl.*, 2024, **13**, 1–14.

193 D. Wang, Y. Liu, G. Li, C. Qin, L. Huang, Y. Wu, D. Wang, Y. Liu, G. Li, C. Qin, L. Huang and Y. Wu, Liquid Metal



Welding to Suppress Li Dendrite by Equalized Heat Distribution, *Adv. Funct. Mater.*, 2021, **31**, 2106740.

194 F.-N. Jiang, S.-J. Yang, H. Liu, X.-B. Cheng, L. Liu, R. Xiang, Q. Zhang, S. Kaskel and J.-Q. Huang, Mechanism Understanding for Stripping Electrochemistry of Li Metal Anode, *SusMat.*, 2021, **1**, 506–536.

195 H. Hong, N. A. R. Che Mohamad, K. Chae, F. Marques Mota and D. H. Kim, The Lithium Metal Anode in Li-S Batteries: Challenges and Recent Progress, *J. Mater. Chem. A*, 2021, **9**, 10012–10038.

196 Y. Xiang, M. Tao, X. Chen, P. Shan, D. Zhao, J. Wu, M. Lin, X. Liu, H. He, W. Zhao, Y. Hu, J. Chen, Y. Wang and Y. Yang, Gas Induced Formation of Inactive Li in Rechargeable Lithium Metal Batteries, *Nat. Commun.*, 2023, **14**, 177.

197 Y. Liu, W. Wang, J. Chen, X. Li, Q. Cheng and G. Wang, Fabrication of Porous Lithium Titanate Self-supporting Anode for High Performance Lithium-ion Capacitor, *J. Energy Chem.*, 2020, **50**, 344–350.

198 D. Wang, H. Liu, M. Li, X. Wang, S. Bai, Y. Shi, J. Tian, Z. Shan, Y. S. Meng, P. Liu and Z. Chen, Nanosheet-assembled Hierarchical  $\text{Li}_4\text{Ti}_5\text{O}_{12}$  Microspheres for High-volumetric-density and High-rate Li-ion Battery Anode, *Energy Storage Mater.*, 2019, **21**, 361–371.

199 T. Bank, L. Alsheimer, N. Löffler, D. U. Sauer, T. Bank, L. Alsheimer, N. Löffler and D. U. Sauer, State of Charge Dependent Degradation Effects of Lithium Titanate Oxide Batteries at Elevated Temperatures: An In Situ and Ex Situ Analysis, *J. Energy Storage*, 2022, **51**, 104201.

200 S. Liu, M. Winter, M. Lewerenz, J. Becker, D. U. Sauer, Z. Ma and J. Jiang, Analysis of Cyclic Aging Performance of Commercial  $\text{Li}_4\text{Ti}_5\text{O}_{12}$ -based batteries at room temperature, *Energy*, 2019, **173**, 1041–1053.

201 R. J. Cava, D. W. Murphy and S. M. Zahurak, Lithium Insertion in Wadsley–Roth Phases Based on Niobium Oxide, *J. Electrochem. Soc.*, 1983, **130**, 2345.

202 A. F. Fuentes, E. B. Garza, A. M. De La Cruz and L. M. Torres-Martínez, Lithium and Sodium Insertion in  $\text{W}_3\text{Nb}_{14}\text{O}_{44}$ , a Block Structure Type Phase, *Solid State Ionics*, 1997, **93**, 245–253.

203 A. F. Fuentes, A. M. De La Cruz and L. M. Torres-Martínez, A study of Lithium Insertion in  $\text{W}_4\text{Nb}_{26}\text{O}_{77}$ : Synthesis and Characterization of New Phases, *Solid State Ionics*, 1996, **92**, 103–111.

204 X. Wu, J. Miao, W. Han, Y. S. Hu, D. Chen, J. S. Lee, J. Kim and L. Chen, Investigation on  $\text{Ti}_2\text{Nb}_{10}\text{O}_{29}$  Anode Material for Lithium-Ion Batteries, *Electrochem. Commun.*, 2012, **25**, 39–42.

205 K. J. Griffith, K. M. Wiaderek and G. Cibin, L.E. Marbella and C.P. Grey, Niobium Tungsten Oxides for High-Rate Lithium-Ion Energy Storage, *Nature*, 2018, **559**, 556–563.

206 X. Zhu, Q. Fu, L. Tang, C. Lin, J. Xu, G. Liang, R. Li, L. Luo and Y. Chen,  $\text{Mg}_2\text{Nb}_{34}\text{O}_{87}$ , Porous Microspheres for Use in High-Energy, Safe, Fast-Charging, and Stable Lithium-Ion Batteries, *ACS Appl. Mater. Interfaces*, 2018, **10**, 23711–23720.

207 X. Zhu, J. Xu, Y. Luo, Q. Fu, G. Liang, L. Luo, Y. Chen, C. Lin and X. S. Zhao,  $\text{MoNb}_{12}\text{O}_{33}$  as a New Anode Material for High-Capacity, Safe, Rapid and Durable  $\text{Li}^+$  Storage: Structural Characteristics, Electrochemical Properties and Working mechanisms, *J. Mater. Chem. A*, 2019, **7**, 6522–6532.

208 D. W. Murphy, M. Greenblatt, R. J. Cava and S. M. Zahurak, Topotactic Lithium Reactions with  $\text{ReO}_3$  Related Shear Structures, *Solid State Ionics*, 1981, **5**, 327–329.

209 X. Ding, Q. Zhou, X. Li and X. Xiong, Fast-Charging Anodes for Lithium Ion Batteries: Progress and Challenges, *Chem. Commun.*, 2024, **60**, 2472–2488.

210 Y. Sheng, Y. Wang, S. Yin, L. Zhao, X. Zhang, D. Liu and G. Wen, Niobium-Based Oxide for Anode Materials for Lithium-Ion Batteries, *Chem. – Eur. J.*, 2024, **30**, e202302865.

211 X. Wu, S. Lou, X. Cheng, C. Lin, J. Gao, Y. Ma, P. Zuo, C. Du, Y. Gao and G. Yin, Unravelling the Interface Layer Formation and Gas Evolution/Suppression on a  $\text{TiNb}_2\text{O}_7$  Anode for Lithium-Ion Batteries, *ACS Appl. Mater. Interfaces*, 2018, **10**, 27056–27062.

212 T. Yuan, L. Soule, B. Zhao, J. Zou, J. Yang, M. Liu and S. Zheng, Recent Advances in Titanium Niobium Oxide Anodes for High-Power Lithium-Ion Batteries, *Energy Fuels*, 2020, **34**, 13321–13334.

213 L. Buannic, J. F. Colin, M. Chapuis, M. Chakir and S. Patoux, Electrochemical Performances and Gassing Behavior of High Surface Area Titanium Niobium Oxides, *J. Mater. Chem. A*, 2016, **4**, 11531–11541.

214 S. J. Gross, M. T. Hsieh, D. R. Mumm, L. Valdevit and A. Mohraz, Alleviating Expansion-Induced Mechanical Degradation in Lithium-Ion battery Silicon Anodes via Morphological Design, *Extreme Mech. Lett.*, 2022, **54**, 101746.

215 A. Šimek, T. Kazda, J. Báňa and O. Čech, Basic Method for Water Detection in  $\text{LiPF}_6$ -Based Electrolytes, *Monatsh. Chem.*, 2024, **155**, 313–317.

216 S. E. Sloop, J. K. Pugh, S. Wang, J. B. Kerr and K. Kinoshita, Chemical Reactivity of  $\text{PF}_5$  and  $\text{LiPF}_6$  in Ethylene Carbonate/Dimethyl Carbonate Solutions, *Electrochem. Solid-State Lett.*, 2001, **4**, A42.

217 J.-G. Han, K. Kim, Y. Lee and N.-S. Choi, Scavenging Materials to Stabilize  $\text{LiPF}_6$ -Containing Carbonate-Based Electrolytes for Li-Ion Batteries, *Adv. Mater.*, 2019, **31**, 1804822.

218 G. G. Eshetu, J. P. Bertrand, A. Lecocq, S. Grugeon, S. Laruelle, M. Armand and G. Marlair, Fire behavior of carbonates-based electrolytes used in Li-ion rechargeable batteries with a focus on the role of the  $\text{LiPF}_6$  and LiFSI salts, *J. Power Sources*, 2014, **269**, 804–811.

219 C. Sångeland, B. Sun, D. Brandell, E. J. Berg and J. Mindemark, Decomposition of Carbonate-Based Electrolytes: Differences and Peculiarities for Liquids vs. Polymers Observed Using Operando Gas Analysis, *Batteries Supercaps*, 2021, **4**, 785–790.

220 I. S. Buyuker, B. Pei, H. Zhou, X. Cao, Z. Yu, S. Liu, W. Zhang, W. Xu, J. G. Zhang, Z. Bao, Y. Cui, C. Wang and M. S. Whittingham, Voltage and Temperature Limits



of Advanced Electrolytes for Lithium-Metal Batteries, *ACS Energy Lett.*, 2023, **8**, 1735–1743.

221 S. Di Tommaso, P. Rotureau and C. Adamo, Oxidation Mechanism of Aliphatic Ethers: Theoretical Insights on The Main Reaction Channels, *J. Phys. Chem. A*, 2012, **116**, 9010–9019.

222 J. Xiang and Y. C. Lu, Ether-Based High-Voltage Lithium Metal Batteries: The Road to Commercialization, *ACS Nano*, 2024, **18**, 10726–10737.

223 Y. Zhao, T. Zhou, M. Mensi, J. W. Choi and A. Coskun, Electrolyte Engineering via Ether Solvent Fluorination for Developing Stable Non-Aqueous Lithium Metal Batteries, *Nat. Commun.*, 2023, **14**, 299.

224 Y. Huang, R. Li, S. Weng, H. Zhang, C. Zhu, D. Lu, C. Sun, X. Huang, T. Deng, L. Fan, L. Chen, X. Wang and X. Fan, Eco-friendly Electrolytes via a Robust Bond Design for High-energy Li Metal Batteries, *Energy Environ. Sci.*, 2022, **15**, 4349–4361.

225 D. Di Lecce, V. Marangon, H. G. Jung, Y. Tominaga, S. Greenbaum and J. Hassoun, Glyme-Based Electrolytes: Suitable Solutions for Next-generation Lithium Batteries, *Green Chem.*, 2022, **24**, 1021–1048.

226 M. C. Long, T. Wang, P. H. Duan, Y. Gao, X. L. Wang, G. Wu and Y. Z. Wang, Thermotolerant and Fireproof Gel Polymer Electrolyte Toward High-Performance and Safe Lithium-Ion Battery, *J. Energy Chem.*, 2022, **65**, 9–18.

227 X. Liu, C. Zhang, S. Gao, S. Cai, Q. Wang, J. Liu and Z. Liu, A Novel Polyphosphonate Flame-Retardant Additive Towards Safety-Reinforced All-Solid-State Polymer Electrolyte, *Mater. Chem. Phys.*, 2020, **239**, 122014.

228 W. Q. Walker, K. Cooper, P. Hughes, I. Doemling, M. Akhnoukh, S. Taylor, J. Darst, J. Billman, M. Sharp, D. Petrushenko, R. Owen, M. Pham, T. Heenan, A. Rack, O. Magdysuk, T. Connolley, D. Brett, P. Shearing, D. Finegan and E. Darcy, The Effect Of Cell Geometry And Trigger Method on The Risks Associated With Thermal Runaway of Lithium-Ion Batteries, *J. Power Sources*, 2022, **524**, 230645.

229 D. P. Finegan, B. Tjaden, T. M. M. Heenan, R. Jervis, M. Di Michiel, A. Rack, G. Hinds, D. J. L. Brett and P. R. Shearing, Tracking Internal Temperature and Structural Dynamics during Nail Penetration of Lithium-Ion Cells, *J. Electrochem. Soc.*, 2017, **164**, A3285–A3291.

230 S. Huang, X. Du, M. Richter, J. Ford, G. M. Cavalheiro, Z. Du, R. T. White and G. Zhang, Understanding Li-Ion Cell Internal Short Circuit and Thermal Runaway through Small, Slow and In Situ Sensing Nail Penetration, *J. Electrochem. Soc.*, 2020, **167**, 090526.

231 M. Yang, M. Rong, Y. Ye, Y. Zhang, A. Yang, J. Chu, H. Yuan and X. Wang, A Comprehensive Study of Thermal Runaway Behavior and Early Warning Subjected to Internal Short-Circuit, *J. Power Sources*, 2024, **620**, 235213.

232 K. C. Chiu, C. H. Lin, S. F. Yeh, Y. H. Lin and K. C. Chen, An Electrochemical Modeling of Lithium-Ion Battery Nail Penetration, *J. Power Sources*, 2014, **251**, 254–263.

233 R. Zhao, J. Liu and J. Gu, A Comprehensive Study on Li-Ion Battery Nail Penetrations and The Possible Solutions, *Energy*, 2017, **123**, 392–401.

234 D. P. Finegan, M. Scheel, J. B. Robinson, B. Tjaden, M. Di Michiel, G. Hinds, D. J. L. Brett and P. R. Shearing, Investigating Lithium-Ion Battery Materials During Overcharge-Induced Thermal Runaway: An Operando and Multi-Scale X-Ray CT Study, *Phys. Chem. Chem. Phys.*, 2016, **18**, 30912–30919.

235 C. J. Wang, Y. L. Zhu, F. Gao, C. Qi, P. L. Zhao, Q. F. Meng, J. Y. Wang and Q. B. Wu, Thermal Runaway Behavior and Features of LiFePO<sub>4</sub>/Graphite Aged Batteries Under Overcharge, *Int. J. Energy Res.*, 2020, **44**, 5477–5487.

236 G. Zhang, X. Wei, S. Chen, J. Zhu, G. Han, X. Tang, W. Hua, H. Dai and J. Ye, Comprehensive Investigation of a Slight Overcharge on Degradation and Thermal Runaway Behavior of Lithium-Ion Batteries, *ACS Appl. Mater. Interfaces*, 2021, **13**, 35054–35068.

237 Y. Zhou, X. Zhu, Z. Wang, T. Shan, J. Zhang and Z. Sun, Safety Assessment of Thermal Runaway Behavior of Lithium-Ion Cells with Actual Installed State, *Appl. Therm. Eng.*, 2023, **229**, 120617.

238 J. Wang, Y. Li, F. Liu, Z. Fang, N. Gu, B. Chen, N. Yang and Y. Jia, A Comparative Study of Overcharge Thermal Runaway Force-Electrical-Thermal Characteristics and Safety Assessment of Lithium Batteries with Different Cathode Materials, *Appl. Therm. Eng.*, 2024, **256**, 124092.

239 L. Huang, Z. Zhang, Z. Wang, L. Zhang, X. Zhu and D. D. Dorrell, Thermal Runaway Behavior During Overcharge for Large-Format Lithium-Ion Batteries with Different Packaging Patterns, *J. Energy Storage*, 2019, **25**, 100811.

240 J. Ye, H. Chen, Q. Wang, P. Huang, J. Sun and S. Lo, Thermal Behavior and Failure Mechanism of Lithium Ion Cells During Overcharge Under Adiabatic Conditions, *Appl. Energy*, 2016, **182**, 464–474.

241 X. Zhu, Z. Wang, Y. Wang, H. Wang, C. Wang, L. Tong and M. Yi, Overcharge Investigation of Large Format Lithium-Ion Pouch Cells with Li(Ni<sub>0.6</sub>Co<sub>0.2</sub>Mn<sub>0.2</sub>)O<sub>2</sub> Cathode for Electric Vehicles: Thermal Runaway Features and Safety Management Method, *Energy*, 2019, **169**, 868–880.

242 C. Qi, Y. Zhu, F. Gao, K. Yang and Q. Jiao, Mathematical Model for Thermal Behavior of Lithium-Ion Battery Pack Under Overcharge, *Int. J. Heat Mass. Transfer*, 2018, **124**, 552–563.

243 W. Mei, L. Zhang, J. Sun and Q. Wang, Experimental and Numerical Methods to Investigate the Overcharge Caused Lithium Plating for Lithium Ion Battery, *Energy Storage Mater.*, 2020, **32**, 91–104.

244 L. Liu, X. Feng, C. Rahe, W. Li, L. Lu, X. He, D. U. Sauer and M. Ouyang, Internal Short Circuit Evaluation and Corresponding Failure Mode Analysis for Lithium-Ion Batteries, *J. Energy Chem.*, 2021, **61**, 269–280.

245 Q. Wu, L. Yang, N. Li, Y. Chen, Q. Wang, W. L. Song, X. Feng, Y. Wei and H. Sen Chen, In-Situ Thermography Revealing the Evolution of Internal Short Circuit of Lithium-Ion Batteries, *J. Power Sources*, 2022, **540**, 231602.



246 X. Liu, Z. Zhou, W. Wu, L. Gao, Y. Li, H. Huang, Z. Huang, Y. Li and Y. Song, Three-Dimensional Modeling for the Internal Shorting Caused Thermal Runaway Process in 20 A h Lithium-Ion Battery, *Energies*, 2022, **15**, 6868.

247 D. P. Finegan, E. Darcy, M. Keyser, B. Tjaden, T. M. M. Heenan, R. Jervis, J. J. Bailey, R. Malik, N. T. Vo, O. V. Magdysyuk, R. Atwood, M. Drakopoulos, M. DiMichiel, A. Rack, G. Hinds, D. J. L. Brett and P. R. Shearing, Characterising Thermal Runaway Within Lithium-Ion Cells By Inducing and Monitoring Internal Short Circuits, *Energy Environ. Sci.*, 2017, **10**, 1377–1388.

248 S. Huang, Z. Du, Q. Zhou, K. Snyder, S. Liu and G. Zhang, In Situ Measurement of Temperature Distributions in a Li-Ion Cell during Internal Short Circuit and Thermal Runaway, *J. Electrochem. Soc.*, 2021, **168**, 090510.

249 L. Liu, X. Feng, M. Zhang, L. Lu, X. Han, X. He and M. Ouyang, Comparative Study on Substitute Triggering Approaches for Internal Short Circuit in Lithium-Ion Batteries, *Appl. Energy*, 2020, **259**, 114143.

250 J. Xu, Y. Wu and S. Yin, Investigation of Effects of Design Parameters on the Internal Short-Circuit in Cylindrical Lithium-Ion Batteries, *RSC Adv.*, 2017, **7**, 14360–14371.

251 Z. An, Y. Zhao, X. Du, T. Shi and D. Zhang, Experimental Research on Thermal-Electrical Behavior and Mechanism During External Short Circuit for LiFePO<sub>4</sub> Li-Ion Battery, *Appl. Energy*, 2023, **332**, 120519.

252 Z. Zeng, X. An, C. Peng, X. Ruan, Z. Song, C. Dang and Z. An, Study on the Thermal Runaway Behavior and Mechanism Of 18 650 Lithium-Ion Battery Induced by External Short Circuit, *Appl. Therm. Eng.*, 2025, **258**, 124569.

253 Z. An, R. Jia, Q. Li, D. Zhang, X. Du, W. Li and T. Shi, Safety of LiFePO<sub>4</sub>/Graphite Li-Ion Pouch Batteries Under Simulated External Short-Circuit (High Rate) Conditions, *J. Power Sources*, 2025, **629**, 236038.

254 Z. An, K. Shah, L. Jia and Y. Ma, Modeling and Analysis of Thermal Runaway in Li-Ion Cell, *Appl. Therm. Eng.*, 2019, **160**, 113960.

255 P. Jindal and J. Bhattacharya, Review—Understanding the Thermal Runaway Behavior of Li-Ion Batteries through Experimental Techniques, *J. Electrochem. Soc.*, 2019, **166**, A2165–A2193.

256 X. Feng, M. Fang, X. He, M. Ouyang, L. Lu, H. Wang and M. Zhang, Thermal Runaway Features of Large Format Prismatic Lithium Ion Battery Using Extended Volume Accelerating Rate Calorimetry, *J. Power Sources*, 2014, **255**, 294–301.

257 J. Liu, Z. Wang, J. Bai, T. Gao and N. Mao, Heat Generation and Thermal Runaway Mechanisms Induced by Overcharging of Aged Lithium-Ion Battery, *Appl. Therm. Eng.*, 2022, **212**, 118565.

258 D. Ren, X. Liu, X. Feng, L. Lu, M. Ouyang, J. Li and X. He, Model-Based Thermal Runaway Prediction of Lithium-Ion Batteries from Kinetics Analysis of Cell Components, *Appl. Energy*, 2018, **228**, 633–644.

259 D. Patel, J. B. Robinson, S. Ball, D. J. L. Brett and P. R. Shearing, Thermal Runaway of a Li-Ion Battery Studied by Combined ARC and Multi-Length Scale X-ray CT, *J. Electrochem. Soc.*, 2020, **167**, 090511.

260 A. Kvasha, C. Gutiérrez, U. Osa, I. de Meatza, J. A. Blazquez, H. Macicior and I. Urdampilleta, A Comparative Study of Thermal Runaway of Commercial Lithium-Ion Cells, *Energy*, 2018, **159**, 547–557.

261 X. Feng, S. Zheng, D. Ren, X. He, L. Wang, H. Cui, X. Liu, C. Jin, F. Zhang, C. Xu, H. Hsu, S. Gao, T. Chen, Y. Li, T. Wang, H. Wang, M. Li and M. Ouyang, Investigating the Thermal Runaway Mechanisms of Lithium-Ion Batteries Based on Thermal Analysis Database, *Appl. Energy*, 2019, **246**, 53–64.

262 L. Yuan, T. Dubaniewicz, I. Zlochower, R. Thomas and N. Rayyan, Experimental Study On Thermal Runaway and Vented Gases of Lithium-Ion Cells, *Process Saf. Environ. Prot.*, 2020, **144**, 186–192.

263 W. Q. Walker, G. A. Bayles, K. L. Johnson, R. P. Brown, D. Petrushenko, P. J. Hughes, D. T. Calderon, J. J. Darst, R. A. Hagen, B. A. Sakowski, J. P. Smith, K. I. Poast, E. C. Darcy and S. L. Rickman, Evaluation of Large-Format Lithium-Ion Cell Thermal Runaway Response Triggered by Nail Penetration using Novel Fractional Thermal Runaway Calorimetry and Gas Collection Methodology, *J. Electrochem. Soc.*, 2022, **169**, 060535.

264 E. Jiaqiang, H. Xiao, S. Tian and Y. Huang, A Comprehensive Review on Thermal Runaway Model of a Lithium-Ion Battery: Mechanism, Thermal, Mechanical, Propagation, Gas Venting and Combustion, *Renewable Energy*, 2024, **229**, 120762.

265 Z. Jia, S. Wang, P. Qin, C. Li, L. Song, Z. Cheng, K. Jin, J. Sun and Q. Wang, Comparative Investigation of the Thermal Runaway and Gas Venting Behaviors of Large-Format LiFePO<sub>4</sub> Batteries Caused by Overcharging and Overheating, *J. Energy Storage*, 2023, **61**, 106791.

266 J. K. Ostanek, W. Li, P. P. Mukherjee, K. R. Crompton and C. Hacker, Simulating Onset and Evolution of Thermal Runaway in Li-Ion Cells Using a Coupled Thermal and Venting Model, *Appl. Energy*, 2020, **268**, 114972.

267 J. Kim, A. Mallarapu, D. P. Finegan and S. Santhanagopalan, Modeling Cell Venting and Gas-Phase Reactions In 18 650 Lithium-Ion Batteries During Thermal Runaway, *J. Power Sources*, 2021, **489**, 229496.

268 B. Mao, C. Fear, H. Chen, H. Zhou, C. Zhao, P. P. Mukherjee, J. Sun and Q. Wang, Experimental and Modeling Investigation on the Gas Generation Dynamics of Lithium-Ion Batteries During Thermal Runaway, *eTransportation*, 2023, **15**, 100212.

269 J. H. Lee, C. S. Yoon, J. Y. Hwang, S. J. Kim, F. Maglia, P. Lamp, S. T. Myung and Y. K. Sun, High-Energy-Density Lithium-Ion Battery Using a Carbon-Nanotube-Si Composite Anode and a Compositionally Graded Li[Ni<sub>0.85</sub>Co<sub>0.05</sub>Mn<sub>0.10</sub>]O<sub>2</sub> Cathode, *Energy Environ. Sci.*, 2016, **9**, 2152–2158.

270 J. U. Choi, N. Voronina, Y.-K. Sun, S.-T. Myung, J. U. Choi, N. Voronina, S.-T. Myung and Y.-K. Sun, Recent Progress and Perspective of Advanced High-Energy Co-Less Ni-Rich



Cathodes for Li-Ion Batteries: Yesterday, Today, and Tomorrow, *Adv. Energy Mater.*, 2020, **10**, 202002027.

271 B. B. Lim, S. T. Myung, C. S. Yoon and Y. K. Sun, Comparative Study of Ni-Rich Layered Cathodes for Rechargeable Lithium Batteries:  $\text{Li}[\text{Ni}_{0.85}\text{Co}_{0.11}\text{Al}_{0.04}]\text{O}_2$  and  $\text{Li}[\text{Ni}_{0.84}\text{Co}_{0.06}\text{Mn}_{0.09}\text{Al}_{0.01}]\text{O}_2$  with Two-Step Full Concentration Gradients, *ACS Energy Lett.*, 2016, **1**, 283–289.

272 Y. K. Sun, B. R. Lee, H. J. Noh, H. Wu, S. T. Myung and K. Amine, A Novel Concentration-Gradient  $\text{Li}[\text{Ni}_{0.83}\text{Co}_{0.07}\text{Mn}_{0.10}]\text{O}_2$  Cathode Material for High-Energy Lithium-Ion Batteries, *J. Mater. Chem.*, 2011, **21**, 10108–10112.

273 Y. K. Sun, D. H. Kim, C. S. Yoon, S. T. Myung, J. Prakash and K. Amine, A Novel Cathode Material with a Concentration-Gradient for High-Energy and Safe Lithium-Ion Batteries, *Adv. Funct. Mater.*, 2010, **20**, 485–491.

274 L. Britala, M. Marinaro and G. Kucinskis, A Review of the Degradation Mechanisms of NCM Cathodes And Corresponding Mitigation Strategies, *J. Energy Storage*, 2023, **73**, 108875.

275 C. S. Yoon, K. J. Park, U. H. Kim, K. H. Kang, H. H. Ryu and Y. K. Sun, High-Energy Ni-Rich  $\text{Li}[\text{Ni}_x\text{Co}_y\text{Mn}_{1-x-y}]\text{O}_2$  Cathodes via Compositional Partitioning for Next-Generation Electric Vehicles, *Chem. Mater.*, 2017, **29**, 10436–10445.

276 T. Wu, X. Liu, X. Zhang, Y. Lu, B. Wang, Q. Deng, Y. Yang, E. Wang, Z. Lyu, Y. Li, Y. Wang, Y. Lyu, C. He, Y. Ren, G. Xu, X. Sun, K. Amine and H. Yu, Full Concentration Gradient-Tailored Li-Rich Layered Oxides for High-Energy Lithium-Ion Batteries, *Adv. Mater.*, 2021, **33**, 2001358.

277 Y. Zhang, B. Tian, Q. Shi, K. K. Yao and M. Xu, Constructing a Li-Gradient in Li-Mn-O Spinel for Long-Life Lithium-Ion Batteries, *Appl. Surf. Sci.*, 2022, **593**, 153410.

278 Y. K. Sun, Z. Chen, H. J. Noh, D. J. Lee, H. G. Jung, Y. Ren, S. Wang, C. S. Yoon, S. T. Myung and K. Amine, Nanosstructured High-Energy Cathode Materials for Advanced Lithium Batteries, *Nat. Mater.*, 2012, **11**, 942–947.

279 H. J. Noh, J. W. Ju and Y. K. Sun, Comparison of Nanorod-Structured  $\text{Li}[\text{Ni}_{0.54}\text{Co}_{0.16}\text{Mn}_{0.30}]\text{O}_2$  with Conventional Cathode Materials for Li-Ion Batteries, *ChemSusChem*, 2014, **7**, 245–252.

280 C. S. Yoon, K. J. Park, U. H. Kim, K. H. Kang, H. H. Ryu and Y. K. Sun, High-Energy Ni-Rich  $\text{Li}[\text{Ni}_x\text{Co}_y\text{Mn}_{1-x-y}]\text{O}_2$  Cathodes via Compositional Partitioning for Next-Generation Electric Vehicles, *Chem. Mater.*, 2017, **29**, 10436–10445.

281 L. Cheng, W. Yang, Y. Zhang, W. Yang, H. Zhou and S. Chen, Concentration-Gradient of Li-Rich Mn-Based Cathode Materials with Enhanced Cycling Retention, *J. Alloys Compd.*, 2024, **976**, 173180.

282 H. J. Noh, J. W. Ju and Y. K. Sun, Comparison of Nanorod-Structured  $\text{Li}[\text{Ni}_{0.54}\text{Co}_{0.16}\text{Mn}_{0.30}]\text{O}_2$  with Conventional Cathode Materials for Li-Ion Batteries, *ChemSusChem*, 2014, **7**, 245–252.

283 Y. K. Sun, Z. Chen, H. J. Noh, D. J. Lee, H. G. Jung, Y. Ren, S. Wang, C. S. Yoon, S. T. Myung and K. Amine, Nanosstructured High-Energy Cathode Materials for Advanced Lithium Batteries, *Nat. Mater.*, 2012, **11**, 942–947.

284 H. H. Sun, J. A. Weeks, A. Heller and C. B. Mullins, Nanorod Gradient Cathode: Preventing Electrolyte Penetration into Cathode Particles, *ACS Appl. Energy Mater.*, 2019, **2**, 6002–6011.

285 H. J. Noh, Z. Chen, C. S. Yoon, J. Lu, K. Amine and Y. K. Sun, Cathode Material with Nanorod Structure – an Application For Advanced High-Energy and Safe Lithium Batteries, *Chem. Mater.*, 2013, **25**, 2109–2115.

286 H. H. Sun, A. Dolocan, J. A. Weeks, A. Heller and C. B. Mullins, Stabilization of a Highly Ni-Rich Layered Oxide Cathode through Flower-Petal Grain Arrays, *ACS Nano*, 2020, **14**, 17142–17150.

287 H. H. Sun, U. H. Kim, J. H. Park, S. W. Park, D. H. Seo, A. Heller, C. B. Mullins, C. S. Yoon and Y. K. Sun, Transition Metal-Doped Ni-Rich Layered Cathode Materials for Durable Li-Ion Batteries, *Nat. Commun.*, 2021, **12**, 6552.

288 H.-H. Ryu, K.-J. Park, D. R. Yoon, A. Aishova, C. S. Yoon, Y.-K. Sun, H.-H. Ryu, K.-J. Park, D. R. Yoon, A. Aishova, C. S. Yoon and Y.-K. Sun,  $\text{Li}[\text{Ni}_{0.9}\text{Co}_{0.09}\text{W}_{0.01}]\text{O}_2$ : A New Type of Layered Oxide Cathode with High Cycling Stability, *Adv. Energy Mater.*, 2019, **9**, 1902698.

289 K.-J. Park, H.-G. Jung, L.-Y. Kuo, P. Kaghazchi, C. S. Yoon, Y.-K. Sun, K.-J. Park, H.-G. Jung, L.-Y. Kuo, P. Kaghazchi, C. S. Yoon and Y.-K. Sun, Improved Cycling Stability of  $\text{Li}[\text{Ni}_{0.90}\text{Co}_{0.05}\text{Mn}_{0.05}]\text{O}_2$  Through Microstructure Modification by Boron Doping for Li-Ion Batteries, *Adv. Energy Mater.*, 2018, **8**, 1801202.

290 H. H. Sun, U. H. Kim, J. H. Park, S. W. Park, D. H. Seo, A. Heller, C. B. Mullins, C. S. Yoon and Y. K. Sun, Transition Metal-Doped Ni-Rich Layered Cathode Materials for Durable Li-Ion Batteries, *Nat. Commun.*, 2021, **12**, 6552.

291 D. Chen, Q. Yu, X. Xiang, M. Chen, Z. Chen, S. Song, L. Xiong, Y. Liao, L. Xing and W. Li, Porous Layered Lithium-Rich Oxide Nanorods: Synthesis and Performances as Cathode of Lithium Ion Battery, *Electrochim. Acta*, 2015, **154**, 83–93.

292 M. Jiang, D. L. Danilov, R. A. Eichel and P. H. L. Notten, A Review of Degradation Mechanisms and Recent Achievements for Ni-Rich Cathode-Based Li-Ion Batteries, *Adv. Energy Mater.*, 2021, **11**, 2103005.

293 D. Hu, Y. Su, L. Chen, N. Li, L. Bao, Y. Lu, Q. Zhang, J. Wang, S. Chen and F. Wu, The Mechanism of Side Reaction Induced Capacity Fading of Ni-Rich Cathode Materials for Lithium Ion Batteries, *J. Energy Chem.*, 2021, **58**, 1–8.

294 Y. Chen, Y. Zhang, B. Chen, Z. Wang and C. Lu, An Approach to Application for  $\text{LiNi}_{0.6}\text{Co}_{0.2}\text{Mn}_{0.2}\text{O}_2$  Cathode Material at High Cutoff Voltage by  $\text{TiO}_2$  Coating, *J. Power Sources*, 2014, **256**, 20–27.

295 Y. Wu, M. Li, W. Wahyudi, G. Sheng, X. Miao, T. D. Anthopoulos, K. W. Huang, Y. Li and Z. Lai, Performance and Stability Improvement of Layered NCM Lithium-Ion Batteries at High Voltage by a Microporous  $\text{Al}_2\text{O}_3$  Sol-Gel Coating, *ACS Omega*, 2019, **4**, 13972–13980.

296 K. Liu, Q. Zhang, S. Dai, W. Li, X. Liu, F. Ding and J. Zhang, Synergistic Effect of F-Doping and LiF Coating on



Improving the High-Voltage Cycling Stability and Rate Capacity of  $\text{LiNi}_{0.5}\text{Co}_{0.2}\text{Mn}_{0.3}\text{O}_2$  Cathode Materials for Lithium-Ion Batteries, *ACS Appl. Mater. Interfaces*, 2018, **10**, 34153–34162.

297 Y. Bai, X. Wang, S. Yang, X. Zhang, X. Yang, H. Shu and Q. Wu, The Effects of  $\text{FePO}_4$ -Coating on High-Voltage Cycling Stability and Rate Capability of  $\text{Li}[\text{Ni}_{0.5}\text{Co}_{0.2}\text{Mn}_{0.3}]\text{O}_2$ , *J. Alloys Compd.*, 2012, **541**, 125–131.

298 N. Owen and Q. Zhang, Investigations of Aluminum Fluoride as a New Cathode Material for Lithium-Ion Batteries, *J. Appl. Electrochem.*, 2017, **47**, 417–431.

299 S. Wang, X. Jia and P. Takyi-Aninakwa, Review—Surface Coatings for Cathodes in Lithium Ion Batteries: From Crystal Structures to Electrochemical Performance, *J. Electrochem. Soc.*, 2022, **169**, 043504.

300 H. Sun, D. Zhu, Y. Chen, C. Xu, L. Huang and H. Yang,  $\text{LaF}_3$  Surface-Modified  $\text{LiCr}_{0.05}\text{Mn}_{1.95}\text{O}_4$  Cathode Material with Improved High-Temperature Performances for Lithium-Ion batteries, *J. Solid State Electrochem.*, 2012, **16**, 2979–2982.

301 S. T. Myung, F. Maglia, K. J. Park, C. S. Yoon, P. Lamp, S. J. Kim and Y. K. Sun, Nickel-Rich Layered Cathode Materials for Automotive Lithium-Ion Batteries: Achievements and Perspectives, *ACS Energy Lett.*, 2017, **2**, 196–223.

302 S. H. Lee, C. S. Yoon, K. Amine and Y. K. Sun, Improvement of Long-Term Cycling Performance of  $\text{Li}[\text{Ni}_{0.8}\text{Co}_{0.15}\text{Al}_{0.05}]\text{O}_2$  by  $\text{AlF}_3$  coating, *J. Power Sources*, 2013, **234**, 201–207.

303 H. Xie, Z. Liang, D. Luo, Y. Zhang, X. Ding, J. Cui, Z. Zhang and Z. Lin, A General Route of Fluoride Coating on the Cyclability Regularity of High-Voltage NCM cathodes, *Chem. Commun.*, 2020, **56**, 12009–12012.

304 K. Wang, Q. Mao, X. Lu, J. Zhang, H. Huang, Y. Gan, X. He, X. Xia, W. Zhang and Y. Xia, Fluorides Coated Ni-rich Cathode Materials with Enhanced Surficial Chemical Stability for Advanced Lithium-Ion Battery, *Sustainable Mater. Technol.*, 2023, **38**, e00713.

305 H. H. Ryu, H. W. Lim, S. G. Lee and Y. K. Sun, Near-Surface Reconstruction in Ni-rich Layered Cathodes for High-Performance Lithium-Ion Batteries, *Nat. Energy*, 2023, **9**, 47–56.

306 J. Zheng, M. Gu, J. Xiao, B. J. Polzin, P. Yan, X. Chen, C. Wang and J. G. Zhang, Functioning Mechanism of  $\text{AlF}_3$  Coating on the Li- and Mn-rich Cathode Materials, *Chem. Mater.*, 2014, **26**, 6320–6327.

307 C. T. Chu, A. Mondal, N. V. Kosova and J. Y. Lin, Improved High-Temperature Cyclability of  $\text{AlF}_3$  Modified Spinel  $\text{LiNi}_{0.5}\text{Mn}_{1.5}\text{O}_4$  Cathode for Lithium-Ion Batteries, *Appl. Surf. Sci.*, 2020, **530**, 147169.

308 H. Zhao, W. Li, J. Li, H. Xu, C. Zhang, J. Li, C. Han, Z. Li, M. Chu and X. Qiu, Enhance Performances of Co-free Li-rich cathode by Eutescic Melting Salt Treatment, *Nano Energy*, 2022, **92**, 106760.

309 F. Wang, P. Zuo, Z. Xue, Y. Liu, C. Wang and G. Chen, Fluorination Effect on Lithium- and Manganese-Rich Layered Oxide Cathodes, *ACS Energy Lett.*, 2024, **9**, 1249–1260.

310 Z. A. Qureshi, H. A. Tariq, R. A. Shakoor, R. Kahraman and S. AlQaradawi, Impact of Coatings on the Electrochemical Performance of  $\text{LiNi}_{0.5}\text{Mn}_{1.5}\text{O}_4$  Cathode Materials: A Focused Review, *Ceram. Int.*, 2022, **48**, 7374–7392.

311 X. Zheng, W. Liu, Q. Qu, Q. Shi, H. Zheng and Y. Huang, Effectively Stabilizing 5 V Spinel  $\text{LiNi}_{0.5}\text{Mn}_{1.5}\text{O}_4$  Cathode in Organic Electrolyte by Polyvinylidene Fluoride Coating, *Appl. Surf. Sci.*, 2018, **455**, 349–356.

312 Y. Li, Q. Zhang, T. Xu, D. Wang, D. Pan, H. Zhao and Y. Bai,  $\text{LaF}_3$  Nanolayer Surface Modified Spinel  $\text{LiNi}_{0.5}\text{Mn}_{1.5}\text{O}_4$  Cathode Material for Advanced Lithium-Ion Batteries, *Ceram. Int.*, 2018, **44**, 4058–4066.

313 K. Min, K. Park, S. Y. Park, S. W. Seo, B. Choi and E. Cho, Improved Electrochemical Properties of  $\text{LiNi}_{0.91}\text{Co}_{0.06}\text{Mn}_{0.03}\text{O}_2$  Cathode Material via Li-Reactive Coating with Metal Phosphates, *Sci. Rep.*, 2017, **7**, 1–10.

314 F. Long, Y. Liu, G. Zhu, Y. Wang and H. Zheng, Phosphate and Borate-Based Composite Interface of Single-Crystal  $\text{LiNi}_{0.8}\text{Co}_{0.1}\text{Mn}_{0.1}\text{O}_2$  Enables Excellent Electrochemical Stability at High Operation Voltage, *Materials*, 2023, **16**, 3613.

315 T. Jenkins, J. A. Alarco, B. Cowie and I. D. R. Mackinnon, Regulation of Surface Oxygen Activity in Li-rich layered Cathodes Using Band Alignment of Vanadium Phosphate Surface Coatings, *J. Mater. Chem. A*, 2022, **10**, 24487–24509.

316 S. Deng, B. Xiao, B. Wang, X. Li, K. Kaliyappan, Y. Zhao, A. Lushington, R. Li, T. K. Sham, H. Wang and X. Sun, New Insight into Atomic-Scale Engineering of Electrode Surface for Long-Life and Safe High Voltage Lithium Ion cathodes, *Nano Energy*, 2017, **38**, 19–27.

317 H. Zhao, W. Li, J. Li, H. Xu, C. Zhang, J. Li, C. Han, Z. Li, M. Chu and X. Qiu, Enhance Performances of Co-free Li-rich cathode by Eutescic Melting Salt Treatment, *Nano Energy*, 2022, **92**, 106760.

318 T. F. Yi, Y. M. Li, X. Y. Li, J. J. Pan, Q. Zhang and Y. R. Zhu, Enhanced Electrochemical Property of  $\text{FePO}_4$ -Coated  $\text{LiNi}_{0.5}\text{Mn}_{1.5}\text{O}_4$  as Cathode Materials for Li-Ion Battery, *Sci. Bull.*, 2017, **62**, 1004–1010.

319 Y. Li, H. Shi, J. He, X. Li, Z. Chen, Y. Zhang, L. Deng, P. Dong, D. Wang, Y. Zhang and J. Duan, Enhanced Cyclability and Reversibility of Nickel-Rich Cathode for Lithium-Ion Batteries via  $\text{LiH}_2\text{PO}_4$  Assisted Saturated  $\text{Li}_2\text{CO}_3$  Washing, *Appl. Surf. Sci.*, 2022, **593**, 153409.

320 J. Liu, Y. Zhang, J. Liu, J. Li, X. Qiu and F. Cheng, In-Situ  $\text{Li}_3\text{PO}_4$  Coating of Li-Rich Mn-Based Cathode Materials for Lithium-ion Batteries, *Acta Chim. Sin.*, 2009, **78**, 1426–1433.

321 S. You, H. T. Tan, L. Wei, W. Tan and C. Chao Li, Design Strategies of Si/C Composite Anode for Lithium-Ion Batteries, *Chem. – Eur. J.*, 2021, **27**, 12237–12256.

322 L. Yang, S. Li, Y. Zhang, H. Feng, J. Li, X. Zhang, H. Guan, L. Kong and Z. Chen, Multi-Scale Design of Silicon/Carbon Composite Anode Materials for Lithium-Ion Batteries: A Review, *J. Energy Chem.*, 2024, **97**, 30–45.

323 J. Liu, Q. Zhang, Z. Y. Wu, J. T. Li, L. Huang and S. G. Sun, Nano-/Microstructured Si/C Composite with High Tap Density as an Anode Material for Lithium-Ion Batteries, *ChemElectroChem*, 2015, **2**, 611–616.



324 M. Abdollahifar, A. Vinograd, C. Y. Lu, S. J. Chang, J. Müller, L. Frankenstein, T. Placke, A. Kwade, M. Winter, C. Y. Chao and N. L. Wu, Enabling Long-Cycling Life of Silicon-Graphite Composite Anodes via Fabrication of a Multi-functional Polymeric Artificial Solid-Electrolyte Interphase Protective Layer, *ACS Appl. Mater. Interfaces*, 2022, **14**, 38824–38834.

325 H. Zhu, M. H. A. Shiraz, L. Liu, Y. Hu and J. Liu, A Facile and Low-Cost  $\text{Al}_2\text{O}_3$  Coating as an Artificial Solid Electrolyte Interphase Layer on Graphite/Silicon Composites for Lithium-Ion Batteries, *Nanotechnology*, 2021, **32**, 144001.

326 H. Zhang, Y. Yang, D. Ren, L. Wang and X. He, Graphite as Anode Materials: Fundamental Mechanism, Recent Progress and Advances, *Energy Storage Mater.*, 2021, **36**, 147–170.

327 H. Zhao, H. Zuo, J. Wang and S. Jiao, Practical Application of Graphite in Lithium-Ion Batteries: Modification, Composite, and Sustainable Recycling, *J. Energy Storage*, 2024, **98**, 113125.

328 Y. Lu, L. Yu and X. W. (David), Lou, Nanostructured Conversion-type Anode Materials for Advanced Lithium-Ion Batteries, *Chem*, 2018, **4**, 972–996.

329 S. Fang, D. Bresser, S. Passerini, S. Fang, D. Bresser and S. Passerini, Transition Metal Oxide Anodes for Electrochemical Energy Storage in Lithium- and Sodium-Ion Batteries, *Adv. Energy Mater.*, 2020, **10**, 1902485.

330 M. H. Hossain, M. A. Chowdhury, N. Hossain, M. A. Islam and M. H. Mobarak, Advances of Lithium-Ion Batteries Anode Materials—A Review, *Chem. Eng. J. Adv.*, 2023, **16**, 100569.

331 G. G. Amatucci and N. Pereira, Fluoride Based Electrode Materials for Advanced Energy Storage Devices, *J. Fluorine Chem.*, 2007, **128**, 243–262.

332 Y. M. Lin, P. R. Abel, A. Heller and C. B. Mullins,  $\alpha\text{-Fe}_2\text{O}_3$  Nanorods as Anode Material for Lithium Ion Batteries, *J. Phys. Chem. Lett.*, 2011, **2**, 2885–2891.

333 J. A. Weeks, H. H. Sun, H. S. Srinivasan, J. N. Burrow, J. V. Guerrera, M. L. Meyerson, A. Dolocan, A. Heller and C. B. Mullins, Facile Synthesis of a Tin Oxide-Carbon Composite Lithium-Ion Battery Anode with High Capacity Retention, *ACS Appl. Energy Mater.*, 2019, **2**, 7244–7255.

334 J. Hou, Y. Yao, Y. Wang, W. Yang, F. Wang, P. Dong, X. Wang, Y. Zhang, X. Li and Y. Zhang, Application of Two-Dimensional Lamellar Lithium Titanate in Lithium-Ion Anode Batteries, *Electrochem. Commun.*, 2023, **156**, 107588.

335 J. Liu, K. Song, P. A. Van Aken, J. Maier and Y. Yu, Self-Supported  $\text{Li}_4\text{Ti}_5\text{O}_{12}\text{-C}$  Nanotube Arrays as High-rate and Long-Life Anode Materials for Flexible Li-Ion Batteries, *Nano Lett.*, 2014, **14**, 2597–2603.

336 X. Chen, X. Zhu, G. Cao, S. Zhang, Y. Mu, H. Ming and J. Qiu,  $\text{Fe}_3\text{O}_4$ -Based Anodes with High Conductivity and Fast Ion Diffusivity Designed for High-Energy Lithium-Ion Batteries, *Energy Fuels*, 2021, **35**, 1810–1819.

337 Y. K. Liu, C. Z. Zhao, J. Du, X. Q. Zhang, A. B. Chen and Q. Zhang, Research Progresses of Liquid Electrolytes in Lithium-Ion Batteries, *Small*, 2023, **19**, 2205315.

338 K. Schroder, J. Alvarado, T. A. Yersak, J. Li, N. Dudney, L. J. Webb, Y. S. Meng and K. J. Stevenson, The Effect of Fluoroethylene Carbonate as an Additive on the Solid Electrolyte Interphase on Silicon Lithium-Ion Electrodes, *Chem. Mater.*, 2015, **27**, 5531–5542.

339 H. Dai, L. Gomes, D. Maxwell, S. Zamani, K. Yang, D. Atienza, N. Dale and S. Mukerjee, Exploring the Role of an Electrolyte Additive in Suppressing Surface Reconstruction of a Ni-Rich NMC Cathode at Ultrahigh Voltage via Enhanced In Situ and Operando Characterization Methods, *ACS Appl. Mater. Interfaces*, 2024, **16**, 8639–8654.

340 Y. Zou, Z. Ma, G. Liu, Q. Li, D. Yin, X. Shi, Z. Cao, Z. Tian, H. Kim, Y. Guo, C. Sun, L. Cavallo, L. Wang, H. N. Alshareef, Y. K. Sun and J. Ming, Non-Flammable Electrolyte Enables High-Voltage and Wide-Temperature Lithium-Ion Batteries with Fast Charging, *Angew. Chem., Int. Ed.*, 2023, **62**, 2201207.

341 J. Y. Hwang, S. J. Park, C. S. Yoon and Y. K. Sun, Customizing a Li-Metal Battery that Survives Practical Operating Conditions for Electric Vehicle Applications, *Energy Environ. Sci.*, 2019, **12**, 2174–2184.

342 Y. Z. Quan, Q. S. Liu, M. C. Liu, G. R. Zhu, G. Wu, X. L. Wang and Y. Z. Wang, Flame-Retardant Oligomeric Electrolyte Additive for Self-Extinguishing and Highly-Stable Lithium-Ion Batteries: Beyond Small Molecules, *J. Energy Chem.*, 2023, **84**, 374–384.

343 R. Mishra, M. Anne, S. Das, T. Chavva, M. V. Shelke and V. G. Pol, Glory of Fire Retardants in Li-Ion Batteries: Could They Be Intrinsically Safer?, *Adv. Sustainable Syst.*, 2024, **8**, 2400273.

344 Y. Dong, N. Zhang, C. Li, Y. Zhang, M. Jia, Y. Wang, Y. Zhao, L. Jiao, F. Cheng and J. Xu, Fire-Retardant Phosphate-Based Electrolytes for High-Performance Lithium Metal Batteries, *ACS Appl. Energy Mater.*, 2019, **2**, 2708–2716.

345 Y. Liu, J. Lu, X. Gong, J. Liu, B. Chen, C. Wu and Z. Fang, Formulating Compatible Non-Flammable Electrolyte for Lithium-Ion Batteries with Ethoxy (Pentafluoro) Cyclotriphosphazene, *RSC Adv.*, 2024, **14**, 11533–11540.

346 J. Long, J. Huang, Y. Miao, H. Huang, X. Chen, J. Wu, X. Li and Y. Chen, A Multi-Functional Electrolyte Additive for Fast-Charging and Flame-Retardant Lithium-Ion Batteries, *J. Mater. Chem. A*, 2024, **12**, 17306–17314.

347 S. M. Seraji, H. Gan, S. R. Swan and R. J. Varley, Phosphazene as an Effective Flame Retardant for Rapid Curing Epoxy Resins, *React. Funct. Polym.*, 2021, **164**, 104910.

348 K. Daems, P. Yadav, K. B. Dermenci, J. Van Mierlo and M. Berecibar, Advances in Inorganic, Polymer and Composite Electrolytes: Mechanisms of Lithium-Ion Transport and Pathways to Enhanced Performance, *Renewable Sustainable Energy Rev.*, 2024, **191**, 114136.

349 C. Li, Z. Y. Wang, Z. J. He, Y. J. Li, J. Mao, K. H. Dai, C. Yan and J. C. Zheng, An Advance Review of Solid-State Battery: Challenges, Progress and Prospects, *Sustainable Mater. Technol.*, 2021, **29**, e00297.



350 X. Fu, D. Yu, J. Zhou, S. Li, X. Gao, Y. Han, P. Qi, X. Feng and B. Wang, Inorganic and Organic Hybrid Solid Electrolytes for Lithium-Ion Batteries, *CrysEngComm*, 2016, **18**, 4236–4258.

351 S. J. Tan, W. P. Wang, Y. F. Tian, S. Xin and Y. G. Guo, Advanced Electrolytes Enabling Safe and Stable Rechargeable Li-Metal Batteries: Progress and Prospects, *Adv. Funct. Mater.*, 2021, **31**, 2105253.

352 H. Liang, L. Wang, A. Wang, Y. Song, Y. Wu, Y. Yang and X. He, Tailoring Practically Accessible Polymer/Inorganic Composite Electrolytes for All-Solid-State Lithium Metal Batteries: A Review, *Nano-Micro Lett.*, 2023, **15**, 42.

353 Y. Wei, Z. Li, Z. Chen, P. Gao, M. Gao, C. Yan, Z. Wu, Q. Ma, Y. Jiang, X. Yu, X. Zhang, Y. Liu, Y. Yang, M. Gao, W. Sun, Z. Qu, J. Chen and H. Pan, A Wide Temperature 10 V Solid-State Electrolyte with a Critical Current Density of over 20 mA cm<sup>-2</sup>, *Energy Environ. Sci.*, 2023, **16**, 4679–4692.

354 J. Sastre, M. H. Futscher, L. Pompizi, A. Aribia, A. Priebe, J. Overbeck, M. Stiefel, A. N. Tiwari and Y. E. Romanyuk, Blocking Lithium Dendrite Growth in Solid-State Batteries with an Ultrathin Amorphous Li-La-Zr-O Solid Electrolyte, *Commun. Mater.*, 2021, **2**, 76.

355 W. Li, J. R. Dahn and D. S. Wainwright, Rechargeable Lithium Batteries with Aqueous Electrolytes, *Science*, 1994, **264**, 1115–1118.

356 H. Zhang, X. Liu, H. Li, I. Hasa and S. Passerini, Challenges and Strategies for High-Energy Aqueous Electrolyte Rechargeable Batteries, *Angew. Chem., Int. Ed.*, 2021, **60**, 598–616.

357 L. Suo, O. Borodin, T. Gao, M. Olgui, J. Ho, X. Fan, C. Luo, C. Wang and K. Xu, ‘Water-in-salt’ Electrolyte enables High-Voltage Aqueous Lithium-Ion Chemistries, *Science*, 2015, **350**, 938–943.

358 L. Suo, O. Borodin, W. Sun, X. Fan, C. Yang, F. Wang, T. Gao, Z. Ma, M. Schroeder, A. von Cresce, S. M. Russell, M. Armand, A. Angell, K. Xu and C. Wang, Advanced High-Voltage Aqueous Lithium-Ion Battery Enabled by ‘Water-in-Bisalt’ Electrolyte, *Angew. Chem., Int. Ed.*, 2016, **128**, 7252–7257.

359 L. Droguet, A. Grimaud, O. Fontaine and J. M. Tarascon, Water-in-Salt Electrolyte (WiSE) for Aqueous Batteries: A Long Way to Practicality, *Adv. Energy Mater.*, 2020, **10**, 2002440.

360 L. Kong, Y. Li and W. Feng, Strategies to Solve Lithium Battery Thermal Runaway: From Mechanism to Modification, *Electrochem. Energy Rev.*, 2021, **4**, 633–679.

361 X. Lai, Z. Meng, F. Zhang, Y. Peng, W. Zhang, L. Sun, L. Wang, F. Gao, J. Sheng, S. Su, Y. Zheng and X. Feng, Mitigating Thermal Runaway Hazard of High-Energy Lithium-Ion Batteries by Poison Agent, *J. Energy Chem.*, 2023, **83**, 3–15.

362 A. Friesen, S. Hildebrand, F. Horsthemke, M. Börner, R. Klöpsch, P. Niehoff, F. M. Schappacher and M. Winter, Al<sub>2</sub>O<sub>3</sub> Coating on Anode Surface in Lithium Ion Batteries: Impact on Low Temperature Cycling and Safety Behavior, *J. Power Sources*, 2017, **363**, 70–77.

363 M. Naguib, S. Allu, S. Simunovic, J. Li, H. Wang and N. J. Dudney, Limiting Internal Short-Circuit Damage by Electrode Partition for Impact-Tolerant Li-Ion Batteries, *Joule*, 2018, **2**, 155–167.

364 W. Ji, B. Jiang, F. Ai, H. Yang and X. Ai, Temperature-Responsive Microspheres-Coated Separator for Thermal Shutdown Protection of Lithium Ion Batteries, *RSC Adv.*, 2015, **5**, 172–176.

365 Y. Shi, D. J. Noelle, M. Wang, A. V. Le, H. Yoon, M. Zhang, Y. S. Meng, J. Fan, D. Wu and Y. Qiao, Mitigating Thermal Runaway of Lithium-Ion Battery through Electrolyte Displacement, *Appl. Phys. Lett.*, 2017, **110**, 063902.

366 J. Weng, D. Ouyang, Y. Liu, M. Chen, Y. Li, X. Huang and J. Wang, Alleviation on Battery Thermal Runaway Propagation: Effects of Oxygen Level and Dilution Gas, *J. Power Sources*, 2021, **509**, 230340.

367 H. Niu, C. Chen, Y. Liu, L. Li, Z. Li, D. Ji and X. Huang, Mitigating Thermal Runaway Propagation of NCM 811 Prismatic Batteries via Hollow Glass Microspheres Plates, *Process Saf. Environ. Prot.*, 2022, **162**, 672–683.

368 J. Xu, C. Lan, Y. Qiao and Y. Ma, Prevent Thermal Runaway of Lithium-Ion Batteries with Minichannel Cooling, *Appl. Therm. Eng.*, 2017, **110**, 883–890.

369 X. Hu, F. Gao, Y. Xiao, D. Wang, Z. Gao, Z. Huang, S. Ren, N. Jiang and S. Wu, Advancements in the Safety of Lithium-Ion Battery: The Trigger, Consequence and Mitigation Method of Thermal Runaway, *Chem. Eng. J.*, 2024, **481**, 148450.

370 J. Xu, P. Guo, Q. Duan, X. Yu, L. Zhang, Y. Liu and Q. Wang, Experimental Study of the Effectiveness of Three Kinds of Extinguishing Agents on Suppressing Lithium-Ion Battery Fires, *Appl. Therm. Eng.*, 2020, **171**, 115076.

371 W. Zhang, N. Ouyang, X. Yin, X. Li, W. Wu and L. Huang, Data-driven Early Warning Strategy for Thermal Runaway Propagation in Lithium-Ion Battery Modules with Variable State of Charge, *Appl. Energy*, 2022, **323**, 119614.

372 J. Jaguemont, L. Boulon and Y. Dubé, A Comprehensive Review of Lithium-Ion Batteries used in Hybrid and Electric Vehicles at Cold Temperatures, *Appl. Energy*, 2016, **164**, 99–114.

373 Y. Feng, L. Zhou, H. Ma, Z. Wu, Q. Zhao, H. Li, K. Zhang and J. Chen, Challenges and Advances in Wide-Temperature Rechargeable Lithium Batteries, *Energy Environ. Sci.*, 2022, **5**, 1711–1759.

374 J. Hou, M. Yang, D. Wang and J. Zhang, Fundamentals and Challenges of Lithium Ion Batteries at Temperatures between –40 and 60 °C, *Adv. Energy Mater.*, 2020, **10**, 1904152.

375 A. Hu, F. Li, W. Chen, T. Lei, Y. Li, Y. Fan, M. He, F. Wang, M. Zhou, Y. Hu, Y. Yan, B. Chen, J. Zhu, J. Long, X. Wang and J. Xiong, Ion Transport Kinetics in Low-Temperature Lithium Metal Batteries, *Adv. Energy Mater.*, 2022, **12**, 2202432.

376 D. Hubble, D. E. Brown, Y. Zhao, C. Fang, J. Lau, B. D. McCloskey and G. Liu, Liquid Electrolyte Development for Low-Temperature Lithium-Ion Batteries, *Energy Environ. Sci.*, 2022, **15**, 550–578.



377 A. Hu, F. Li, W. Chen, T. Lei, Y. Li, Y. Fan, M. He, F. Wang, M. Zhou, Y. Hu, Y. Yan, B. Chen, J. Zhu, J. Long, X. Wang and J. Xiong, Ion Transport Kinetics in Low-Temperature Lithium Metal Batteries, *Adv. Energy Mater.*, 2022, **12**, 2202432.

378 N. Piao, X. Gao, H. Yang, Z. Guo, G. Hu, H. M. Cheng and F. Li, Challenges and Development of Lithium-Ion Batteries for Low Temperature Environments, *eTransportation*, 2022, **11**, 100145.

379 J. Hou, M. Yang, D. Wang and J. Zhang, Fundamentals and Challenges of Lithium Ion Batteries at Temperatures between  $-40$  and  $60$   $^{\circ}\text{C}$ , *Adv. Energy Mater.*, 2020, **10**, 1904152.

380 D. Yaakov, Y. Gofer, D. Aurbach and I. C. Halalay, On the Study of Electrolyte Solutions for Li-Ion Batteries that can work over a Wide Temperature Range, *J. Electrochem. Soc.*, 2010, **157**, A1383.

381 M. C. Smart, B. V. Ratnakuma and S. Surampudi, Electrolytes for Low-Temperature Lithium Batteries Based on Ternary Mixtures of Aliphatic Carbonates, *J. Electrochem. Soc.*, 1999, **146**, 486.

382 M. C. Smart, B. V. Ratnakumar, S. Surampudi, Y. Wang, X. Zhang, S. G. Greenbaum, A. Hightower, C. C. Ahn and B. Fultz, Irreversible Capacities of Graphite in Low-Temperature Electrolytes for Lithium-Ion Batteries, *J. Electrochem. Soc.*, 1991, **146**, 3963.

383 M. C. Smart, B. V. Ratnakumar and S. Surampudi, Use of Organic Esters as Cosolvents in Electrolytes for Lithium-Ion Batteries with Improved Low Temperature Performance, *J. Electrochem. Soc.*, 2002, **149**, A361.

384 S. V. Sazhin, M. Y. Khimchenko, Y. N. Tritenichenko and H. S. Lim, Performance of Li-Ion Cells with New Electrolytes Conceived for Low-Temperature Applications, *J. Power Sources*, 2000, **87**, 112–117.

385 E. J. Plichta, M. Hendrickson, R. Thompson, G. Au, W. K. Behl, M. C. Smart, B. V. Ratnakumar and S. Surampudi, Development of Low Temperature Li-Ion Electrolytes for NASA and DoD Applications, *J. Power Sources*, 2001, **94**, 160–162.

386 D. R. Wright, N. Garcia-Araez and J. R. Owen, Review on High Temperature Secondary Li-Ion Batteries, *Energy Proc.*, 2018, **151**, 174–181.

387 M.-T. F. Rodrigues, G. Babu, H. Gullapalli, K. Kalaga, F. N. Sayed, K. Kato, J. Joyner and P. M. Ajayan, A Materials Perspective on Li-Ion Batteries at Extreme Temperatures, *Nat. Energy*, 2017, **2**, 17108.

388 S. Hess, M. Wohlfahrt-Mehrens and M. Wachtler, Flammability of Li-Ion Battery Electrolytes: Flash Point and Self-Extinguishing Time Measurements, *J. Electrochem. Soc.*, 2015, **162**, A3084.

389 K. Xu, S. Zhang, T. R. Jow, W. Xu and C. A. Angell, LiBOB as Salt for Lithium-Ion Batteries: A Possible Solution for High Temperature Operation, *Electrochem. Solid-State Lett.*, 2002, **5**, A26.

390 A. Du Pasquier, F. Disma, T. Bowmer, A. S. Gozdz, G. Amatucci and J.-M. Tarascon, Differential Scanning Calorimetry Study of the Reactivity of Carbon Anodes in Plastic Li-Ion Batteries, *J. Electrochem. Soc.*, 1998, **145**, 472–477.

391 Z. Zhang, D. Fouchard and J. R. Rea, Differential Scanning Calorimetry Material Studies: Implications for the Safety of Lithium-Ion Cells, *J. Power Sources*, 1998, **70**, 16–20.

392 H. Maleki, G. Deng, A. Anani and J. Howard, Thermal Stability Studies of Li-Ion Cells and Components, *J. Electrochem. Soc.*, 1999, **146**, 3224.

393 B. Sims and S. Crase, Review of Battery Technologies for Military Land Vehicles, 2017, <https://apps.dtic.mil/sti/tr/pdf/AD1027339.pdf>, (accessed April 2025).

394 J. M. Hooper and J. Marco, Characterising the In-Vehicle Vibration Inputs to the High Voltage Battery of an Electric Vehicle, *J. Power Sources*, 2014, **245**, 510–519.

395 L. Shui, F. Chen, A. Garg, X. Peng, N. Bao and J. Zhang, Design Optimization of Battery Pack Enclosure for Electric Vehicle, *Struct. Multidisciplinary Optimization*, 2018, **58**, 331–347.

396 J. M. Hooper, J. Marco, G. H. Chouchelamane and C. Lyness, Vibration Durability Testing of Nickel Manganese Cobalt Oxide (NMC) Lithium-Ion 18 650 Battery Cells, *Energies*, 2016, **9**, 52.

397 J. M. Hooper, J. Marco, G. H. Chouchelamane, J. S. Chevalier and D. Williams, Multi-axis Vibration Durability Testing of Lithium Ion 18 650 NCA Cylindrical Cells, *J. Energy Storage*, 2018, **15**, 103–123.

398 L. Somerville, J. M. Hooper, J. Marco, A. McGordon, C. Lyness, M. Walker and P. Jennings, Impact of Vibration on the Surface Film of Lithium-Ion Cells, *Energies*, 2017, **10**, 741.

399 S. Mutagekar and A. Jhunjhunwala, Designing Small Batteries and Adaptive Charging Strategies for Operation on Rough Terrain, *J. Energy Storage*, 2024, **84**, 111003.

400 S. Chavan, B. Venkateswarlu, R. Prabakaran, M. Salman, S. W. Joo, G. S. Choi and S. C. Kim, Thermal Runaway and Mitigation Strategies for Electric Vehicle Lithium-Ion Batteries using Battery Cooling Approach: A Review of the Current Status and Challenges, *J. Energy Storage*, 2023, **72**, 108569.

401 A. Rabbitt, I. Horsfall and D. J. Carr, Effect of Ballistic Impacts on Batteries and the potential for injury, *BMJ Mil. Health*, 2020, **166**, 330–335.

402 Y. Yang, R. Wang, Z. Shen, Q. Yu, R. Xiong and W. Shen, Towards a Safer Lithium-Ion Batteries: A Critical Review on Cause, Characteristics, Warning and Disposal Strategy for Thermal Runaway, *Adv. Appl. Energy*, 2023, **11**, 100146.

403 U.S. Department of Homeland Security, System Assessment and Validation for Emergency Responders (SAVER), <https://www.dhs.gov/science-and-technology/saver>, (accessed April 2025).

404 U.S. Department of Homeland Security, Batteries for Firefighting Equipment, <https://www.dhs.gov/group/13025/saver/batteries-firefighting-equipment>, (accessed April 2025).

405 U.S. Department of Homeland Security, Self-Contained Breathing Apparatuses (SCBA) Lessons Learned Report,

[https://www.dhs.gov/sites/default/files/2024-05/24\\_0517\\_st\\_nustl\\_scba\\_lessons\\_learned\\_report.pdf](https://www.dhs.gov/sites/default/files/2024-05/24_0517_st_nustl_scba_lessons_learned_report.pdf), (accessed April 2025).

406 X. Feng, M. Ouyang, X. Liu, L. Lu, Y. Xia and X. He, Thermal Runaway Mechanism of Lithium Ion Battery for Electric Vehicles: A Review, *Energy Storage Mater.*, 2018, **10**, 246–267.

407 C. Xiao, B. Wang, D. Zhao and C. Wang, Comprehensive Investigation on Lithium Batteries for Electric and Hybrid-electric Unmanned Aerial Vehicle Applications, *Therm. Sci. Eng. Prog.*, 2023, **38**, 101677.

408 R. Wang, X. Zhou, Y. Wang, Y. Xiao, Z. Shi, Y. Liu and T. Zhang, Degradation Analysis of Lithium-Ion Batteries under Ultrahigh-Rate Discharge Profile, *Appl. Energy*, 2024, **376**, 124241.

409 X. Long, J. Lu, Y. Wu, J. Wei and R. Zhou, High Rate Pulse Discharge of Lithium Battery in Electromagnetic Launch System, *Int. J. Emerg. Electr. Power Syst.*, 2018, **19**, 20170172.

410 H. Oman, Aerospace & Military Battery Applications, *IEEE Aerosp. Electron. Syst. Maga.*, 2002, **17**, 29–35.

411 E. Catenaro, D. M. Rizzo and S. Onori, Framework for Energy Storage Selection to Design the Next Generation of Electrified Military Vehicles, *Energy*, 2021, **231**, 120695.

412 J. A. Jeevarajan and C. S. Winchester, Battery Safety Qualifications for Human Ratings, *Electrochem. Soc. Interface*, 2012, **21**, 51–55.

413 Naval Sea Systems Command, SG270-BV-SAF-010 High-Energy Storage System Safety Manual, 2011, [https://every spec.com/USN/NAVSEA/SG270-BV-SAF-010\\_27APR2011\\_50446](https://every spec.com/USN/NAVSEA/SG270-BV-SAF-010_27APR2011_50446), (accessed April 2025).

414 Naval Sea Systems Command, S9310-AQ-SAF-010 Navy Lithium Battery Safety Program Responsibilities and Procedures Revision 3, 2020, [https://navysbir.com/n21\\_1/Topic-N211-033-Reference\\_Document\\_S9310-AQ-SAF-010-Rev3.pdf](https://navysbir.com/n21_1/Topic-N211-033-Reference_Document_S9310-AQ-SAF-010-Rev3.pdf), (accessed April 2025).

415 A. Nedjalkov, J. Meyer, M. Köhring, A. Doering, M. Angelmahr, S. Dahle, A. Sander, A. Fischer and W. Schade, Toxic Gas Emissions from Damaged Lithium Ion Batteries—Analysis and Safety Enhancement Solution, *Batteries*, 2016, **2**, 5.

